ISBN 978-82-326-2368-6 (printed ver.)
ISBN 978-82-326-2369-3 (electronic ver.)
ISSN 1503-8181

Astrid Røkke
Doctoral thesis

Doctoral theses at NTNU, 2017:148

Astrid Røkke

PERMANENT MAGNET GENERATORS FOR MARINE CURRENT TIDAL TURBINES

Analysis and optimisation of low- to medium- speed machines featuring various winding layouts

NTNU
Norwegian University of Science and Technology

NTNU
Norwegian University of Science and Technology

Thesis for the Degree of Philosophiae Doctor
Faculty of Information Technology and Electrical Engineering
Department of Electric Power Engineering

Doctoral theses at NTNU, 2017:148
NTNU

Astrid Røkke

PERMANENT MAGNET GENERATORS FOR MARINE CURRENT TIDAL TURBINES

Analysis and optimisation of low- to medium-speed machines featuring various winding layouts

Thesis for the Degree of Philosophiae Doctor

Trondheim, May 2017

Norwegian University of Science and Technology
Faculty of Information Technology and Electrical Engineering
Department of Electric Power Engineering

NTNU
Norwegian University of
Science and Technology

NTNU
Norwegian University of Science and Technology

Thesis for the Degree of Philosophiae Doctor

Faculty of Information Technology and Electrical Engineering
Department of Electric Power Engineering

ISBN 978-82-326-2368-6 (printed ver.)
ISBN 978-82-326-2369-3 (electronic ver.)
ISSN 1503-8181

Doctoral theses at NTNU, 2017:148

Printed by NTNU Grafisk senter

Acknowledgements

This dissertation is a summary of the work that I have performed during four years as a PhD student at the Norwegian University of Science and Technology in the department of Electric Power Engineering. I am grateful to SmartMotor AS, now a part of Rolls-Royce Marine AS, for financing my study program and PhD project. They have also helped to shape my PhD study and provided valuable input to my analysis.

I would like to thank my supervisor, Professor Robert Nilssen, for being frank and for challenging my opinions. I appreciate the fact that we are both unafraid to speak our own minds and that we on some points think alike and on some points can agree to disagree.
Thank you to my co-supervisor Arne Nysveen for helping me to be more organised. Thomas Nordaunet and Erlend L. Engevik did a lot of good work on optimisation in their master theses, which was also very helpful to me.

I also want to thank my many colleagues in the department, for keeping my days interesting and for providing a social life in addition to my academic life. I am especially grateful to Nathalie, Mostafa, Erlend, and Eric for interesting discussions on PM machines and other relevant subjects.

Last, I want to thank Sverre, for being there for me all the time, and for the sacrifices you have made. I would not have managed this without you. Thank you to Ane, who has been growing up alongside this thesis, and to Sigrid, who gave me a diversion in the middle of it, for taking my mind off work when I shouldn't work and for constantly reminding me about the important things in life.

Abstract

The focus of this thesis is the design of a permanent magnet generator for a marine current turbine, more specifically a tidal turbine. Tidal turbines can offer a predictable input of energy to the power grid and help to eliminate the dependency on fossil fuels. The marine current energy industry is currently working to reduce the cost of energy. Optimisation can be used both to optimise the power train topology at the system level and to reduce the cost of each individual component. In this thesis, optimisation is used to minimise the cost of the active materials for a generator and the cost of energy lost in the generator over its lifetime.

A review of various tidal turbine concepts was conducted and resulted in a set of specifications for the generator: a 1,5 MW turbine with a nominal speed of 15 rpm and a 3,3 kV voltage rating. The turbine may be geared or directly driven, and the nominal speed of the generator may range from 15 rpm to 1000 rpm.

A radial-flux, inner-rotor, surface-mounted, slotted machine with laminated stator and rotor cores was chosen as the basis for optimisation. A novel feature of the work presented in this thesis is that in the optimisation routine, the numbers of poles and slots can be allowed to freely vary. The optimisation will result in the most optimal winding topology for the given application. The winding topology can be either distributed or concentrated. In the optimisation, constraints are placed on the spatial envelope, the frequency, the power factor, the short-circuit demagnetisation field and machine temperatures.

As part of the optimisation, for each considered machine design, an appropriate winding layout is determined, and a magnetic analysis, an electrical analysis, a loss analysis and a thermal analysis are performed. The outputs of the analysis are the fitness value (cost) and a vector containing the values of all parameters subject to the specified constraints.

This thesis includes a thorough analysis of stator yoke flux patterns in fractional-slot machines. Machine flux densities are often found under the assumption of no

load. However, it is shown in this thesis that the *armature reaction* flux does not have the same amplitude behind all slots. Additionally, the time-varying no-load and armature reaction fluxes are shifted in time, with different phase shifts behind different slots. The *on-load* flux depends on both the amplitudes of the fluxes *and* the phase shift between them, and it varies significantly with the stator position. The amplitude variation depends on the winding configuration and is highest in machines with high subharmonic fields. In one of the investigated machines, the on-load flux behind one slot is 10 times higher than that behind another slot.
The on-load flux can be significantly higher than the no-load flux in the yoke.
The study of the stator yoke flux patterns is one of the major contributions of this thesis. Using this knowledge, it is possible to accurately predict the fluxes in machines at all positions at all times without using finite element analysis (FEA). An optimisation routine that constrained only the no-load flux densities and not the on-load flux densities would undoubtedly produce optimal machine designs that would be highly saturated at load. It is also possible to use this knowledge when choosing the position of holes and bolts in the laminations. Flux barriers in the stator have previously been used to reduce the subharmonics in fractional-slot machines. By investigating the positions in which the stator is more saturated, the positions of the flux barriers can be chosen more appropriately.

The analytical estimation of induced eddy-current losses has been identified as the most challenging part of the analysis. Various established methods for the computation of the eddy-current magnet losses were analysed here; however, none of the methods yielded results that matched the FEA results well. In this thesis, it is shown that it is possible to find the area of the magnitude of the eddy-current losses, but when the level of segmentation is either high or low, the analytical results do not match the FEA results very well. Analytical methods for calculating eddy-current losses in magnets should be used with the knowledge that the results are not very reliable. Other methods, which require more computational effort, must be used if a higher degree of confidence is desired.

Two main classes of optimisation methods exist, both with advantages and disadvantages. One gradient-based solver, available through MATLAB, and one direct optimisation method, a genetic algorithm that is also available through MATLAB, were used in this thesis work. The fast gradient-based solver solves a subproblem with a reduced number of possible slot-and-pole combinations. The speed of the solver enables the designer to repeat the optimisation routine with a changing set of requirements. The minimum cost, and the optimal design, can thereby be found as a function of parameters such as the power factor or the energy price. In this thesis, it is shown that in the case of a one-stage gear train, the cost of active materials *decreases* with an increasing number of poles while the cost of energy loss

increases, and an optimal number of poles exists. The optimal generator designs for a direct drive, a one-stage gear train and a two-stage gear train are also shown. It is often claimed that gradient-based solvers are unsuitable for electrical machine design optimisation because such a solver finds only local minima for a nonlinear problem. Here, it is shown that as long as there are no, or very few, integer variables, the tested gradient-based solver is certainly capable of solving the problem when multiple startpoints are used.

The second tested optimisation algorithm, the genetic algorithm, is able to solve the full problem, with freely varying numbers of slots and poles. This capability comes at the cost of additional time spent. Although the genetic algorithm is a global optimisation tool, the genetic algorithm also will find only a local minimum if the number of individuals or generations is too small or if the diversity of the population is either too narrow or too wide.
A hybrid algorithm is ultimately used in this thesis; this algorithm combines the genetic and gradient-based algorithm, such that the genetic algorithm first locates the area of the global minimum and the gradient-based algorithm then locates the exact minimum.
The optimisation reported in this thesis shows that the lowest cost for the turbine generator is achieved using double-layer fractional-slot concentrated winding machines when the speed is less than approximately 1000 rpm. In a generator equipped with a three-stage gear train, either concentrated or distributed windings can be used with a comparable cost.
The optimal generator design has been found for six different generator speeds. The price of the generator decreases with a decreasing gear ratio, as expected. The reduction is most significant for the transition from a direct drive to a one-stage gear train. The curve showing the cost as a function of the generator speed can help guide the system owner in deciding which drive-train topology to choose.

Acronyms, abbreviations and symbols

AC	Alternating current
DC	Direct current
DW	Distributed winding
EMEC	European Marine Energy Centre
FEA	Finite element analysis
FSCW	Fractional-slot concentrated winding
GA	Genetic algorithm
LPM	Lumped parameter model
MMF	Magneto motive force
OTEC	Ocean thermal energy conversion
PM	Permanent magnet
PSO	Particle swarm optimisation
SQP	Sequential Quadratic Programming
THD	Total harmonic distortion
UK	United Kingdom

B_D	T	PM knee flux density value
$B_{m,nl}$	T	No-load flux density in magnets
$B_{m,sc}$	T	Flux density in magnets under short-circuit conditions
B_R	T	Remanent flux density in magnets
$B_{r,ar}$	T	Armature reaction flux density in rotor yoke (max)
$B_{r,nl}$	T	No-load flux density in rotor yoke
$B_{r,sum}$	T	On-load flux density in rotor yoke (max)
$B_{s,ar}$	T	Armature reaction flux density in stator yoke (max)
$B_{s,nl}$	T	No-load flux density in stator yoke
$B_{s,sum}$	T	On-load flux density in stator yoke (max)
$B_{t,ar}$	T	Armature reaction flux density in tooth (max)
$B_{t,nl}$	T	No-load flux density in tooth
$B_{t,sum}$	T	On-load flux density in tooth (max)
C_p		Turbine power coefficient
d_{ins}	m	Slot insulation thickness
$d_{r,yoke}$	m	Rotor yoke thickness
d_{slot}	m	Slot depth
$d_{s,yoke}$	m	Stator yoke thickness
d_{wedge}	m	Slot wedge thickness
$d_{winding}$	m	Winding depth
E	V	No-load phase voltage
f	Hz	Electrical frequency
g	m	Air gap length
I_{ph}	A	Phase current (rms)
$\widehat{I_s}$	A	Slot current (amplitude)
$\widehat{I_{sc}}$	A	Short-circuit current (amplitude)
J	A/mm^2	Current density (rms)
k_C		Carter coefficient
k_d		Winding distribution factor

k_{fill}		Winding fill factor
k_p		Winding pitch factor
k_{slot}		Slot fill factor
k_{sq}		Skewing factor
k_w		Winding factor
k_{wv}		Winding factor of harmonic number v
L	m	Active length
L_{ew}	H	End winding inductance
L_{EW}	m	Average end winding length
l_m	m	Magnet length
L_m	H	Magnetising inductance
L_{mph}	H	Magnetising inductance of a single-phase winding
L_s	H	Synchronous inductance
L_{slot}	H	Slot leakage inductance
L_{sq}	H	Skew leakage inductance
L_{tt}	H	Tooth tip leakage inductance
$l_{winding}$	m	Phase winding length
L_δ	H	Air gap leakage inductance
L_σ	H	Stator leakage inductance
n	rpm	Rotational speed
n'		Winding denominator
n_{pb}		Number of parallel branches
N_c		Number of coils
n_{cs}		Number of coils in series
N_{lam}		Number of magnet laminations per pole
N_{layer}		Number of layers in slot
N_{ph}		Number of phases
n_t		Number of turns per coil
Nu		Nusselt number

p		Number of pole pairs
P	W	Generator active power
$p*$		Number of pole pairs in a base winding
P_{cu}	W	Copper loss (total)
P_e	W	Eddy current loss
p_h	W	Hysteresis loss
P_{pm}	W	Magnet loss (total)
$P_{pm,ar}$	W	Magnet loss caused by the armature reaction
$P_{pm,nl}$	W	Magnet loss caused by reluctance variations
P_{iron}	W	Iron loss (total)
q		Number of slots per pole and phase
Q		Number of slots
$Q*$		Number of slots in a base winding
Q_p		Number of slots per phase
R	Ohm	Resistance
$R_{ac,dc}$		AC/DC resistance factor
R_g	A/Wb	Air gap reluctance
R_{gap}	A/Wb	Air gap and magnet reluctance combined
R_{inner}	m	Rotor inner radius
R_{ml}	A/Wb	Magnet-to-magnet leakage reluctance
R_{mr}	A/Wb	Magnet-to-rotor-yoke leakage reluctance
R_{pm}	A/Wb	Magnet reluctance
R_r	A/Wb	Rotor yoke reluctance
R_s	A/Wb	Stator yoke reluctance
R_{slot}	A/Wb	Slot leakage reluctance
Re		Reynolds number
t		Periodicity of winding
T	Nm	Machine torque
$t*$		Periodicity of winding in a base winding

T_{cu}	°C	Average copper temperature
Ta		Taylor number
V_{pm}	m^m	Total PM volume
w_{lam}	m	Magnet lamination width
w_m	m	Magnet width
w_{slot}	m	Slot width
w_{tooth}	m	Tooth width
$w_{winding}$	m	Winding width
X	Ohm	Phase reactance
y	slot pitches	Coil span
$\overline{y}$	slot pitches	Average coil span
y_Q	slot pitches	Coil span of full pitch winding
y_{sp}	slot pitches	Short pitch factor
z'		Winding numerator
α_m		Magnet width/pole pitch
α_s	deg	Electrical slot angle
$\phi_{g,nl}$	Wb/m	No-load air gap flux (per meter)
ϕ_{pm}	Wb/m	PM remanent flux (per meter)
$\phi_{r,nl}$	Wb/m	No-load rotor yoke flux (per meter)
$\phi_{s,nl}$	Wb/m	No-load stator yoke flux (per meter)
μ_0	H/m	Permeability of vacuum
μ_{pm}		Relative permeability of magnet material
ρ	kg/m^3	Mass density
σ	rad	Phase spread
σ_{cu}	S/m	Electrical conductivity of copper
σ_{pm}	S/m	Electrical conductivity of magnet material
σ_δ		Air gap harmonic leakage factor
τ_p	m	Pole pitch
τ_s	m	Slot pitch

ω	rad/s	Electrical frequency

Contents

Acknowledgements **iii**

Abstract **v**

Acronyms, abbreviations and symbols **ix**

1 Introduction **1**

1.1 Motivation 1

1.2 Approach 2

1.3 Structure of the thesis 3

1.4 List of publications 3

2 Marine current turbines **5**

2.1 Introduction 5

2.2 Marine currents 6

2.3 Power train options 7

2.4 Literature 8

2.5 State of the art 8

2.5.1 Cross-axis turbines 9

2.5.2 Oscillating hydrofoils 10
2.5.3 Enclosed tips (ducted) 11
2.5.4 Horizontal-axis turbines 11
2.5.5 Tidal kites 17
2.5.6 Archimedes screws 17
2.6 Conclusion 17
2.7 Case Study 19

3 Permanent magnet generators **21**
3.1 Introduction 22
3.2 Main categories of PM generators 22
3.3 Main design elements 24
3.3.1 Rotor design 24
3.3.2 Stator design 24
3.3.3 Literature: comparing winding types 26
3.4 Cooling 29
3.5 Main constraints and specifications 29

4 Analysis **33**
4.1 Introduction 33
4.2 Variable selection 33
4.3 Design layout 37
4.3.1 Defining winding types and base windings 37
4.3.2 Winding layout 39
4.3.3 Winding factor 39
4.3.4 End windings 42
4.4 Magnetic analysis 43

4.4.1 Introduction 43
4.4.2 No-load magnetic fields 45
4.4.3 Armature reaction fields 47
4.4.4 Magnetic fields under load: combining the no-load and armature reaction fields 54
4.4.5 Conclusion of Chapter 4.4 62
4.5 Electrical circuit 63
4.5.1 Slot current 63
4.5.2 Inductances 64
4.5.3 Power factor 67
4.6 Torque 68
4.7 Loss analysis 69
4.7.1 Copper and iron losses 69
4.7.2 Permanent magnet losses 70
4.7.3 Lifetime energy loss 87
4.8 Thermal analysis 90
4.8.1 Lumped parameter thermal model 90
4.8.2 Machine temperatures 93
4.9 Demagnetisation 94
4.10 Objective value - cost evaluation 95
4.11 Model verification with FEA 98

5 Optimisation **101**
5.1 Introduction 101
5.2 Nonlinear optimisation 102
5.3 Gradient-based optimisation 104
5.3.1 Introduction 104

5.3.2 MATLAB gradient-based optimisation method, *fmincon* . 104
5.3.3 Implementation of a gradient-based method (*fmincon*) . . 106
5.4 Direct optimisation 109
5.4.1 Introduction 109
5.4.2 Genetic algorithm 110
5.4.3 Implementation of the genetic algorithm 112
5.5 Hybrid algorithm 115
5.5.1 Introduction 115
5.5.2 Implementation of the hybrid algorithm 116
5.5.3 Investigations 116

6 Results **119**
6.1 Introduction 119
6.2 Gradient-based method 120
6.2.1 Generator designs for a one-stage gear train 120
6.2.2 Direct-drive generator designs 125
6.2.3 Generator designs for a two-stage gear train 128
6.2.4 Conclusions from the gradient-based optimisation 129
6.3 Hybrid method 130
6.3.1 Generator designs for a one-stage gear train 131
6.3.2 Various gear ratios 138
6.3.3 Conclusions from the hybrid optimisation 142

7 Conclusions **143**
7.1 Challenges and future work 147

APPENDICES **148**

A Armature-induced eddy-current loss in magnets: Method 4 149

Chapter 1

Introduction

1.1 Motivation

Climate change may be the greatest challenge that humans have faced in modern times. There is an urgent need to replace carbon-based energy sources with renewable energy sources, and it will most likely be necessary to use many of them to satisfy future global energy needs. The development of new renewable energy technology has been my main interest ever since I began my university studies, and I am very happy to have had the opportunity to work towards this goal in my PhD thesis research.
Marine currents, particularly tidal currents, are a vast source of energy; however, tidal turbines are still very expensive, and the cost of energy for tidal energy is higher than for most other renewable energy sources. To reduce the cost of energy to the greatest possible extent, the most cost-effective system must be used, and each component should be as cost-effective as possible.

I had been working on designing permanent magnet machines for several years before I ventured into my life as a PhD candidate. I had become quite experienced with single-layer concentrated winding designs, and I was confident that this type of machine design was very competitive for slow-rotating applications. However, for higher-speed applications, distributed windings seemed more alluring. I wanted to compare the two winding strategies, but simply comparing a distributed winding machine with a concentrated winding machine would not give me the knowledge I needed because either the distributed winding machine or the concentrated winding machine could well be relatively poorly designed, thus resulting in an unfair comparison.

Imagine a simple case in which you have a particular machine design, and you would like to know whether you could improve the design by changing the number of slots. How do you make that change? Do you keep the current loading the same, or the current density? What about the slot depth and the yoke thickness? The changes you make to the machine design will alter the thermal situation of the machine, the inductance, the flux densities, etc. A given design might prove to be lighter but have a lower efficiency; in that case, which do you choose? The only way you can make a fair comparison is to optimise each design for the application of interest, given the same objective and the same constraints. This, then, is the motivation behind the work that serves as the basis for this thesis.

1.2 Approach

Before developing the detailed machine design, I needed to perform a review of various marine current turbines to identify the most typical turbine types, the typical power ratings and speed ranges and the typical gear ratios and types of electrical machines. This review would yield a set of specifications for the tidal turbine for which I would then design the generator.

I also needed to decide on a set of constraints with which the design would need to comply. These constraints would ensure an adequate expected lifetime (temperatures), reasonable converter costs (power factor and frequency), feasible producibility (design envelope and minimum and maximum dimensions of generator parts) and no magnetic saturation or critical demagnetisation.
To quantify the levels of these constrained parameters, it was necessary to perform a thorough analysis of the generator design. This analysis could be conducted using either analytical equations, FEA, or a combination of these. The quality of such a generator analysis is of great importance. Without a reliable analysis, the optimisation results will be of low quality.
Because concentrated winding machines are known to produce much higher losses in the rotor than distributed winding machines do, it was necessary to capture this in the analysis. Rotor losses affect both the generator efficiency and the magnet temperatures, both of which can strongly influence the quality of a machine design. Induced rotor losses can be found using FEA tools; however, analytical methods have also been developed. The choice of calculation method is an important part of this thesis.
The full analysis should be able to predict the induced voltage, inductance, flux density levels, losses, temperatures, weights and costs. These parameters should then be the values used by the optimisation tool.

I had no intention of developing a self-created optimisation algorithm. I wanted to find one or more optimisation methods that were available to the majority of

machine designers and that did not require extensive knowledge of optimisation theory. Still, I recognised the need for training in optimisation theory, as I had no previous experience; therefore, I included two courses on optimisation in my academic training.
Most importantly, I needed an optimisation algorithm that could handle the difficult task of solving a problem with nonlinear constraints, a nonlinear objective, integer variables and numerous variables.

Finally, it was necessary to provide an optimisation tool that could be used in a way that would provide useful information for machine designers. A result that indicated only a single optimal generator design would not benefit anyone but a designer making a generator for the exact same specifications as mine. Therefore, it was important to illustrate how the optimal design and the minimum cost would change with varying parameter values. The most important parameter for this purpose is the gear ratio (generator speed).

1.3 Structure of the thesis

Chapter 2 of this thesis includes an introduction to marine current turbines and a technology review covering different turbine types and drive-train topologies.
Chapter 3 is a brief introduction to PM machines, which provides the rationales behind the choices of different machine types. It also discusses the main design relations between the various design variables and the machine performance.
Chapter 4 is the analysis chapter, which presents a description of all calculations performed as part of the thesis work. Magnetic, electric, loss, thermal and cost analyses are included. The calculations of the stator yoke flux patterns and the induced losses in magnets are particularly emphasised.
Chapter 5 is an introduction to optimisation methods. The two methods chosen for use in this research are described in detail.
Chapter 6 presents the optimisation results. It is split into two sections, one for each of the optimisation methods.
Finally, Chapter 7 presents the conclusions of this thesis, along with recommendations for future work.

1.4 List of publications

Journal papers:

- A. Røkke and R. Nilssen, 'Marine current turbines and generator preference. A technology review', in *Renewable Energy and Power Quality Journal*,vol. 11, no. 299, Mar. 2013.

- A. Røkke and R. Nilssen, 'Analytical calculation of yoke flux patterns in fractional-slot permanent magnet machines', *IEEE Transactions on magnetics*, vol. 53, no. 4, pp. 1-9, 2017.

Conference papers:

- A. Røkke and R. Nilssen, 'Gradient based optimization of permanent magnet generator design for a tidal turbine', in *2014 International Conference on Electrical Machines (ICEM)*, Sep. 2014, pp. 1199-1205
- E. L. Engevik, A. Røkke and R. Nilssen, 'Evaluating hybrid optimization algorithms for design of a permanent magnet generator', *Joint International Conference on Electromotion(ACEMP-OPTIM)2015*, Side-Turkey, Sep. 2015, pp. 711-718.
- A. Matveev and A. Røkke, 'Power take-off for tidal turbines providing lowest cost of energy', *Proceedings of the 10th European Wave and Tidal Energy Conference*, Sep. 2013.

Conference paper not directly related to the main content of the thesis:

- E. Severson, A Røkke, R. Nilssen, T. Undeland, and N. Mohan. 'Design and measurement of a passive thrust magnetic bearing for a bearingless motor.' In *Industrial Electronics Society, IECON 2013-39th Annual Conference of the IEEE*, pp. 2720-2725. IEEE, 2013

Chapter 2

Marine current turbines

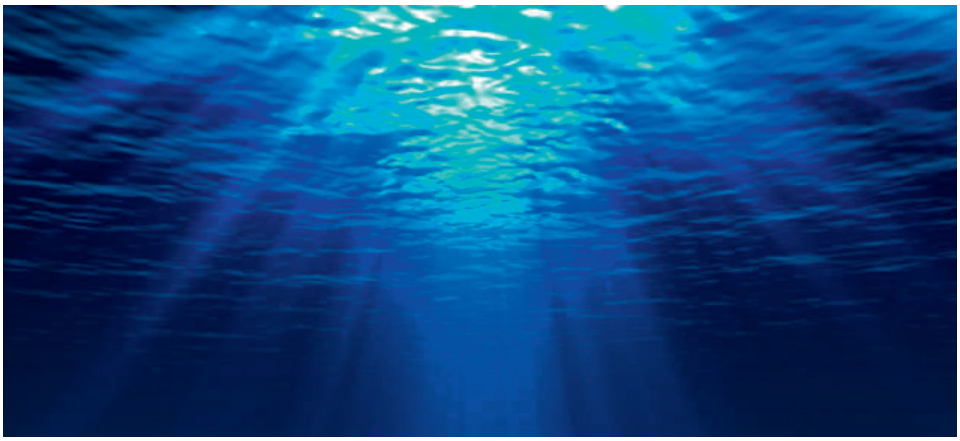

2.1 Introduction

This chapter discusses the potential of marine current energy sources and illustrates various concepts of turbine functionality. A technology review performed in 2012 and presented at the International Conference on Renewable Energies and Power Quality (ICREPQ' 13) constitutes the main part of this chapter. The technology review focuses on generators and drive trains. The chapter concludes with the chosen design specifications for a tidal turbine generator.

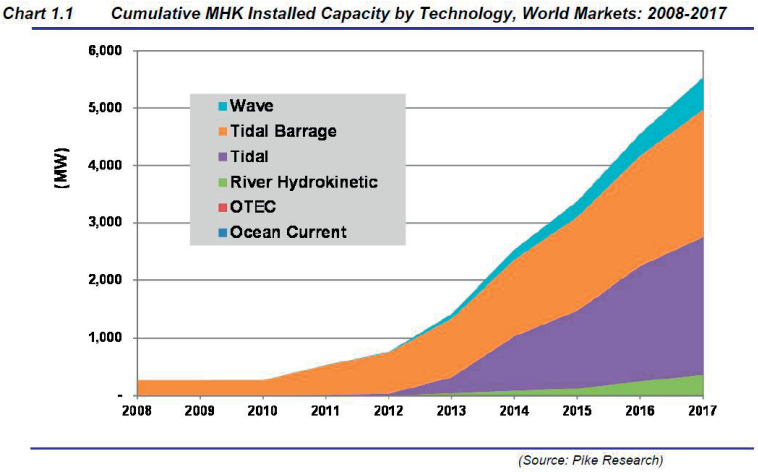

Figure 2.1: Predicted cumulative installed ocean power capacity. Source: [3]

2.2 Marine currents

Rivers, tidal currents and global ocean currents are all different forms of marine currents. Tidal currents represent the largest potential source of energy exploitable for electricity production. The UK possesses the most plentiful tidal resources in Europe [1], with a potential of approximately 21 TWh per year, exploitable by devices that are currently under development. This represents nearly 6% of the UK's annual electricity consumption (in 2009) [2]. In the quest to replace fossil-fuelled power plants, new renewable power production routes must be developed, and marine current power is one of the fields that is expected to grow in the coming decades. Pike Research [3] has issued a prediction regarding the installed ocean power capacity, as shown in Figure 2.1. This cumulative ocean power includes wave energy, energy from tidal barrages (enclosed, dam-like structures), tidal energy, kinetic energy in rivers, ocean thermal energy conversion (OTEC) and energy from ocean currents.

Th extraction of kinetic energy from marine currents can be compared to the extraction of kinetic energy from the wind. Water has a higher density than air and consequently has a higher energy density. However, the speeds at which water moves in tidal currents and ocean currents are less than the wind speeds utilised by wind turbines.
The power available from moving water is

$$P = C_P \frac{\rho A v^3}{2} \tag{2.1}$$

where C_P is the turbine power coefficient, ρ is the density of the water, A is the sweep area of the turbine, and v is the velocity of the flow. The turbine power coefficient depends on the turbine design.

Although tidal energy is still far more expensive than energy from other renewable sources, such as wind power, solar power and hydropower, it is likely to be a necessary part of the energy mix if the world is to reach a carbon-neutral state. This is why government funding is being used to support the development of marine current energy converters.
The marine current industry is still in the development stage. The first turbine with a permanent connection to the public grid was connected in Hammerfest, Norway, in 2004. New concepts emerge yearly. In January 2016, the European Marine Energy Centre (EMEC) presented a list of 120 different tidal energy concepts [4]. Most of these are currently in the proof-of-concept or prototype stage, but a few are already commercial products. [5] suggests that "the tidal power industry can be likened to the wind industry in the seventies, when a plethora of concepts were competing for supremacy."
The development of tidal energy technologies has been pushed by EMEC, a test and research centre in the Orkney Islands, and several national renewable energy centres.

2.3 Power train options

There are many technologies that can potentially be used to convert the kinetic energy of water into electricity for use in a public grid. An overview of various combinations of these technologies can be seen in Figure 2.2.
A directly driven solution uses no gears and has the advantages of low mechanical stiffness, no gear loss and high reliability. The disadvantage is that such a generator is large and expensive with a relatively low efficiency. Single-stage gear trains are more reliable than multiple-stage gear trains, but they have a lower gear ratio, and consequently, the generator becomes relatively large. Because of the low speed of a tidal turbine, a high gear ratio must be used if a conventional induction generator is to be applied, whereas both wound-field and permanent magnet generators can run on medium-speed gears.
A fixed-speed generator suffers the drawbacks of low energy capture, high mechanical stress, poor power quality and no control of the reactive power. Instead, voltage source inverters are used to transform the variable frequency of the generator to the grid frequency.
A doubly fed induction generator or a brushed synchronous generator requires a brush system to excite the rotor. Because of the accompanying maintenence re-

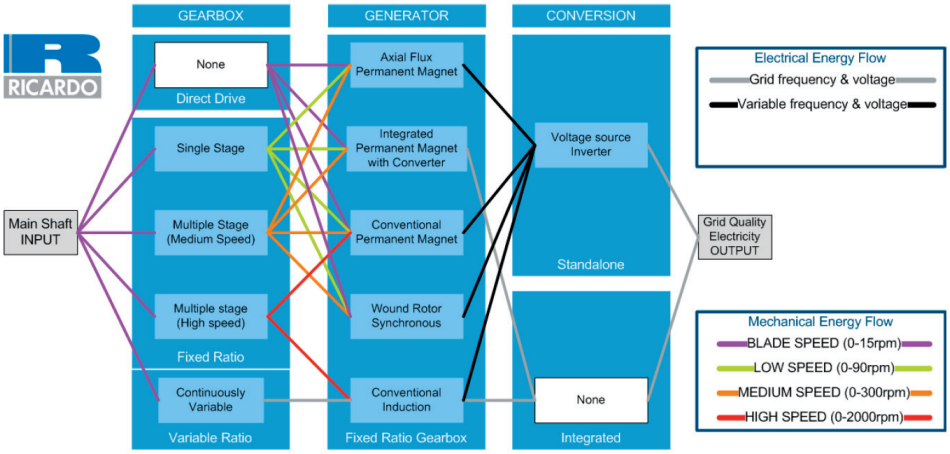

Figure 2.2: Drive train options [8]

quirements, this is not viewed as a viable option for tidal turbines [6].
A brief overview of the most common generators for tidal energy applications was presented by Magagna & Uihlein in [7].

2.4 Literature

The purpose of this section is to provide an overview of the present marine current industry to serve as a basis for a plausible set of design specifications for a generator. Several other publications [9]–[17] have described turbine technologies, but without presenting the details of the drive train. In [5], several turbine technologies are presented and discussed. The drive train is briefly discussed, but the authors found little information regarding the choices of gears and generators. Since 2012, additional literature has been published concerning drive train options and power take-off methods [6]–[8], [18]

2.5 State of the art

Energy converters developed for marine currents are used in tidal currents, river streams and ocean currents. These are all harsh marine environments and demand robustness, cost-effectiveness and limited maintenance time.
Tidal energy can be harvested in one of two ways: either by building a barrage across a bay or an estuary and taking advantage of the difference in head or by extracting kinetic energy from free-flowing water. Because of its considerable influence on the ecosystem, the number of locations at which the first option is

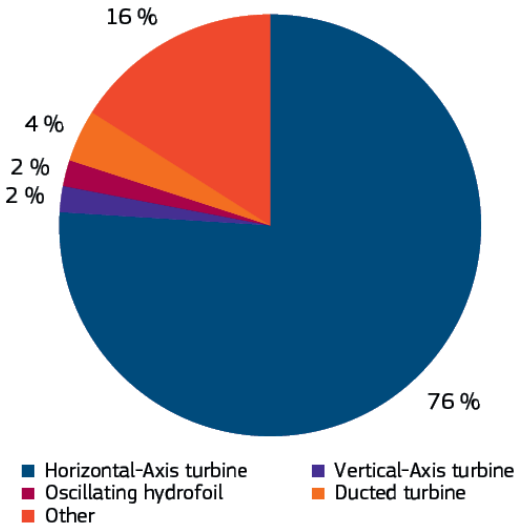

Figure 2.3: Distribution of R&D efforts focused on different types of tidal technologies. Sources: [7], [19]

feasible is limited; hence, the second option is investigated here. Because of space limitations, not all devices can be presented. Thus, the devices that appear most promising and are most fully developed are included. The information has been gathered from major developers of marine current energy devices, mainly from their respective web sites.

Figure 2.3 shows the distribution of research efforts pursuing the different turbine types (as of 2013) that are presented in this chapter. It is clear that the horizontal-axis turbine is currently the most extensively investigated, and it is the turbine type that is most likely to be chosen for widespread use in the future.

2.5.1 Cross-axis turbines

A cross-axis turbine may have either a vertical axis (see Figure 2.5) or a horizontal axis (Figure 2.4).

Ocean Renewable Power Company has designed a modular turbine system with horizontal-axis Darrieus turbines (Figure 2.4). Small versions can be installed in rivers, larger versions are available for shallow tidal streams, and the largest version is designed to be installed at deep-water tidal or ocean current sites. The turbines directly drive a permanent magnet generator, with no intervening gears.

One advantage of a vertical-axis turbine is that the water flow direction does not influence the output of the turbine. It is also possible to simplify the maintenance

Figure 2.4: Ocean Renewable Energy's turbine system, TidGen® [20]

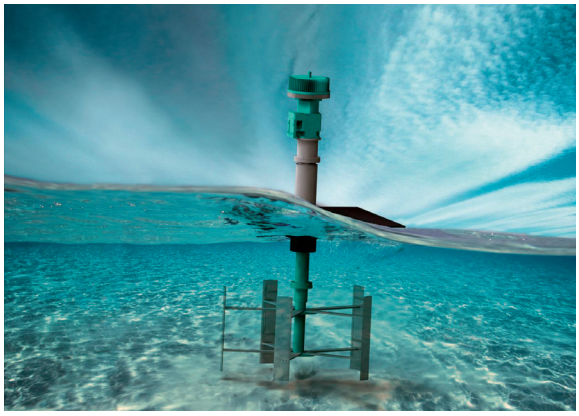

Figure 2.5: A vertical-axis tidal turbine [21]

by placing the main drive train above water. However, the performance of vertical-axis turbines has proven inferior to that of horizontal-axis turbines, and no device has yet been developed for use at the commercial scale in the tidal market. Instead, the focus is placed on smaller units located in rivers or other smaller water flows. Neptune Renewable Energy, which was established in 2005, developed a very different type of marine current energy converter with a vertical axis, called the Proteus. However, because of its poor performance, the company went into liquidation in 2013.

2.5.2 Oscillating hydrofoils

The vertically oscillating movement of a horizontal blade is utilised in the Pulse Tidal generator shown in Figure 2.6. Similar to a horizontal cross-axis turbine, the swept area is rectangular rather than circular, which is beneficial for shallow sites [22]. The power is transmitted hydraulically to a gearbox and a generator housed in a steel nacelle above the waterline [16]. However, both Pulse Tidal and another

Figure 2.6: The Pulse-S stream generator [22]

company that developed a similar turbine, IHC Engineering Business, are now out of business.

2.5.3 Enclosed tips (ducted)

Several ducted turbines are being developed, all of which seem to be gravity-based, i.e., mounted on the seabed. The only turbine of this type that has reached the commercial stage is OpenHydro's Open-Centre Turbine, shown in Figure 2.7. This is a bidirectional symmetrical turbine with an open centre, and the rim of the duct contains a gearless permanent magnet synchronous generator. OpenHydro is currently planning the installations of two of the first grid-connected tidal arrays, one in France and one in Canada.

2.5.4 Horizontal-axis turbines

The majority of marine current energy devices that have reached commercialisation are horizontal-axis devices in some form [17]. Within this category, however, there is a high degree of variation.
Devices with different mooring options include seabed-mounted devices, floating devices and buoyant devices that float between the surface and the seabed. The most common option is for a single turbine to be mounted alone; however, other designs involve two or more turbines mounted on the same structure.
Seabed-mounted turbines are often referred to as first-generation devices. They can only be used at relatively shallow water depths. For deep sites, floating devices are most attractive because the water speed is fastest close to the surface.

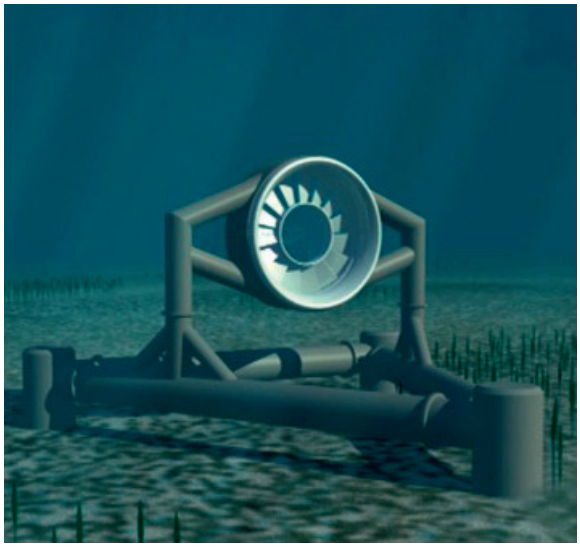

Figure 2.7: The Open-Centre Turbine [23]

Figure 2.8: AR turbine by Atlantis Resources [24]

Figure 2.9: HS1000 turbine by Andritz Hydro Hammerfest [25]

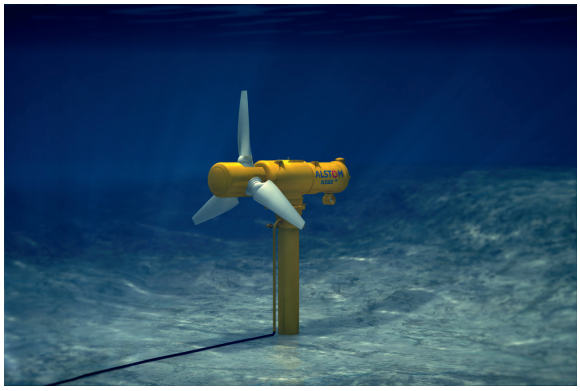

Figure 2.10: Oceade turbine by GE & Alstom Energy [27]

Single seabed-mounted turbines

Atlantis Resources Corporation's AR turbine (Figure 2.8) has three blades and is fitted with a two-stage gearbox, a permanent magnet generator and a variable speed drive [7]. The base of the turbine has a rotating mechanism and turns as required with each tidal change [24]. A similar turbine is Andritz Hydro Hammerfest's HS1000 (Figure 2.9). It is also a three-bladed turbine, but it adapts to the changing tides by pitching its blades [25]. The turbine is fitted with an induction generator and a three-stage gearbox. GE & Alstom Energy are currently offering a tidal turbine platform called Oceade (Figure 2.10). The turbines have pitching blades and a yawing nacelle, and no information is available about the chosen generator and gear technology. However, the 500 kW prototype made by Tidal Generation Ltd. was equipped with a gear and an induction generator [26].

Voith Hydro has developed a slightly different three-bladed turbine; see Figure 2.11. The blades do not pitch, and there is no yaw mechanism; it is designed to be

Figure 2.11: Voith Hydro's direct-drive turbine [28]

bidirectional. A permanent magnet generator is directly driven, without the use of a gear [28].

Multiple seabed-mounted turbines

In 2015, Tocardo aquired Swanturbines' intellecual property, including a turbine similar to Voith's in that it has a direct drive and utilises a permanent magnet generator and bidirectional reversible rotor blades. However, it has only two blades, and it is smaller; the 1.2 MW design includes five turbines mounted on a common structure.

MCT/Atlantis chose a seabed-mounted structure for their SeaGen S system (Figure 2.12). Two two-bladed turbines are mounted on a crossbeam on a surface-piercing tower support structure that can raise the turbines above the water for repairs and maintenance. The blades are pitch-controlled, and mechanical energy is transferred through a gearbox to the induction generator [30].

Another device comprising several turbines is Delta-Stream, developed by Tidal Energy Ltd. Three three-bladed turbines are mounted on a single, triangular frame (Figure 2.13). The hub of each turbine has a yaw mechanism, and the turbines are connected through a gearbox to an induction generator.

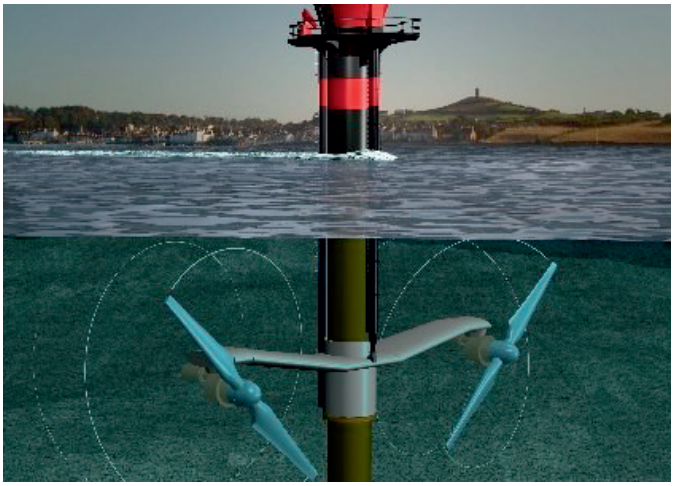

Figure 2.12: MCT/Atlantis' SeaGen S system [29]

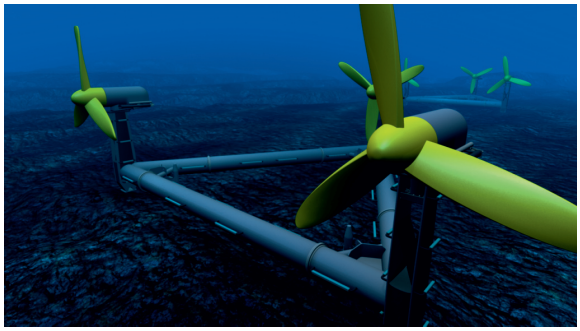

Figure 2.13: DeltaStream by Tidal Energy Ltd. [31]

Figure 2.14: Twin version of Oceanflow Energy's Evopod [32]

Floating turbines

Floating marine current turbines are intended for use in deep waters and are often referred to as second-generation devices. They may be totally submerged, or part of the structure can float above the water (Figure 2.15). Such a device usually does not require a yaw mechanism, as the tide will pull the turbine into the correct position. Floating devices are more readily accessible than seabed-mounted ones, which is a significant advantage that can reduce maintenance costs. However, the mooring of the device to the seabed is challenging.

Oceanflow Energy's three-bladed Evopod comes in single-, twin- (Figure 2.14) and multiple-turbine versions. The structure floats partly above the water. The blades are fixed, and the swivel mooring and power export solution is disconnectable. The power train includes a gear and a permanent magnet generator.

Scotrenewables' marine current turbine consists of a steel tube that floats on the surface of the water and two two-bladed rotors mounted on arms that fold up next to the tube in especially rough weather and during transportation (Figure 2.15). It has a passive yaw system and fixed-pitch blades. The power train includes a gearbox and an induction generator. In early 2016, the company is building a 2 MW turbine that will be the largest tidal turbine in the world when it is finished.

CoRMaT, the tidal generator developed by Nautricity, has a turbine with two closely spaced contra-rotating rotors. This produces a lesser wake effect, causing less environmental impact and permitting an increased device density [36]. The device is neutrally buoyant and has a passive yaw. Within the nacelle, there is a flooded permanent magnet generator, which is driven by the two rotors. The relative speed within the generator is twice that of each of the rotors, reducing the

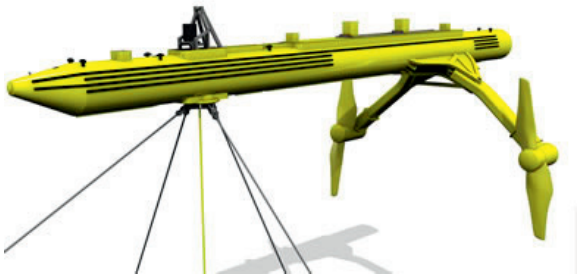

Figure 2.15: Scotrenewables turbine with two rotors [33]

torque requirement and therefore the size of the generator.

2.5.5 Tidal kites

A marine current energy device that is significantly different from the rest is Minesto's Deep Green concept. It is a turbine that is attached to a wing (Figure 2.16), which moves in loops through the water, and is also attached to the seabed by a moving wire, similar to a kite [34]. The device moves through the water at a speed significantly higher than that of the water, thereby reducing the torque per unit of power, and hence also the weight and cost of the drive train, compared with other device types. According to [16], a 1 m diameter turbine can generate 500 kW, whereas a fixed turbine with the same capacity would be 30 m in diameter. The Carbon Trust's Marine Energy Accelerator project [2] states that "the device is sufficiently different from competing designs to potentially offer either a significantly lower cost of energy, or the ability to exploit an entirely new resource". The generator is gearless. The type of electrical generator used has not yet been revealed.

2.5.6 Archimedes screws

Flumill's Archimedes screw turbine has two counter-rotating helical screws and is slowly rotating. It is naturally buoyant, and the flow and ebb of the tide itself causes its position to shift. The turbine gearlessly drives a permanent magnet synchronous generator [36]. A pilot project was planned for installation in 2015, but because of a lack of funding, building had not yet begun by the end of 2015.

2.6 Conclusion

Technologies
It seems clear that the tidal industry is moving towards one preferred turbine type,

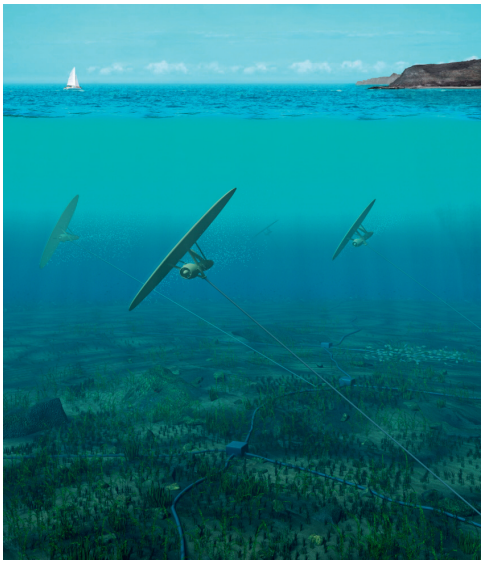

Figure 2.16: The Deep Green turbine by Minesto [35]

Figure 2.17: Flumill's Archimedes screws [36]

namely, the horizontal-axis turbine. Exeptions include OpenHydro's enclosed tip turbine and Minesto's tidal kite. Three-bladed turbines are most common; however, several two-bladed turbines are also on the market. Some first-generation turbines, which are mounted on the seabed, have already reached commercialisation and are being used to establish the first tidal energy arrays.
Permanent magnet generators and induction generators are the two preferred generator technologies. In direct-drive systems, permanent magnet machines are applied. For geared machines, both types are used. Most turbines are geared. Few specifications can be found regarding the gear type, but both two- and three-stage gear trains have been identified.

Challenges
The marine current industry is in an early stage of development. The business is characterized by the building of prototypes and the proposal of new ideas. In such a setting, reliability is of great importance. Manufacturers do not wish to deploy a new tidal turbine in the sea for the first time only to find that the generator does not work properly. This is a significant risk if the generator itself is also a prototype. However, some marine current turbines require properties that are not common among off-the-shelf products. In addition, the optimal combination of compactness, high efficiency and high reliability throughout the product's lifetime may not be available in thoroughly tested machinery. Manufacturers therefore face a trade-off between risking a malfunction in the generator and using a generator that is not optimised for the turbine. This technology review shows that different manufacturers choose different strategies. Companies that take the more risk-averse approach may wish to alter their drive train designs once turbine functionality has been proven. Then, they can focus on optimising the rest of the system.

Because marine current energy converters are submerged and are often located far from docks and workshops, it is of the utmost importance to design a system that requires as little maintenance as possible and has the lowest possible risk of failure. This is a problem for all turbine components, and manufacturers attempt to keep the number of high-risk components to a minimum. These include all moving parts, such as seals, gears, and breaks. Machines with brushes are not desirable in such underwater structures because brushes are a common source of failure, although brush quality has improved greatly in recent decades.

2.7 Case Study

The generator chosen for optimisation in this work is intended for use with a horizontal-axis turbine. The two main parameters of the design specifications are power and speed. Based on the technology review performed at the start of this

Table 2.1: Design specifications

Turbine power	1.5 MW
Generator speed	15-1050 rpm
Number of phases	3
Line-to-line voltage	3.3 kV
Maximum outer diameter	3.5 m

project, the chosen power rating of the generator is 1.5 MW. This is a typical size for turbines manufactured for commercially ready arrays. The power rating typically varies from 1 to 2 MW. The rated speed for this type of turbine can be approximately 15 rpm. The rated speed for the generator will range from 15 rpm (direct drive) through 80 rpm (one-stage gear train) up to 1050 rpm (three-stage gear train). In Chapter 4, in which the analysis of the generator is presented, generators with one-stage gear trains are considered as examples. A one-stage gear train is more reliable than a multi-stage gear train and requires less maintenence. The generator size will be smaller than for a direct-drive solution and larger than for a multi-stage gear solution. The focus of the investigations is a surface-mounted permanent magnet three-phase machine with a voltage rating of 3.3 kV. A report published later [6] shows that voltage ratings vary between 400 V and 13.8 kV, with 6.6 kV and 11 kV being the most common voltage levels.

Chapter 3

Permanent magnet generators

1

[1]Figure from Rolls-Royce Marine AS Trondheim

3.1 Introduction

Electrical machines have been used since the 19th century to convert energy from mechanical power into electrical power (i.e., electric generators) or from electrical power into mechanical power (i.e., electric motors). In 1831-1832, Michael Faraday discovered the operating principle of electromagnetic generators. Since that time, electrical machines have evolved dramatically, giving rise to a large family of machine classes that are used in all sorts of equipment. Electrical generators are typically alternating current (AC) machines and may be either induction generators or synchronous generators. In recent decades, interest in PM machines has been growing because of their high power density, high efficiency and good low-speed capabilities.

Electrical machines are responsible for nearly all electricity production throughout the world (except for that from solar cells). Additionally, approximately 60% of all electricity is consumed by electrical machines. If the general efficiency of electrical machines and generators could be improved, it would have a substantial effect on the world's energy consumption. Efforts to design machines with low losses not only result in high-quality products but also can help to achieve a suitable energy balance in a world in which the number of people in need of electric power is continuously increasing.

This section briefly introduces PM machines, identifies several factors that drive the size and cost of generators, and describes the difference between concentrated windings and distributed windings. This is followed by a discussion on how these winding types can be compared. The cooling system for a generator of the type in question is briefly discussed, after which the main specifications for and constraints relevant to a PM generator for a tidal turbine are presented.

3.2 Main categories of PM generators

PM machines come in many shapes. There are numerous design options among which to choose, and the best choice will always depend on the application. The following are some of the main classifications of PM machines:

- Axial flux or radial flux
- Slotted or slotless stator
- Inner rotor or outer rotor
- Surface-mounted or interior rotor magnets
- Distributed or concentrated windings

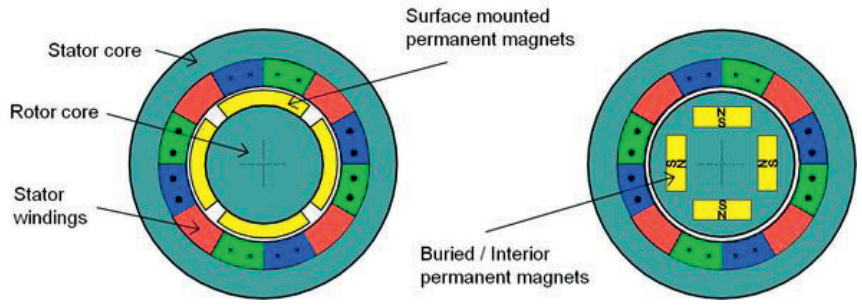

Figure 3.1: Surface and interior magnet machines. Source: [38]

In a marine current turbine, the water flow around the central shaft is disturbed if the generator diameter is too large; hence, an axial flux generator, which is well suited for large-diameter designs, is not well suited for this purpose. However, an axial flux machine with as many as 7 rotor disks and 6 stator disks has nevertheless been designed for the Scotrenewables Tidal Turbine [37], although it has not been implemented. Axial flux machines perform well in applications in which the machine can be shaped like a disc. When the diameter must be relatively small, the necessary numbers of stator and rotor disks can be high, and the amount of winding material used in the end windings compared with the active area becomes large, resulting in high cost and low efficiency. Therefore, the turbine generator chosen for consideration in this study is a radial flux machine.
Outer rotor machines can be beneficial in some cases, such as in wheel motors. However, because of the simple mechanical structure considered here, an inner rotor is chosen.
An ironless machine has the benefit of zero cogging torque and a low weight. However, the torque density is also usually low because of the large effective air gap. A traditional slotted design is chosen here.

The permanent magnets can be either mounted on the surface of the motor or buried in the rotor structure; see Figure 3.1. With buried magnets, the flux weakening capabilities are very good. Such a design is suitable for high-speed applications and electric vehicles. In a tidal turbine, however, the peak torque occurs at the peak speed; hence, flux weakening is not a concern. Because of the simpler assembly procedures for surface-mounted magnets, this latter approach is chosen here.

The windings can be either concentrated, in which case coils are wound around every tooth or every other tooth, or distributed, in which case the sides of a single coil are placed several slots apart. Concentrated coil windings are easier to manufacture and assemble, and they have shorter end windings. Distributed windings usually have lower rotor losses and better winding factors. Both concentrated and

distributed winding machines are considered here. A more in-depth discussion about winding types follows later in this chapter.

3.3 Main design elements

3.3.1 Rotor design

Number of poles

The number of poles in a machine affects several aspects of the machine's performance. A high number of poles results in a small magnet pitch and a low magnetic flux through the stator and rotor yokes. The yokes can therefore be thin, which is beneficial for reducing the weight and cost of the machine. Studies have typically shown that the weight and cost of a machine decrease with a decreasing number of poles [39], [40].
However, the performance is reduced if the number of poles is too high. Narrow magnets will have a relatively high pole-to-pole leakage flux. Narrow stator slots will have a low fill factor, thereby reducing the torque density of the machine. For a given speed, the frequency is proportional to the number of poles and is limited by the maximum allowed converter frequency. Large numbers of poles also result in high frequency-dependent losses, reduced efficiency and high temperatures.

Magnetisation and magnetic loading

The magnetisation of a machine is determined by the magnet dimensions and the air gap length. A machine with thick magnets (in the magnetisation direction) will have a high air gap flux density and high magnetic loading. Wide magnets also contribute to a higher magnetic loading. The size of the machine is inversely proportional to the magnetic loading. The price of the magnet material per unit weight is much higher than the prices of the other materials in the machine. A large magnet volume will lead to a relatively small machine, which, in itself, is cost-effective; however, the cost of the magnet material will be high.
An excessively high magnetic loading can cause saturation. To avoid saturation, the yoke thicknesses must be increased, at the expense of increasing the weight and cost of the machine. The tooth width must also be increased, at the expense of decreasing the slot width and the electric loading.

3.3.2 Stator design

Stator bore diameter

Both the torque and the weight are proportional to the square of the stator bore diameter. Optimisation routines usually find that the lowest cost or weight per Nm is achieved with the largest possible diameter [40], [41]. However, when the

diameter becomes too large, the active length becomes small relative to the end winding length, and the efficiency is consequently reduced. The outer diameter is often limited by spatial constraints.

Armature and electric loading

The size of the machine is inversely proportional to the electric loading.
The amount of electric loading is determined by the ratio of the slot width to the slot pitch, the slot depth, the fill factor and the current density. Deep slots result in high electric loading but also a high slot leakage inductance. Slots that are wide compared to the slot pitch result in high electric loading but leave less space for the magnetic flux to pass through the teeth, which can cause tooth saturation and high iron losses. At a given current density, the windings in large slots will become hotter than the windings in small slots, potentially inducing hot spots with temperatures above the allowed limit.
For a given slot dimension, a higher current density results in higher electric loading but also causes copper loss and higher hot-spot temperatures.
High electric loading results in high reactive voltage drops and low power factors.

Winding layout

The winding layout of a machine strongly affects its performance. The winding configuration depends on the numbers of slots and poles and on the number of layers in a slot. Machines with similar numbers of poles and slots are made with concentrated windings, whereas machines with more than 1.5 times as many slots as poles are made with distributed windings.
The winding layout determines the winding factors and the harmonic content of the armature field. Harmonics that do not have the same number of poles as the machine does induce losses in the rotor and cause leakage inductance. The length, loss and weight of the end windings are also determined by the winding layout.

Concentrated windings
Fractional-slot concentrated non-overlapping windings (FSCWs) consist of coils wound around single teeth. The coils are compact, and the end winding volume is minimised. The coils can be premade and can also be pressed before insertion to increase the fill factor and improve their thermal conductivity. Single-layer concentrated coils are wound around every other tooth, whereas double-layer concentrated coils are wound around every tooth, as illustrated in Figure 3.2. Single-layer windings often have a higher distribution factor than do double-layer windings. The automatic insertion of concentrated coils into slots is easier with single-layer coils than with double-layer coils. Other advantages of single-layer coils include a negligible flux linkage between phases and physical separation between the coils,

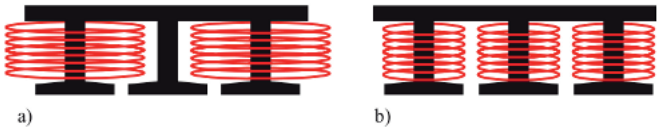

Figure 3.2: Single-layer (left) and double-layer (right) concentrated windings [42]

resulting in a fault-tolerant design. The main disadvantage of single-layer concentrated coil windings is that they often produce high levels of subharmonic magnetic field content. This can cause considerable rotor loss and a large air gap leakage inductance. Vibrations due to the subharmonics can also be an issue.

Distributed windings
In this thesis, the term distributed windings (DWs) is used for all overlapping windings. The coil pitch in a DW machine is greater than one, which means that each coil is wound around multiple teeth. Figure 3.3 shows a machine with concentric distributed windings. This is a single-layer winding layout. In single-layer DW machines, the end windings must be shaped to accommodate the overlappping of the coils. Typically, at least two different coil shapes are used. This increases the production cost of the machine.
A machine with double-layer windings typically has only one coil shape, as in Figure 3.4. DWs are often short pitched, i.e., the coil throw is less than one *pole pitch*. Short pitching reduces the length of the end windings and the harmonic distortion but also reduces the main winding factor.
A machine with DWs is equipped with several slots per pole. Therefore, the slots can be very narrow if the number of poles is high. This results in a low fill factor. DWs have longer end windings than do FSCWs. This incurs additional cost and weight, a higher end winding inductance and increased losses. The dissipation of heat in the end windings can often result in high temperatures because the thermal resistance between the end windings and the ambient environment is high. DWs can have a layout that creates minimal flux harmonics. The tooth width is often smaller than that in the case of concentrated windings. This leads to low PM losses.

3.3.3 Literature: comparing winding types

Some machine designers favour DWs, whereas others favour FSCWs. The two winding topologies both have advantages and disadvantages, and the best choice depends on the application. In [45], El-Refaie describes the main opportunities and challenges of FSCW machines.
Only a few studies have attempted to compare the two winding types for use in the

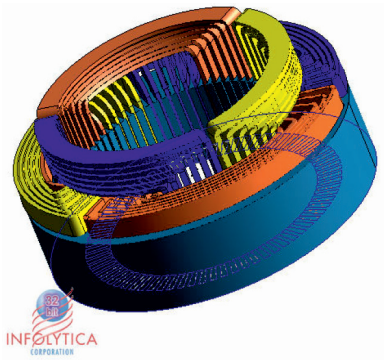

Figure 3.3: End windings of a single-layer distributed winding machine [43]

Figure 3.4: Double-layer distributed winding machine by ABB [44]

same application. This is a difficult task, as both FSCWs and DWs can be fabricated with a wide variety of slot-and-pole combinations, all of which have different properties. This is illustrated in [46], which investigates several different slot-and-pole combinations for FSCWs with open and semi-closed slots and with embedded and surface-mounted magnets. The torque capabilities and loss distributions are compared for the different topologies, and considerable variation is found.

In [47], comparisons are presented between an integer DW stator and three different FSCW stators for an induction machine. It is shown that in two of the FSCW machines, the torque produced is extremely low, and high harmonic contents induce high rotor losses in the third FSCW machine. Of the four investigated stators, only the DW stator is found to be suitable for the induction rotor.

Several studies have investigated the advantages and disadvantages of FSCWs and DWs for use in traction applications at a wide range of speeds with the use of flux weakening [48]–[52]. [50] presents a comparison of a DW design and an FSCW

design for a 4-pole machine with flux weakening. The saliency ratio, the induced voltage and the torque are lower in the FSCW machine, but the losses are also lower. The authors cannot claim to determine which of the two winding topologies is more suitable for the application, only which of the two specific machine designs is better. Firstly, the same rotor, the same outer radius, the same number of turns and the same active length are used in both configurations. These parameters may be better suited for one of the topologies, and if another set of parameters were to be chosen, the result could be different. Secondly, only one slot-and-pole combination is investigated for each winding topology. Because the number of poles is four, the possible choices for the number of slots are very limited. In a larger machine, many pole-and-slot combinations should be investigated before drawing a conclusion.

A similar comparison is presented in [49]. A 4-pole machine with the same rotor and four different stators, with both DWs and FSCWs, is designed to meet a given set of requirements, including field weakening. It is concluded that all stator types are capable of meeting the criteria and that they all have different advantages. The benefits of the FSCW machines include short end turns, compatibility with segmented stators, a low cogging torque and low stator core losses at high operating speeds. The two DW machines offer the advantages of a higher reluctance torque (i.e., opportunities for a lower magnet mass) and lower high-speed rotor losses. It is noted that the results could be improved if the stator and rotor designs were optimised simultaneously.
Similar conclusions are drawn in [48], in which the effects of surface and interior magnets are investigated along with the winding layout. The relatively high magnet losses in the FSCW machine are highlighted as a challenge facing FSCW machines.

In [51], a comparison between an FSCW design and a DW design reveals that the FSCW design can yield a higher torque for the same total length when the total length is small, but when the total length is relatively large, the DW design yields a higher torque.

Optimised machines with three different slot-and-pole combinations are compared in [52]. The application is a PM-assisted synchronous reluctance machine for use in electric vehicle traction. With the objective of maximising efficiency, the DW is found to show better performance because one of the two FSCW machines suffers high iron losses due to harmonics and other has a higher cogging torque. The comparison is fair because all three machines are optimised for the same objective and the same constraints. It is also noted that conventional approaches to optimisation, in which the same split ratio is employed for the different machines being compared, could yield a considerably different outcome.

The aim of the optimisation presented in this thesis is to enable a comparison in which no distinction is made between concentrated and distributed windings. The method used to achieve this purpose is to include the numbers of both poles and slots in the list of variables, thereby allowing the winding type to differ from one individual machine to another. *Thus, the transition from FSCWs to DWs is smooth, and the optimisation routine will search for the best individual design,* ***independent*** *of the winding type*. This is the main contribution of this thesis. The hypothesis is that the optimal slot-and-pole combination will change as a function of generator speed/number of poles. It is believed that FSCW generators should be more suitable for low speeds, whereas DW generators should be more suitable for high speeds. This is because at high speeds, the frequency constraint limits the maximum allowable number of poles, and distributed windings are well suited for low-pole-number machines.

3.4 Cooling

How a machine is cooled can be a decisive factor in choosing the electric and magnetic loading in the machine. In a submerged tidal generator, the ambient temperature is low (assumed to be $15\,^{\circ}\mathrm{C}$), and the temperature on the surface of the stator housing is approximately the same as the seawater temperature. The machine can be filled with either air or another gas or with a liquid with better thermal properties. In this study, an air-filled machine is considered, with a pressure of 5 bar. In submerged machines, it is beneficial to keep the interior pressure higher than the ambient pressure. Then, in the case of a small leak, air will seep out of the machine instead of seawater seeping in.
The cooling of the rotor can be either forced or passive. Forced cooling requires fans and heat exchangers. The generator considered in this study is assumed to be passively cooled. The speed of the rotor maintains a relatively high level of heat transfer between the rotor and the stator. The transmission of heat from the end windings to the surrounding air is low, independent of the speed.

3.5 Main constraints and specifications

The chosen generator specifications are based on the discussion presented in Chapter 2. The main characteristics of the generator are listed here:

- Radial flux machine

Table 3.1: Fixed parameters

Rotational speed	15-1000 rpm
Available power	1.5 MW
Air gap length, g	6 mm
Housing thickness	50 mm
Relative permeability of iron	2000
Relative permeability of magnets	1.05
Magnet remanence	1.2 T

- Inner rotor
- Surface-mounted magnets
- Slotted stator
- Three-phase machine
- Passive cooling
- Laminated stator and rotor yokes
- Current in the q-axis

Various optimisation strategies can be chosen for the optimisation of PM machines. One can choose to limit the number of variables by, for example, choosing a fixed magnet-width-to-pole-pitch ratio. However, the same ratio might not be optimal in both DW and FSCW machines, and consequently, fixing this type of parameter can result in a sub-optimal design. Instead, in this thesis, the number of variables is allowed to remain high, and their values are restricted as little as possible. The variable space (the number of possible combinations of variables) becomes large when this strategy is used. The problem with this strategy is that it is more difficult to search the entire variable space. Depending on the optimisation algorithm, it is necessary to choose the settings in a way that ensures that the variable space is sufficiently covered.

A few parameters are, however, held constant. One of them is the air gap thickness, g, which is set to 6 mm. This is a fairly large air gap. A large air gap is beneficial for reducing the cogging torque, induced rotor losses and radial forces, and it allows the machining tolerances to be kept relatively high, which reduces the production cost. However, although a larger air gap results in a lower torque density, this is true only to a certain degree. The effective air gap of a surface-mounted PM machine also includes the permanent magnet; hence, reducing the air

gap by one half would reduce the air gap magnetic reluctance not to one half of its original value but more likely to approximately 80-90%, depending on the magnet thickness. The air gap length is listed among the other fixed parameters in Table 3.1.
A NdFeB rare-earth magnet material is assumed to be used in the rotor poles. NdFeB materials have very high energy densities and are commonly used in large PM machines. The stator laminations are assumed to be fitted into a steel housing for mechanical rigidity and protection from the marine environment. For simplicity, the current is placed in the q-axis. This ensures the maximum torque per unit current in the generator.

Constraints are imposed on various parameters to prevent a machine design that cannot be manufactured in practice or will lead to unnecessary costs in other parts of the tidal energy system. These constraints are listed in Table 3.2.
With an insulation system of temperature class F, the lifetime of the insulation system will be suitably long if the maximum allowed hot-spot temperature in the windings is lower than $135\,^{\circ}\mathrm{C}$.
The maximum allowable flux densities in the teeth and yokes are chosen based on experience. Because rotor yoke losses are not considered, the rotor yoke flux density is set somewhat lower than the stator yoke flux density.

Table 3.2: Constraints

Constraint objective	**Constraint description**
Keep the generator size within the available space	Outer diameter less than 3.5 m Active length less than 3 m
Keep the converter cost down	Electrical frequency less than 200 Hz Power factor higher than 0.85
Ensure a long lifetime	Magnet temperature below 90 °C End winding temperature below 135 °C
Guarantee the rigidity of the mechanical structure	Tooth width at least 5 mm Stator and rotor yoke thicknesses at least 5 mm Shaft stress less than 30 MPa Magnet thickness at least 2 mm
Ensure feasibility of assembly	Magnet thickness no more than 100 mm Minimum distance between magnets 1 mm Winding width and depth at least 1 mm
Avoid magnetic saturation	Flux density in teeth below 1.6 T Flux density in stator yoke below 1.4 T Flux density in rotor yoke below 1.2 T
Avoid demagnetisation	Short-circuit magnet flux density at least -0.2 T

Chapter 4

Analysis

4.1 Introduction

This chapter presents the analysis of the electrical machine considered in this study. After the input parameters defining the machine are presented, the analytical calculation of all key parameters of the machine is described. A novel feature of the analysis is that it is independent of the winding type. For a given input, including the number of slots, the number of poles and the number of winding layers, an appropriate winding layout is found, and a magnetic analysis, an electrical analysis, a loss analysis and a thermal analysis are performed. The result of the analysis is a set of key machine parameters that describe the machine design. The outputs are the objective value (fitness) for the machine design and a vector containing the values of all parameters that are subject to constraints.
One of the main contributions of this thesis is presented in this chapter: a description of stator yoke flux patterns, including a simple method for predicting the combined stator flux from the magnets and the armature reaction.
The eddy-current losses in the magnets are identified as the physical phenomenon that is most difficult to calculate using analytical equations. Several methods of predicting eddy-current losses in magnets are presented, and the results are compared with the results of FEA.

4.2 Variable selection

The accuracy of the analysis is very important for the optimisation outcome. If the analytical calculations are inaccurate, the quality of the optimisation algorithm will not matter; the identified optimal machine design will not be correct.

For the analysis to be incorporated into an optimisation routine, it is necessary to

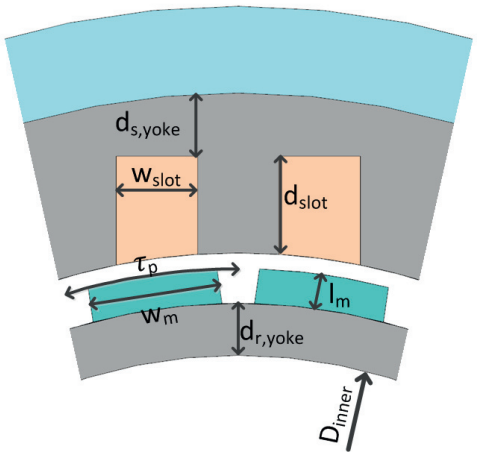

Figure 4.1: Geometric variables; parameter information is listed in Table 4.1

specify a set of input parameters that, together with a set of predefined quantities, uniquely describes the machine and its operation.

Twelve variables, or input parameters, are defined, of which 4 take integer values and the rest are real numbers; all of them are listed in Table 4.1. The geometric variables are illustrated in Figure 4.1. α_m is defined as w_m/τ_p, where τ_p is the pole pitch in metres. The number of winding layers may be only one or two, which are the traditionally used numbers of winding layers. The short-pitch factor is the number of slots by which the coil pitch is reduced compared with the pole pitch. Its value can be only zero, one or two; a larger short-pitch factor would result in a very low winding factor.

The active length is a function of other variables and is set to the length that is required to achieve the rated torque.

The machine model consists of four active components: the rotor yoke, the magnets, the stator yoke and the windings. The windings may be of the single-layer or double-layer type and may be either FSCWs or DWs. The magnets are mounted on the surface, and the rotor and stator yokes are made of laminated steel. Design details such as the pole shoes, slot wedge thickness and magnet shape are not subject to optimisation and therefore remain identical for all design variations.
The initial analysis is focused on generators with a one-stage gear train and a rotational speed of 80 rpm. In subsequent sections, the effects of varying the gear ratio are investigated.

Four different machines, illustrated in Figure 4.2, are used as examples throughout

Table 4.1: Optimisation variables

	Variables	
p	Number of pole pairs	**int**
$Q_p/2$	Number of slots per phase/2	**int**
N_{layer}	Number of winding layers	**int**
y_{sp}	Short-pitch factor	**int**
R_{inner}	Inner radius	m
$d_{s,yoke}$	Stator yoke thickness	m
d_{slot}	Slot depth	m
w_{slot}	Slot width	m
l_m	Magnet length	m
α_m	Magnet width/pole pitch	
$d_{r,yoke}$	Rotor yoke thickness	m
J	Current density (rms)	A/mm^2

this chapter. The investigated machines are not the results of any optimisation; they are merely used to verify the functionality of the analysis. Machines A and B are FSCW machines with the same numbers of slots and poles. Machine A is a single-layer winding machine, and Machine B is a double-layer winding machine. Machines C and D are DW machines with the same numbers of slots and poles. Machine C has one winding layer, whereas Machine D has two winding layers and a short-pitch factor of one slot. The sets of variables for all four machines are listed in Table 4.2. The analyses presented below address these four machines.

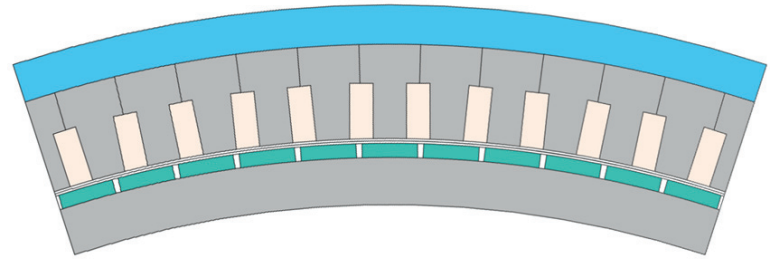

(a) Machine A

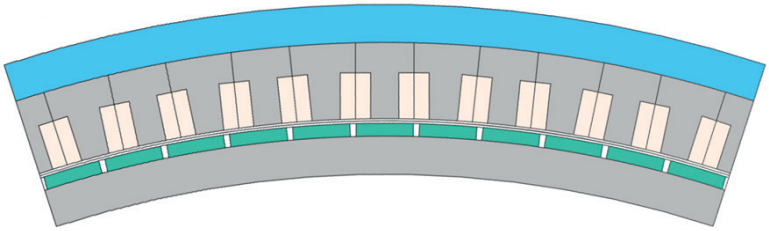

(b) Machine B

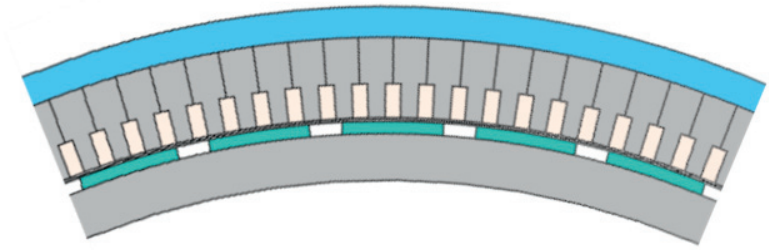

(c) Machine C

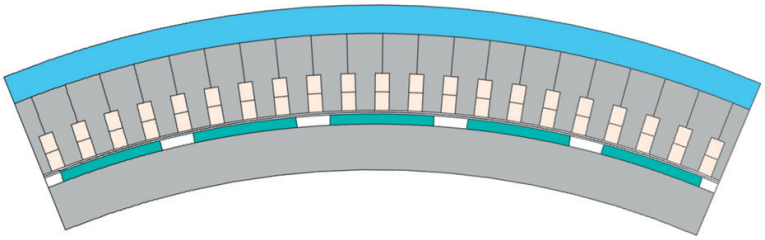

(d) Machine D

Figure 4.2: Geometries of Machines A-D

Table 4.2: Investigated machines

	Machine A	Machine B	Machine C	Machine D
p	55	55	20	20
$Q_p/2$	20	20	28	28
N_{layer}	1	2	1	2
y_{sp}	0	0	0	1
R_{inner} [m]	1.3	1.4	1.3	1.45
$d_{s,yoke}$ [mm]	50	40	75	70
d_{slot} [mm]	70	60	55	65
w_{slot} [mm]	30	40	25	25
l_m [mm]	18	17	20	18
α_m	0.9	0.9	0.75	0.75
$d_{r,yoke}$ [mm]	60	50	75	80
J [A/mm^2]	3	3.5	3	3.5
n [rpm]	80	80	80	80

4.3 Design layout

4.3.1 Defining winding types and base windings

The design of the winding layout is automated and depends only on the variables $Q = Q_p \cdot 3$, p, N_{layer} and y_{sp}. The number of slots per pole and phase is defined as

$$q = \frac{Q}{2pN_{ph}} = \psi + \frac{z'}{n'} \tag{4.1}$$

and is an important parameter in machine design. Here, Q and N_{ph} are the number of slots and the number of phases, respectively, and z' and n' are the winding numerator and denominator. If q is an integer, then the design is referred to as *integer winding*; otherwise, it is *fractional-slot winding*. The coil span, in slot pitches, of a full-pitch winding is $y_Q = Q/p$. The coil span, y, is chosen by rounding y_Q to the nearest integer of one or greater. If the short-pitch factor y_{sp} is greater than zero,

$$y = round(y_Q) - y_{sp} \tag{4.2}$$

The short-pitch factor cannot be equal to or greater than $round(y_Q)$. If it is, the design is rejected.
If the calculated coil span is 1, then the design is of the FSCW type, and each coil is wound around one tooth. Coil spans larger than 1 constitute DW designs.
If the denominator n' is an even number, then the winding is of grade 2; otherwise, it is of grade 1 [53]. The denominator of q is also used to find t, the periodicity,

Table 4.3: Winding parameters

	Machine A	Machine B	Machine C	Machine D
q	4/11	4/11	7/5 = 1+2/5	7/5 = 1+2/5
y_Q, y	1.09, 1	1.09, 1	4.2, 4	4.2, 3
W-grade	1	1	1	1
t	5	5	4	4
$Q*$	24	24	42	42
$p*$	11	11	5	5
Types	Fractional FSCW	Fractional FSCW	Fractional DW	Fractional DW

which is the largest common divisor of Q and p:

$$t = \frac{p}{n'} \cdot \text{ Winding grade} \tag{4.3}$$

The phase distribution of the machine is repeated n_{base} times in the winding layout. Depending on the winding grade, the numbers of slots and poles included in one base winding, $Q*$ and $p*$, respectively, are calculated using Equation 4.4. The periodicity within one base winding may be one or two, depending on the winding grade and the number of winding layers.

$$\begin{array}{lcc} & \text{if Winding grade = 1} & \text{if Winding grade = 2} \\ Q* = & Q/t & 2Q/(t \cdot N_{layer}) \\ p* = & p/t & 2p/(t \cdot N_{layer}) \\ t* = & 1 & 2/(t \cdot N_{layer}) \end{array} \tag{4.4}$$

The winding parameters for Machines A-D are listed in Table 4.3.

Infeasible slot-and-pole combinations

The numbers of poles and slots in a machine can never be equal. Therefore, if $Q = 2p$, the machine design is deemed infeasible.
The first condition of symmetry ([53]) states that

$$N_{layer}\frac{p}{n'} \in \mathbb{N} \tag{4.5}$$

Furthermore, to fulfil the second condition of symmetry, n cannot be divisible by the number of phases. Hence, if

$$\frac{n'}{3} \in \mathbb{N} \tag{4.6}$$

or if the first condition of symmetry is not met, then the machine design is deemed infeasible and rejected.

4.3.2 Winding layout

Professor Robert Nilssen has developed an automated winding layout routine based on winding routines described in [53] and [54]. The phases are distributed to achieve a high main harmonic magnetomotive force (MMF), and no slot is left vacant.

For double-layer windings and for concentrated non-overlapping windings, the routine is based on the star of slots theory. The electrical angle between each pair of adjacent slots, in degrees, is

$$\alpha_s = 360\frac{p}{Q} \tag{4.7}$$

Phase groups of 60° are implemented, such that all slots with a phase angle from 0° to 60° are of the R+ phase, those with phase angles lying in the next interval of 60° are of the -T phase, etc. Figure 4.3 shows the stars of slots for Machines A and B and for Machine D. The number next to each phasor is the slot number. One base winding contains 24 slots in Machines A and B and 42 slots in Machine D.

The star of slots method can also be used for winding distribution in single-layer DWs, but the end winding connections can turn out quite chaotic. In such cases, the method presented in [53] and [54] can be used to create coil groups of concentric coils that are easily produced and implemented. This method is used for Machine C, and Figure 4.4 shows the first 9 slot phasors. According to the star of slots, slot number 5 should belong to the +S phase. However, it is instead assigned to the -R phase. With this layout, the two coils of phase R will go from slots 1 and 2 to slots 5 and 6. The resulting main harmonic winding factor will be slightly lower with this winding distribution, but the winding assembly will be much simpler.

The described method yields the winding layout illustrated in Figure 4.5 for Machine C. The winding layout of Machine A is presented in the next section, in Figure 4.7.

4.3.3 Winding factor

Three factors contribute to causing the induced voltage of a phase winding to be lower than its maximum potential. One is the pitch factor, which is less than one if the pitch of a coil is unequal to the pole pitch. According to [53], the pitch factor

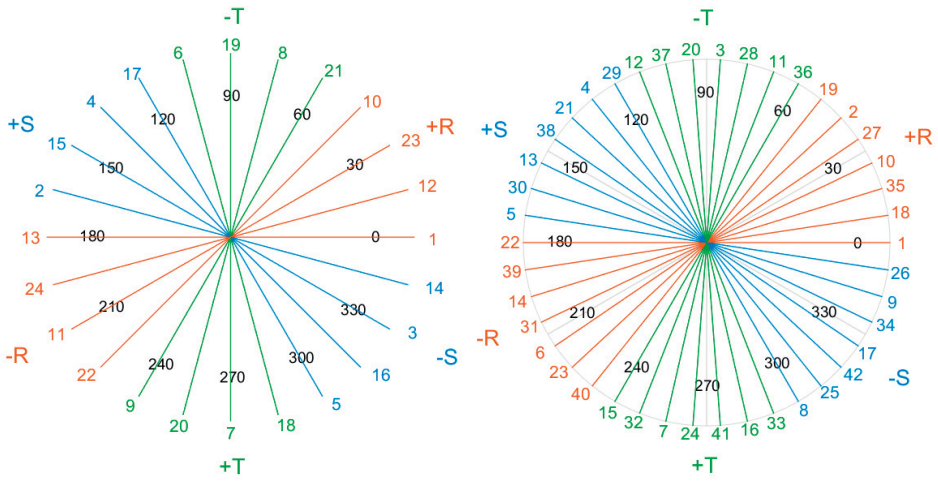

(a) Machines A and B **(b)** Machine D

Figure 4.3: Stars of slots

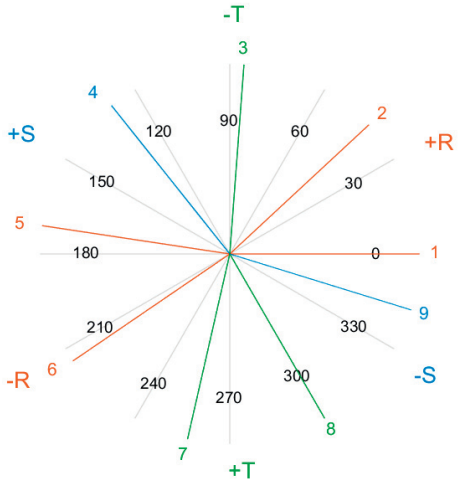

Figure 4.4: Star of the first 9 slots for Machine C

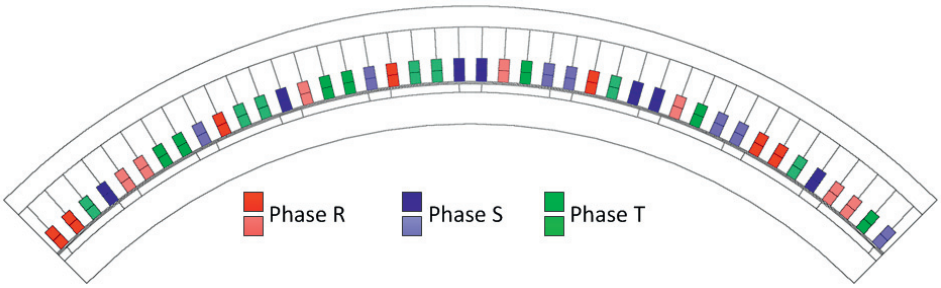

Figure 4.5: Winding layout of Machine C

of a winding is

$$k_p = sin(\frac{y}{y_Q}\frac{\pi}{2}) \tag{4.8}$$

The second is the distribution factor, which accounts for the fact that when several coil sides that are not of exactly the same phase are connected in series, the sum of the induced voltages is less than it would be if they were all of the same phase. In [55], the following equation is used for the distribution factor, k_d:

$$k_d = \frac{sin(\frac{1}{2}\sigma)}{\widetilde{z}sin(\frac{\sigma}{2z'})} \tag{4.9}$$

where $\sigma = \pi/3$ is the phase spread and

$$\widetilde{z} = \frac{N_c}{gcd(N_c, 2p \cdot N_{ph})} \tag{4.10}$$

Here, N_c is the number of coils; in double-layer windings, $N_c = Q$, whereas in single-layer windings, $N_c = Q/2$.
In single-layer overlapping windings, the coils are of unequal size, and they are distributed unevenly within the star of slots; hence, it is difficult to calculate the winding factor using general equations.
Instead, the slot phasors of all slots assigned to phase R in one base winding are summed, as illustrated in Figure 4.6. To obtain the winding factor, the following equation can be used:

$$k_w = \frac{U_{sum}}{u_1 Q*} \tag{4.11}$$

The third factor is the skewing factor. If the winding is of the fractional type, then the machine will have no skew. If the winding is of the integer type, then the rotor

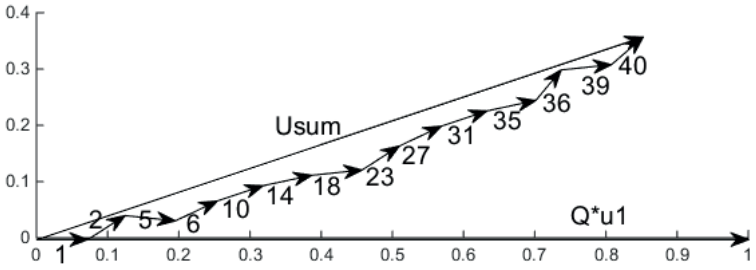

Figure 4.6: Vector sum for phase R in Machine C

Table 4.4: Winding factors

	Machine A	Machine B	Machine C	Machine D
k_p	0.9914	0.9914		0.901
k_d	0.9659	0.9577		0.9558
k_{sq}	1	1	1	1
k_w	0.9577	0.9495	0.9451	0.8612

poles will be skewed by one slot pitch, τ_s. The skewing factor is [53]

$$k_{sq} = \frac{\sin\left(\frac{\pi}{2}\frac{1}{N_{ph}q}\right)}{\frac{\pi}{2}\frac{1}{N_{ph}q}} \tag{4.12}$$

The winding factors of the investigated machines are listed in Table 4.4.

4.3.4 End windings

The length of the end windings depends on the winding layout. In FSCW machines, the end windings are short, and they are modelled as half-circles with an inner diameter equal to the tooth width. The average end winding length is

$$L_{EW} = \pi * \frac{0.67w_{slot} + w_{tooth}}{2} \tag{4.13}$$

For DWs, an end winding is modelled as two sections with mainly axial directions and one section with a mainly tangential direction. The lengths of the axial sections are set to 15 cm for all DW designs. The length of the tangential section is equal to the average coil throw times the slot pitch: $\overline{y} * \tau_s$.

4.4 Magnetic analysis

4.4.1 Introduction

The magnetic fluxes in the stator and rotor yokes of PM machines have two sources: the magnetic fields created by the PMs and the magnetic fields created by the current in the stator windings, namely, the armature reaction. Both of these sources create fields that vary with time and space. The time variation is caused by the rotation of the rotor and the time variation of the current in the windings. These fluxes vary with the electrical frequency, as determined by the rotational speed and the number of magnetic poles. However, they are not in phase, at least not in all parts of the yokes. This section shows how the PM flux and the flux from the armature together create flux patterns with considerable spatial variations.

The optimisation tool created in the course of this doctoral programme has undergone continuous development. In the first version, constraints were placed on the flux densities in the teeth and in the stator and rotor back yokes only for the no-load condition, consistent with the fact that the yoke thicknesses in PM machines are often chosen based on the no-load flux. The resulting optimal machines had a very high electric loading compared with the magnetic loading. The FEA results for these machines revealed some flux densities in the back yokes under load that were much higher than the specified constraints. This was caused by the flux produced by the stator currents.
In the next version of the optimisation tool, the armature reaction was included in the calculation of the machine fluxes. A literature study revealed that this is not a common practice in analytical calculations for PM machines. In the optimisation presented in [41], a constraint was imposed on both the no-load flux density and the armature reaction flux density, with the same value. It seemed probable that the fluxes from these two sources would not simply combine additively, as the magnets produce fields in the d-axis and the current produces fields in the q-axis.
Finally, an FEA model was used to study the stator yoke fluxes behind every slot, which revealed that the armature reaction flux did combine additively with the no-load flux at some positions. This investigation also revealed that the fluxes were not evenly distribute over time. Moreover, it was clear that the sum of the armature reaction flux and the no-load flux varied greatly and that this variation depended on the winding layout.
This section describes the methods used to find the no-load fluxes, armature fluxes and total fluxes. The flux patterns for all four machines are illustrated. This work has also been reported in [56].

Literature

Little focus has been placed on the calculation of the magnetic flux in a PM machine that is induced by the armature reaction. In 1993, a paper [57] was written on the instantaneous prediction of the air gap and magnet flux induced by the armature reaction, which included all harmonic contents. However, only the air gap and magnet region, not the stator yoke, was considered in the calculations.
An analytical technique is presented in [58] that is capable of predicting the on-load flux density waveforms in various parts of the stator of a PM machine. The technique relies on a lumped parameter model (LPM) and the sectioning of the stator teeth. However, the technique is applied only to an integral slot machine, and the focus is placed on the flux density waveforms in various parts of the tooth.
In [59], the stator flux and iron losses of a non-overlapping concentrated winding machine are investigated, but the stator yoke flux is measured at only one point, and the spatial harmonic pattern of the stator yoke is not studied.
The flux patterns in stators with fractional-slot non-overlapping windings are briefly mentioned in [60], and it is suggested that in a double-layer winding machine, portions of the stator yoke can be reduced because some parts are less used by the flux than others. Only armature reaction fluxes are shown. In this section, it will be shown that when the no-load and armature reaction fluxes are combined, the on-load flux distribution in a single-layer winding machine can exhibit even larger variations.
In [61], [62], the stator core flux density of an FSCW machine with interior magnets is investigated. It is claimed that the investigated machine possesses electric and magnetic symmetry that causes the yoke fluxes behind each slot to show identical patterns, although separated in time. Here, it will be shown that for a three-phase fractional-slot machine with three slots per pole, the magnetic symmetry is indeed such that the yoke flux is identical behind each slot.

Background

The magnetic flux densities in iron yokes are calculated in a variety of ways and for various reasons. The most common reasons are to determine the iron losses and to prevent iron saturation. In many cases, only the no-load flux is calculated, and the armature reaction is disregarded [63], [64]. PM machines are typically designed such that the air gap flux density induced by the armature reaction is lower than the air gap flux from the magnets. This will prevent the demagnetisation of the PMs in the case of fault currents in the stator windings. However, it does not necessarily ensure that the yoke flux densities originating from the armature reaction will remain low. In FSCW machines with significant subharmonics, the stator and rotor yoke fluxes can be much higher than the air gap flux. This can

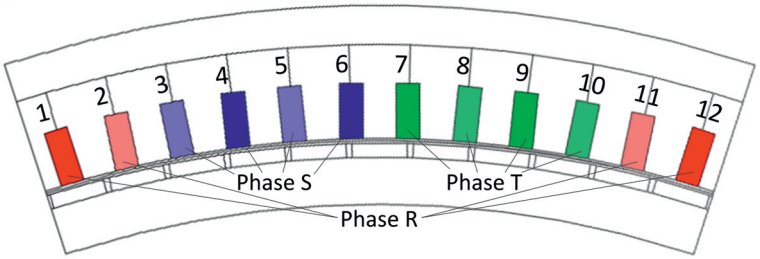

Figure 4.7: Machine A: Positions and winding layout

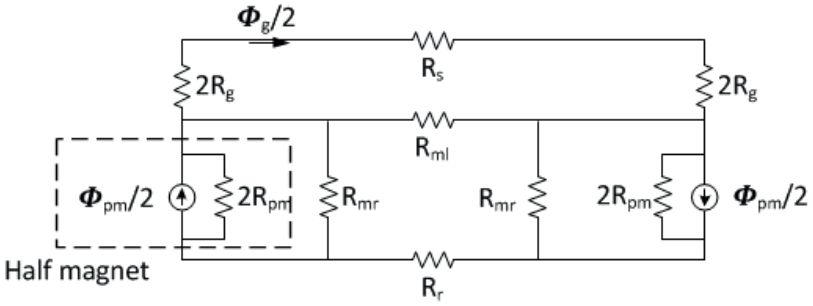

Figure 4.8: No-load magnetic circuit

cause the back iron to become heavily saturated, and in such a case, the magnetic flux can spread into nearby conductive materials, thereby inducing losses.

The most accurate method of performing such calculations is finite element analysis (FEA). In some cases, however, FEA is not practical. In this thesis, a simple method requiring only two LPMs is used to estimate the fluxes throughout all parts of the stator and rotor yokes and teeth.
The objects of study are the yoke and teeth fluxes, not the flux densities. The flux at position 1, for example, is the integral of the tangential flux density over the line connecting slot number one with the outer periphery (Figure 4.7). The mean flux density behind a slot can be found by dividing the flux at the corresponding position by the yoke thickness. To limit the scope of this work, attention is focused on the stator yoke fluxes.

4.4.2 No-load magnetic fields

The no-load magnetic fields are calculated using the LPM shown in Figure 4.8 [65]. R_s and R_r are the stator and rotor yoke reluctances, respectively. Both are set to zero because of the high relative permeability of iron. R_g is the air gap

reluctance, R_{ml} is the magnet-to-magnet leakage reluctance, R_{mr} is the magnet-to-rotor-yoke leakage reluctance, R_{pm} is the magnet reluctance, and ϕ_{pm} is the remanent flux of the permanent magnet.
The physical air gap is multiplied by a Carter coefficient, k_C, to account for the variation in the flux density in the air gap caused by slotting [66]:

$$k_C = \left[1 - \frac{1}{\frac{\tau_s}{w_{slot}} \left(5 \frac{g}{w_{slot}} + 1 \right)} \right] \tag{4.14}$$

The Carter coefficient is always greater than or equal to one.

From the magnetic circuit, one can see that the no-load air gap flux per meter is

$$\phi_{g,nl} = \frac{R_{ml} R_{pm1} \phi_{pm}}{R_g R_{ml} + 4 R_g R_{pm1} + R_{ml} R_{pm1}} \tag{4.15}$$

where R_{pm1} is the reluctance resulting from $2R_{pm}$ and R_{mr} in parallel. The no-load rotor yoke flux per meter is

$$\phi_{r,nl} = \frac{R_{pm1} \phi_{pm} (4 R_g R_{ml})}{2(R_g R_{ml} + 4 R_g R_{pm1} + R_{ml} R_{pm1})} \tag{4.16}$$

The stator yoke flux at no load is $\phi_{s,nl} = \phi_{g,nl}/2$.
The no-load flux has a certain spatial distribution, and the phase shift between slots is

$$\alpha_s = 360 \frac{p}{Q} \tag{4.17}$$

The no-load calculation is performed in time steps. The flux at position 1 is at a maximum at $t = 0$, and the fluxes at all other positions lag behind in accordance with their phase angles. The fluxes in all teeth and behind every stator slot are found at each time step. For simplicity, it is assumed that the flux is sinusoidally varying in time.

The no-load flux density amplitudes in the teeth, magnets, and rotor and stator yokes for Machines A-D are listed in Table 4.5.

Figure 4.9 shows how the no-load flux varies over time at various positions in Machine A. The positions are labelled as shown in Figure 4.7. At $t = 0$, one permanent magnet is located directly below the tooth to the left of position 1.

Table 4.5: No-load fluxes and flux densities

	Machine A	Machine B	Machine C	Machine D
$\phi_{g,nl}$ [mWb/m]	52.4	52.8	138.8	151.2
$B_{t,nl}$ [T]	1.23	1.42	1.21	1.09
$B_{m,nl}$ [T]	0.74	0.70	0.84	0.83
$B_{r,nl}$ [T]	0.51	0.62	0.94	0.96
$B_{s,nl}$ [T]	0.52	0.66	0.92	1.08

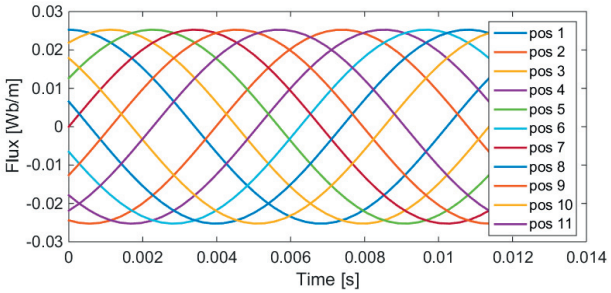

Figure 4.9: No-load flux as a function of time in Machine A

4.4.3 Armature reaction fields

The magnetic LPM shown in Figure 4.10 is used to find the magnetic flux densities in the teeth and yokes that are induced by the armature reaction. R_{gap} is the reluctance of the magnet and the air gap combined, R_{slot} is the slot leakage reluctance, N is the number of turns per coil, I is the current, and ϕ is the mesh flux. The subscript i indicates the slot number, Q is the number of slots per base winding, and t and b denote the top and bottom winding layers, respectively, in the case of two-layer windings. When the winding is of the single-layer type or for a concentrated double-layer winding, $NI_i^b = NI_i^t$.
The figure shows only a part of the mesh network. $Q*$ teeth must be included in the circuit.
In a slot that contains stator coils in which the current is distributed evenly and linearly, the stored magnetic energy is $1/3$ of the magnetic energy that would be present if the current were concentrated at one point at the bottom of the slot [67]. This should be considered when modelling the slot leakage reluctance. As a simplification, the slot leakage reluctance can be calculated using the equation

$$R_{slot} = L\frac{3w_{slot}}{\mu_0 d_{slot}} \tag{4.18}$$

where μ_0 is the permeability of vacuum.

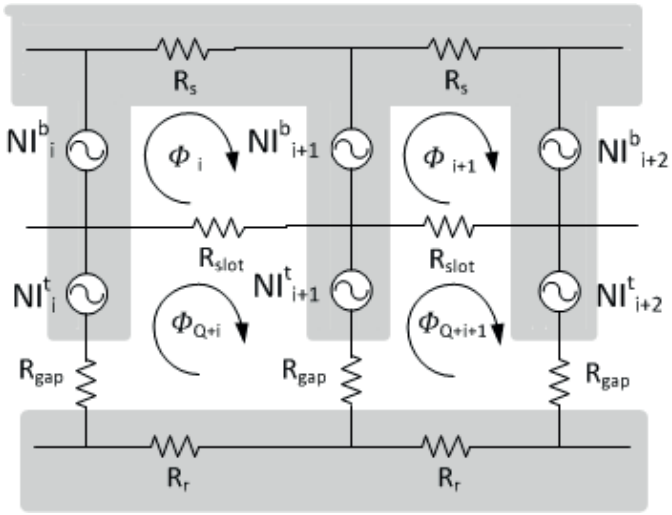

Figure 4.10: Armature reaction magnetic circuit

The LPM contains three nodes per tooth. This is a coarse division and can be refined to obtain more precise estimates of the flux densities. For machines with salient poles, more nodes should be added at the slot opening.

With the aid of Figure 4.10, one can write the following equations:

$$NI^b_{i+1} + \phi_{i+1}R_s - NI^b_{i+2} + (\phi_{i+1} - \phi_{Q*+i+1})R_{slot} = 0 \tag{4.19}$$

$$\begin{aligned}(\phi_{Q*+i+1} - \phi_{Q*+i})R_{gap} + NI^t_{i+1} + (\phi_{Q*+i+1} - \phi_{i+1})R_{slot} \\ -NI^t_{i+2} + (\phi_{Q*+i+1} - \phi_{Q*+i+2})R_{gap} + \phi_{Q*+i+1}R_r = 0\end{aligned} \tag{4.20}$$

A set of $2Q*$ equations yields a matrix equation of the form

$$\underline{NI} = R\underline{\phi} \tag{4.21}$$

where R is a $2Q*$ by $2Q*$ matrix and NI and ϕ are vectors with a length of $2Q*$. The first half of ϕ contains the fluxes per meter in the stator back yokes, and the second half contains the fluxes per meter in the rotor back yokes. The tooth fluxes at the air gap and at the tooth base are $\phi_{gap,ar} = \phi_{Q*+i+1} - \phi_{Q*+i}$ and $\phi_{i+1} - \phi_i$, respectively.

In Figure 4.12, the flux through each tooth (at the air gap) over 11 magnetic poles is illustrated for Machines A-D. The blue line shows the flux in each tooth, whereas the black line represents the main harmonic. In Machines A and B, there are 12

$$
\mathrm{R} = \left[\begin{array}{cccc|cccccc}
R_s + R_{slot} & 0 & \cdots & 0 & -R_{slot} & 0 & 0 & \cdots & 0 & 0 \\
0 & R_s + R_{slot} & \cdots & 0 & 0 & -R_{slot} & 0 & \cdots & 0 & 0 \\
\vdots & \vdots & \ddots & \vdots & \vdots & \vdots & \vdots & \ddots & \vdots & \vdots \\
0 & 0 & \cdots & R_s + R_{slot} & 0 & 0 & 0 & \cdots & 0 & -R_{slot} \\
\hline
-R_{slot} & 0 & \cdots & 0 & R_1 & -R_{gap} & 0 & \cdots & 0 & -R_{gap} \\
0 & -R_{slot} & \cdots & 0 & -R_{gap} & R_1 & -R_{gap} & \cdots & 0 & 0 \\
\vdots & \vdots & \ddots & \vdots & \vdots & \vdots & \vdots & \ddots & \vdots & \vdots \\
0 & 0 & \cdots & -R_{slot} & -R_{gap} & 0 & 0 & \cdots & -R_{gap} & R_1
\end{array}\right]
$$

Figure 4.11: R matrix

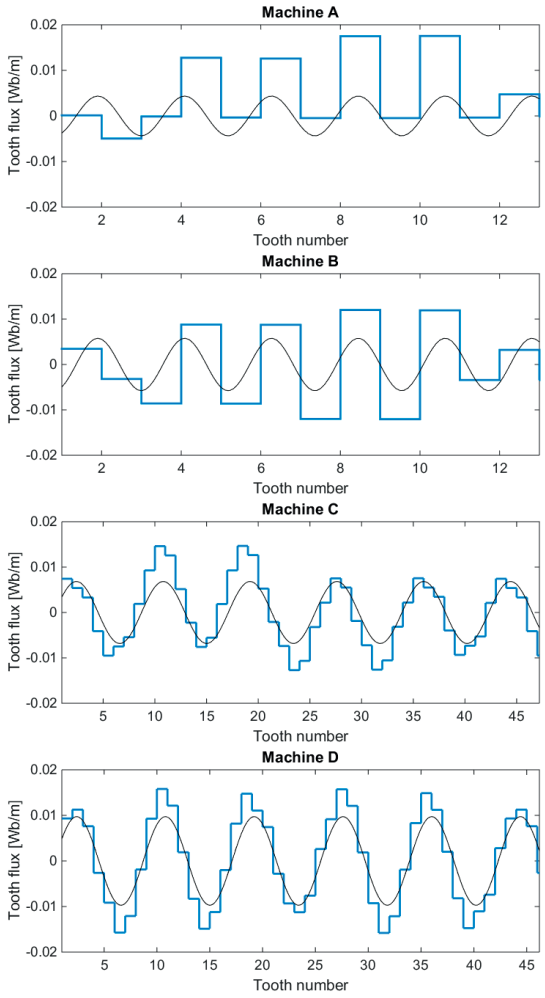

Figure 4.12: Tooth fluxes in Machines A-D,
where the black curves represent the main harmonics

teeth for each 11 poles, whereas in Machines C and D, there are 46.2 teeth for each 11 poles. The fluxes are shown for a single instant of time.

The armature reaction flux calculation is also performed in time steps, and the fluxes at all positions are found in all time steps. The phase currents are

$$\begin{aligned} I_R &= \widehat{I}cos(\omega(t-t_0)) \\ I_S &= \widehat{I}cos(\omega(t-t_0)+2\pi/3) \\ I_T &= \widehat{I}cos(\omega(t-t_0)-2\pi/3) \end{aligned} \tag{4.22}$$

The current is placed in the q-axis to ensure the maximum torque production per unit current. Hence, the current must be in phase with the no-load voltage. The no-load flux is summed for all slots composing phase R as a function of time. The no-load voltage is $E_R = -d\phi_{nl}/dt$. t_0 is set equal to the time at which the induced R-phase voltage peaks. This places the current in the q-axis.

A stationary calculation performed at $t = t_0$ yields the tangential fluxes in the stator and rotor back yokes as well as the radial fluxes in the teeth, as shown in Table 4.6. It is clear that both the stator yoke and rotor yoke fluxes are significantly higher than the tooth fluxes. This is in contrast to the case of no-load operation for FSCW machines, in which the fluxes in the stator and rotor yokes are each half of the flux in the teeth because half of the tooth flux goes to the left and the other half goes to the right.

It is generally known that in an FSCW machine, the air gap flux can contain high subharmonics [63], [68]. A Fourier analysis of the flux distributions presented in Table 4.6 for both the air gap fluxes and the stator yoke fluxes reveals that although the amplitudes of the air gap flux subharmonics are high, the amplitudes of the stator yoke flux subharmonics are even higher. The lowest harmonic (5^{th}) is 7 times higher than the main harmonic (55^{th}), as shown in Figure 4.13. This is the main reason why it is important to account for the armature reaction when calculating magnetic flux densities for fractional-slot machines.

Above, the spatial distribution of the armature reaction flux is investigated. The armature reaction flux in the stator yoke is also studied as a function of time. The no-load flux amplitude is equal at every position, as illustrated in Figure 4.15, which shows the no-load fluxes at positions 3-6. The field rotates over time, and the maximum flux appears to move from one position to the next. By contrast, the armature reaction flux amplitudes are not equal at all positions. The time variations of the fluxes at positions 3, 4, 5 and 6 in Machine A are shown in Figure 4.14.

Table 4.6: Armature reaction fluxes [mWb/m]

Position	Stator flux	Rotor flux	Air gap flux
1	2.6	-0.2	0.5
2	-20.2	17.8	-18.1
3	-16.2	17.4	0.4
4	-27.5	26.4	-8.9
5	-24.9	26.1	0.2
6	-36.5	35.3	-9.2
7	-36.5	35.3	0
8	-24.9	26.1	9.2
9	-27.5	26.4	-0.2
10	-16.2	17.4	8.9
11	-20.2	17.8	-0.4
12	2.6	-0.2	18.1

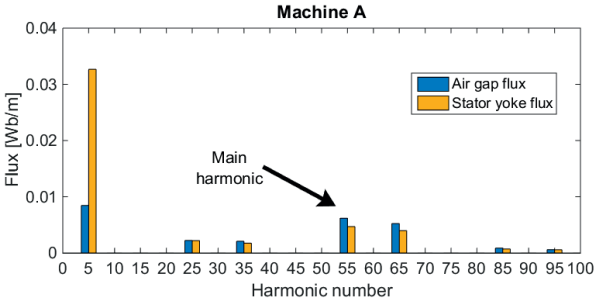

Figure 4.13: Harmonic contents of the stator yoke and air gap fluxes

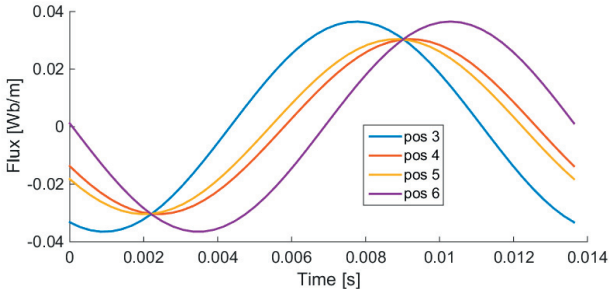

Figure 4.14: Armature reaction fluxes at positions 3-6 in Machine A

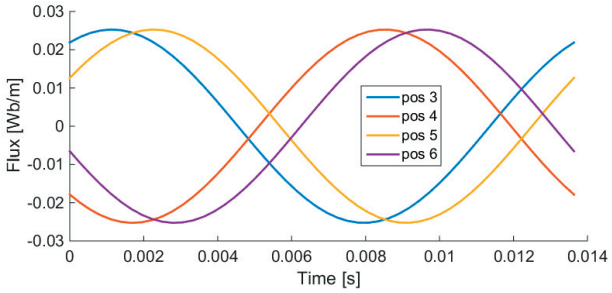

Figure 4.15: No-load fluxes at positions 3-6 in Machine A

The pattern of the four curves repeats itself for each of the three phase groups. Although the armature reaction creates a flux pattern that rotates, this pattern is not evenly distributed along the stator. In Machine A, the winding layout causes the flux to be higher on the outer edges of the phase group than in the middle of the phase group. This is illustrated by the dark circles in Figure 4.16.

Similar uneven patterns can also be observed in the other three machines. Figure 4.17 shows the amplitudes of the armature reaction fluxes at each position in Machines A-D. The flux patterns of Machines B and C show that some parts of the stator yoke are dramatically less used by the armature reaction flux than other parts.

When three phases are distributed symmetrically within each section, the flux pattern is repeated three times per section. This can be seen in Figure 4.17. In a fractional-slot machine with only three slots per pole ($q = 0.5$), there are only three slots in one symmetric section; hence, the flux amplitude is the same behind all slots, as is claimed in [69].

The highest flux densities due to the armature reaction alone that are found in the

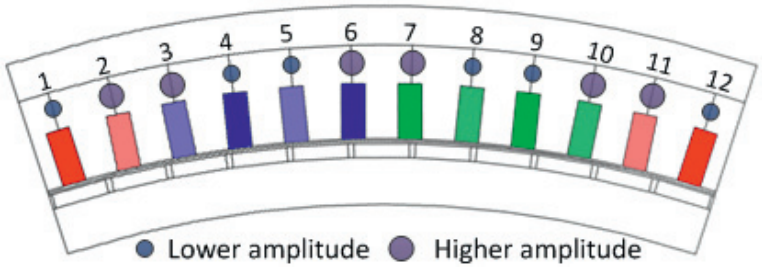

Figure 4.16: Armature reaction flux pattern in Machine A

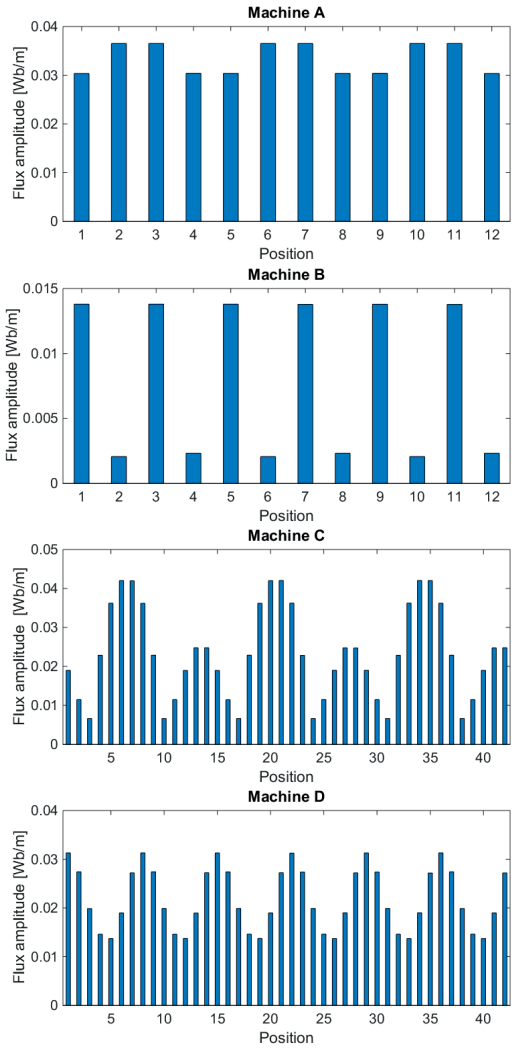

Figure 4.17: Armature reaction flux amplitudes in Machines A-D

Table 4.7: Armature reaction flux densities

	Machine A	Machine B	Machine C	Machine D
$B_{t,ar}$ [T]	0.43	0.33	0.55	0.48
$B_{r,ar}$ [T]	0.59	0.24	0.54	0.36
$B_{s,ar}$	0.73	0.35	0.56	0.45

teeth, the rotor yokes and the stator yokes are listed for all machines in Table 4.7.

4.4.4 Magnetic fields under load: combining the no-load and armature reaction fields

FEA model

FEA can be used to verify the analytical results for a machine and to generate illustrations of the flux lines. FEA models of the four machines considered in this study have been created in COMSOL. One 10^{th} of Machines A and B and one 8^{th} of Machine D are modelled, and antisymmetry conditions are imposed on the side boundaries. Because of the winding layout of Machine C, one quarter of this machine is modelled, with symmetry conditions imposed on the side boundaries. The laminations have a nonlinear magnetisation curve.

First, a no-load calculation is performed under rotation, yielding the fluxes through the cross sections of the stator back yokes as functions of time. The flux density and flux lines of Machine A are presented in Figure 4.18. The flux lines flow tangentially along the stator yoke in every other direction as the position of interest moves along the stator.

Second, an armature reaction calculation is performed with the current placed in the q-axis and the PMs de-energised. The resulting flux density and flux lines of Machine A are shown in Figure 4.19. The 5^{th} harmonic can be clearly seen.

Finally, superposition is assumed, and the time-varying flux from the no-load simulation is added to the time-varying flux from the armature reaction simulation at each time step. Thus, the no-load flux, the armature reaction flux and the on-load flux can be found from only two time-stepped FEA simulations.
This approach is based on the assumption that superposing the two results is sufficient to predict the on-load flux. This assumption is verified by the results of a simulation of Machine D under load, with magnetised magnets **and** the armature reaction. The on-load fluxes and the superposed fluxes at positions 3 and 15 are

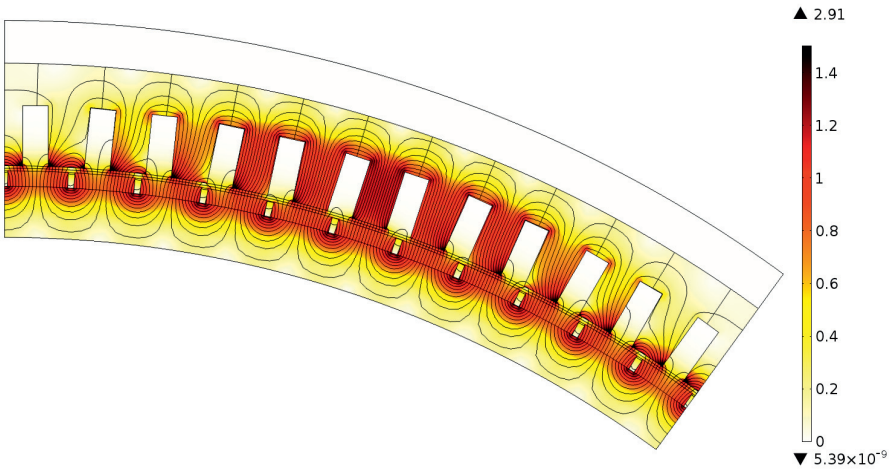

Figure 4.18: No-load flux density [T] and flux lines in Machine A

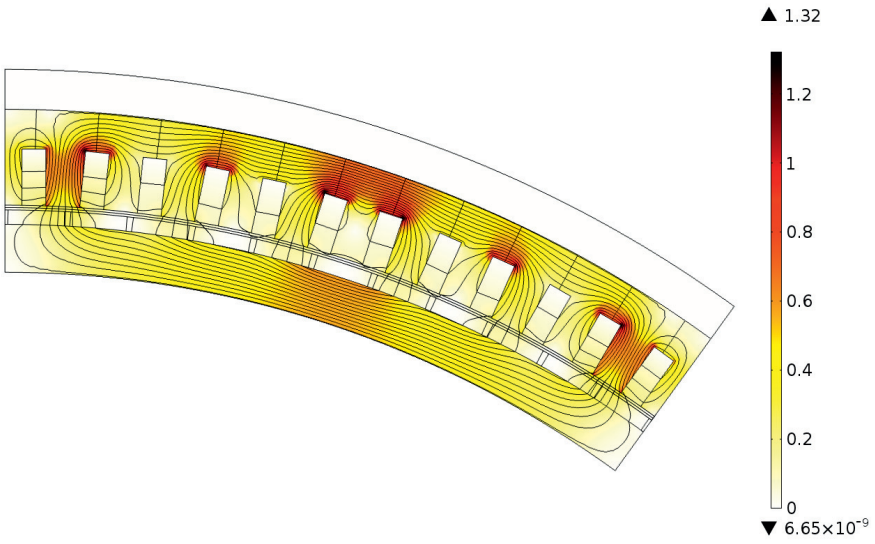

Figure 4.19: Armature-reaction-induced flux density [T] in Machine A

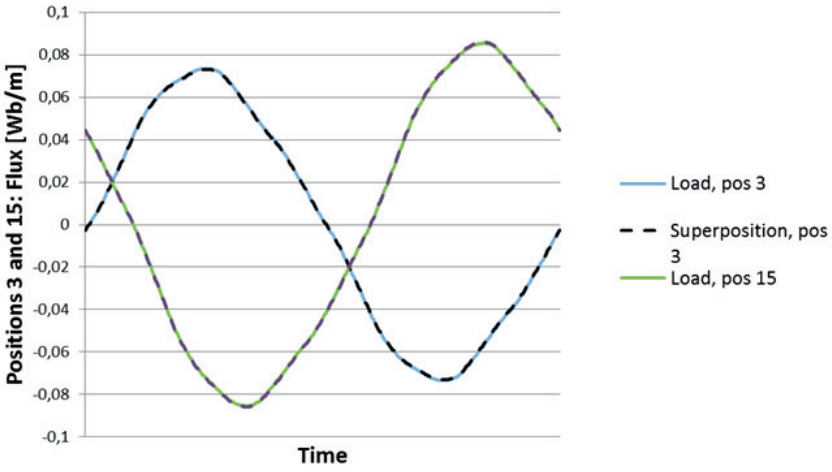

Figure 4.20: Fluxes obtained via superposition compared with fluxes obtained under load

plotted in Figure 4.20 to show that the assumption is valid. For a heavily saturated machine, however, this simplification would be less accurate.

Flux under load: combining the no-load and armature reaction fluxes

The results from the no-load LPM and the armature reaction LPM are also combined at each time step, as in the case of the FEA results described above. When the two flux patterns shown in Figures 4.15 and 4.14 are combined, the no-load flux lines are alternately summed with or subtracted from the 5^{th} harmonic of the armature reaction flux at every other position. This is illustrated in Figure 4.21, which shows how the armature reaction and no-load fluxes are combined to obtain the superposed fluxes at positions 3 and 4. At position 3, the armature reaction flux and the no-load flux are nearly opposite in phase, whereas at position 4, they are nearly in phase.

Consequently, the magnitude of the flux under load is more strongly dependent on the phase difference between the no-load and armature reaction fluxes than on the amplitude of the armature reaction flux. Although the highest armature reaction flux amplitude is observed at position 3, the combined flux amplitude is much higher at position 4.

Figure 4.22 shows the amplitudes of the no-load and armature reaction fluxes and the resulting on-load fluxes at all positions in Machine A. It is evident that the no-load and armature reaction fluxes are alternately in phase and opposite in phase at every other position. This is the effect of the very high subharmonic content of the

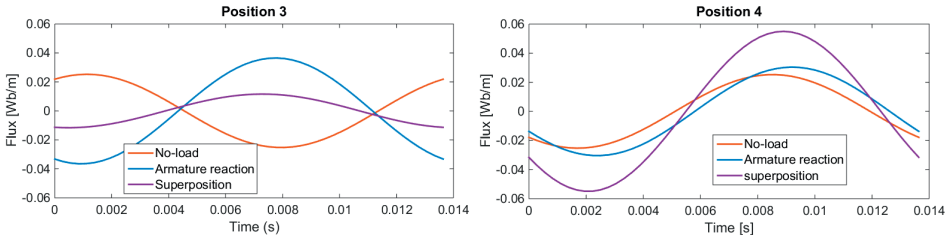

Figure 4.21: No-load, armature reaction and superposed fluxes as functions of time

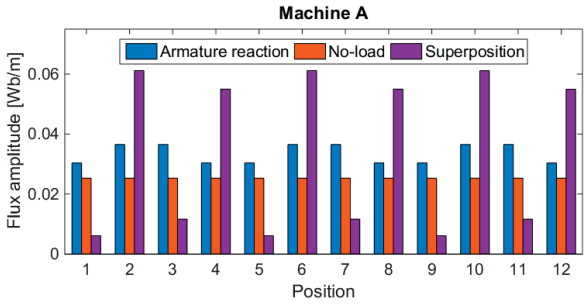

Figure 4.22: Flux amplitudes at positions 1-12 in Machine A

armature reaction flux. It is clear that the flux density is not evenly distributed in the back yoke, even over time. The highest flux amplitudes, at positions 2, 6 and 10, are 10 times higher than the flux amplitudes at positions 1, 5 and 9.

The winding configuration creates an **armature reaction flux** that does not exhibit the same amplitudes behind all slots. Additionally, the time-varying armature reaction flux exhibits a phase shift with respect to the no-load flux that is **not the same** behind each slot. Consequently, the on-load flux amplitudes differ significantly at different positions.

A **single-layer** FSCW such as that in Machine A produces a large amount of subharmonics. By comparison, the subharmonic content of a **double-layer** FSCW with the same number of poles and slots (Machine B) is significantly lower [63]. Figure 4.23 shows the harmonic contents in the air gap and the stator back yoke in Machine B. There is no strong subharmonic in the armature reaction field, and the sum of the two flux patterns looks quite different from the single-layer pattern; see Figure 4.24.

In Machine B, the armature reaction pattern is more variable than that in Machine A, with the highest amplitudes being 6.7 times higher than the lowest. This is the

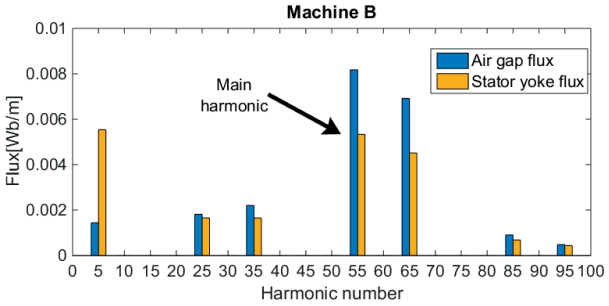

Figure 4.23: Harmonic content in Machine B

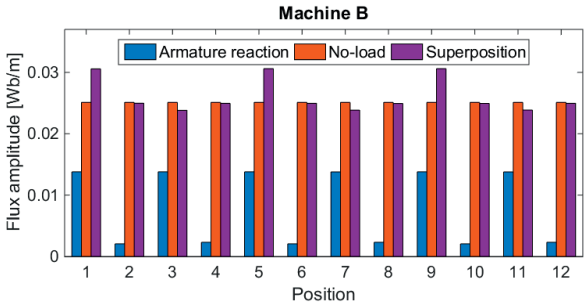

Figure 4.24: Flux amplitudes at positions 1-12 in Machine B

phenomenon described in [60]; in a machine with double-layer winding and two adjacent teeth wound with the same phase, the armature reaction is smaller in certain parts of the stator. However, when the armature reaction flux is combined with the no-load flux, the difference between the lowest and highest amplitudes is only 28%. Note that the current loading of Machine B is lower than the current loading of Machine A; hence, the armature reaction has a less significant effect on the total field.

Machine C is a single-layer DW machine with 1.4 slots per pole and phase. The amplitudes of the no-load, armature reaction and superposed fluxes are shown in Figure 4.25. It is evident that the flux variation in this machine is also large. The armature reaction flux amplitudes at positions 6 and 7 are more than 6 times higher than the armature reaction flux amplitudes at positions 3 and 10. The variation among the load flux amplitudes is smaller but still significant. The highest amplitude (position 5) is more than two times higher than the lowest amplitude (position 8).

Machine D is a double-layer DW machine with the same numbers of slots and poles as Machine C. Figure 4.26 shows the amplitudes of the fluxes in the stator

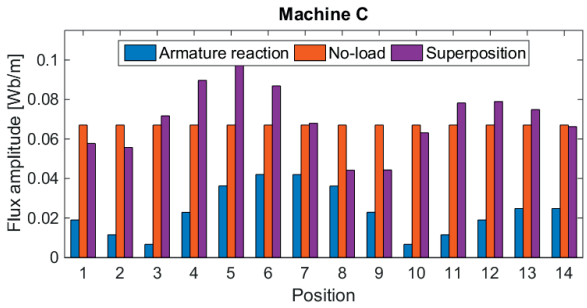

Figure 4.25: Flux amplitudes at positions 1-14 in Machine C

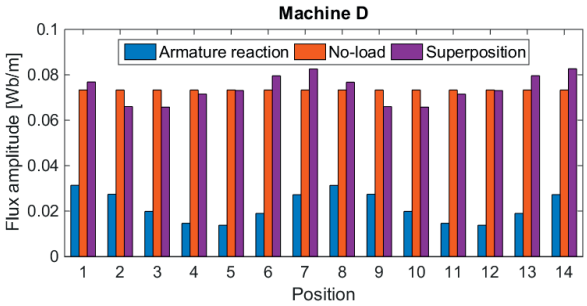

Figure 4.26: Flux amplitudes at positions 1-14 in Machine D

yoke. The armature reaction flux amplitudes vary with position, and the amplitude at position 1 is 2.3 times higher than that at position 4. As the figure shows, the no-load fluxes dominate the stator flux pattern; hence, the variation in the load flux amplitudes is only 40% in Machine D.

Discussion

The validity of the combined LPM method can be confirmed by comparing the results with the results of FEA simulations. In Table 4.8, the no-load, armature reaction and superposed fluxes in all four machines are summarised. The top half of the table lists the highest amplitudes observed in the machines, whereas the bottom half lists the average amplitudes. The results from both the FEA simulations and the LPM calculations are included.

The LPM method underestimates the flux by 1.3 to 11.3% in most cases. The no-load fluxes for Machines A and B are slightly overestimated, and the maximum and average armature reaction fluxes in Machine B are lower than the FEA results by 13.1 and 23.6%, respectively. It is possible that the armature reaction flux calculations could be further improved by improving the slot leakage model, especially

Table 4.8: Maximum and average flux amplitudes [mWb/m] from the analytical and FEA calculations

Machine		A	B	C	D
Maximum					
No load	LPM	26.2	26.4	69.4	75.6
	FEA	24.7	24.9	70.6	76.7
Armature reac.	LPM	36.5	13.8	42.0	31.3
	FEA	38.4	15.9	43.4	34.6
Superposition	LPM	62.2	30.6	96.9	83.3
	FEA	62.4	31.5	103.5	90.9
Average					
No load	LPM	26.2	26.4	69.4	75.6
	FEA	24.4	24.7	70.6	76.7
Armature reac.	LPM	33.4	8.0	23.3	21.8
	FEA	34.4	10.5	24.3	24.6
Superposition	LPM	33.7	26.5	69.8	74.4
	FEA	36.5	26.4	74.5	80.8

for double-layer winding machines.

The results presented in Table 4.8 show that the maximum stator flux is considerably higher than the no-load flux. The difference ranges from 19% (in Machine D) to 152% (in Machine A).
The average fluxes in Machines B-D under load are only slightly higher than the average no-load fluxes; by contrast, the average on-load flux is 50% higher in Machine A. This is because of the strong subharmonic content in Machine A.

To further illustrate the validity of the LPM model, Figure 4.27 shows the amplitudes under load at all positions as calculated using the LPM and FEA approaches. The analytical model is able to recreate the flux patterns in all machines.

In integer slot machines, no subharmonic flux patterns exist in the yokes, and the current reaction fluxes are no larger in the yokes than in the air gap. If the air gap flux is kept relatively low to avoid demagnetisation, then the current reaction does not have a strong impact on the yoke flux magnitude. However, in fractional-slot machines, the combination of the no-load flux and the current reaction flux can lead to yoke fluxes that are much higher than the no-load fluxes. The yoke thickness must be adjusted accordingly if saturation is to be avoided.

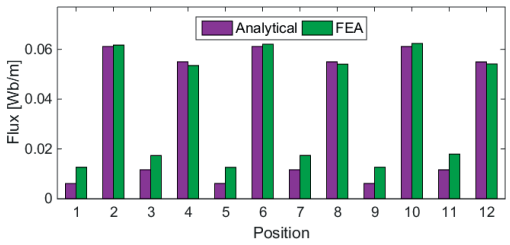

(a) Machine A

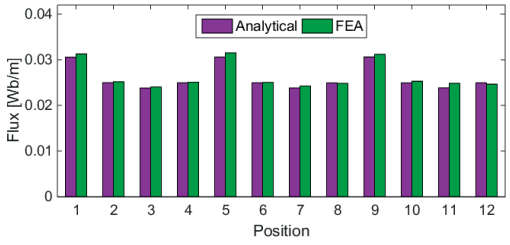

(b) Machine B

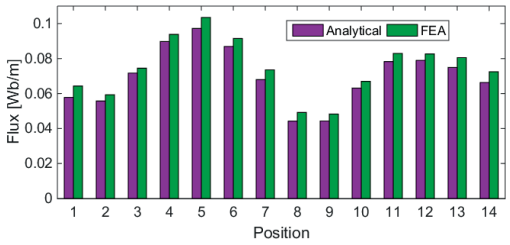

(c) Machine C

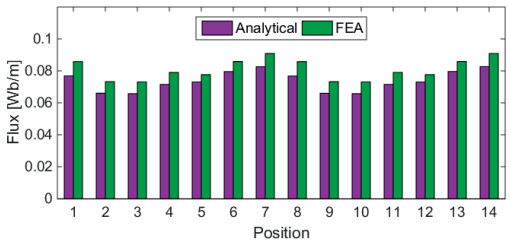

(d) Machine D

Figure 4.27: Superposed amplitudes in Machines A-D

Table 4.9: Maximum flux densities under load

	Machine A	Machine B	Machine C	Machine D
$B_{t,sum}$ [T]	1.49	1.58	1.78	1.57
$B_{r,sum}$ [T]	1.09	0.68	1.30	1.06
$B_{s,sum}$ [T]	1.24	0.76	1.29	1.19

It is possible to allow the stator yoke to partially saturate in small sections. This would increase the reluctance in the yoke and act as a flux barrier, reducing the subharmonic fluxes in both the stator and rotor yokes. This is a known method of reducing the induced losses in the rotors of fractional-slot winding machines [70], [71]. Additional flux barriers can also be placed in the locations where the fluxes are highest. However, these measures reduce the torque production capability.

The maximum flux densities in the teeth, the rotor yoke and the stator yoke for all four machines are listed in Table 4.9. The maximum stator yoke flux density under load is higher than that without load; the differences are 10%, 15%, 40% and 138% in Machines D, B, C and A, respectively. The tooth flux density is also higher under load conditions than under no-load conditions. In Machines A and B, the differences are 21% and 11%, respectively, whereas in Machines C and D, the difference is approximately 45%. The tooth flux values have not been verified against FEA calculations.

4.4.5 Conclusion of Chapter 4.4

The armature reaction flux in the stator and rotor yokes should be accounted for in a fractional-slot machine, especially when the current loading is high. Although the subharmonic contents of the magnetic flux in the air gap can be high, the subharmonic amplitudes in the yokes may be much higher. Consequently, in the stator yoke, the on-load flux can be much higher than the no-load flux.
The flux amplitudes in the stator yoke are not the same behind every slot of the stator. The winding layout may cause the armature reaction flux amplitudes to be unevenly distributed. An even larger variation can be observed when the permanent magnet flux and the armature reaction flux are combined, as the phase shift between them varies behind different slots. In one of the investigated machines, the load flux behind one slot is 10 times higher than that behind another slot.
With detailed knowledge of how the magnetic flux is distributed along the stator back yoke, the machine designer can place the holes for bolts or cooling in positions that are less saturated. It is also possible to deliberately allow the yoke to

saturate in some areas, thereby creating flux barriers and reducing the magnitude of the subharmonic fluxes traversing the machine, potentially reducing the rotor losses. Flux barriers designed to reduce the subharmonic fluxes can also be placed in precisely chosen locations when the flux pattern in the stator is known.

4.5 Electrical circuit

4.5.1 Slot current

The torque density of an electrical machine is greatly affected by the slot fill factor. For a generator designed for medium-voltage operation (3.3 kV), the insulation thickness is considerable, and together with the slot wedge, it can constitute a large portion of the slot if the slot dimensions are relatively small. A slot may be modelled with one or two coil sides, depending on the number of winding layers. Each coil side has a fill factor, k_{fill}, and is surrounded by a layer of insulation. There is a slot wedge at the slot opening. Table 4.10 lists the values of the slot parameters, which are fixed in the optimisation routine but can be altered if needed. Figure 4.28 illustrates how the windings are located in the slot in the cases of double-layer windings of the DW (left) and FSCW (right) types. The total winding depth and width are

$$d_{winding} = d_{slot} - d_{wedge} - 2N_{rad}d_{ins} \tag{4.23}$$

$$w_{winding} = w_{slot} - 2N_{tan}d_{ins} \tag{4.24}$$

For a double-layer FSCW, N_{tan} is 2; otherwise, it is 1. For a double-layer DW, N_{rad} is 2; otherwise, it is 1.

The resulting slot fill factor, k_{slot}, is given by

$$k_{slot} = \frac{k_{fill}d_{winding}w_{winding}}{d_{slot}w_{slot}}. \tag{4.25}$$

Table 4.10: Slot parameters

Parameter		Value
Slot wedge thickness	d_{wedge}	1.5 mm
Slot insulation thickness	d_{ins}	2.15 mm
Winding fill factor	k_{fill}	0.7
AC/DC factor	$R_{ac,dc}$	1.2

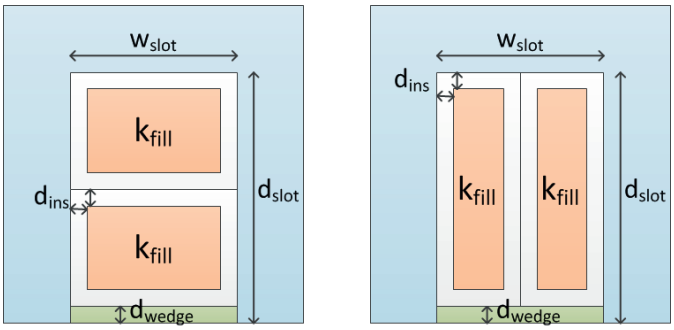

Figure 4.28: Schematic views of a slot

The phase current is

$$I_{ph} = \frac{J d_{slot} w_{slot} k_{slot}}{N_{lay} N} n_{pb} \tag{4.26}$$

where N is the number of turns per coil and n_{pb} is the number of parallel branches. The phase currents and fill factors of the investigated machines are listed in Table 4.12 in a later section.

4.5.2 Inductances

The synchronous inductance, L_s, of a winding consists of a magnetising inductance, L_m, and a stator leakage inductance, L_σ:

$$L_s = L_m + L_\sigma \tag{4.27}$$

The magnetising inductance links the rotor and stator fluxes, whereas the leakage inductance is linked to the stray flux and is not useful for energy conversion. A large synchronous inductance results in a low power factor, which leads to a higher power converter cost and higher copper losses. However, a large synchronous inductance can also be beneficial; it is a desired property in machines designed for field-weakening operation. It also reduces short-circuit currents and reduces the risk of demagnetisation. The leakage inductance is calculated as follows [53]:

$$L_\sigma = L_{ew} + L_{slot} + L_{tt} + L_\delta + L_{sq} \tag{4.28}$$

Here, L_{ew} is the end winding leakage inductance, L_{slot} is the slot leakage inductance, L_{tt} is the tooth tip leakage inductance, L_δ is the air gap leakage inductance, and L_{sq} is the skew inductance. FSCWs often have a high synchronous air gap leakage inductance because of the high harmonic content of the MMF. DWs often have a higher magnetising inductance because of the mutual coupling between phases and a higher end winding inductance because of their longer end windings.

The magnetising inductance of a single-phase winding, L_{mph}, is found using the following equation [53]:

$$L_{mph} = \frac{2}{\pi}\mu_0\mu_{pm}\frac{1}{2p}\frac{4}{\pi}\frac{\tau_p}{l_m + \mu_{pm}g}L(k_w N n_{cs})^2 \tag{4.29}$$

This equation is applicable for both concentrated and distributed winding designs. L is the active length, μ_{pm} is the relative permeability of the PM, τ_p is the pole pitch, N is the number of turns per coil, and n_{cs} is the number of coils in series. In a machine with overlapping coils, all phase currents contribute to the magnetic flux linkage, and the total magnetising inductance is $L_m = L_{mph}N_{ph}/2$. Concentrated coils have a very low mutual inductance, and the total magnetising inductance becomes $L_m = L_{mph}$.

An integer winding machine with skewing has a magnetising inductance that is slightly lower than (4.29). If L_m is the magnetising inductance of an unskewed machine and L'_m is the magnetising inductance of a skewed machine, then the skew inductance is

$$L_{sq} = L_m - L'_m = (1 - k_{sq}^2)L_m \tag{4.30}$$

The air gap harmonic leakage flux is the flux crossing the air gap that has a different harmonic number than the main harmonic. Especially in fractional-slot machines, the subharmonic flux patterns can result in large air gap leakage fluxes. For a given combination of poles and slots, the ratio between L_m and the air gap leakage inductance, L_δ, remains the same: $L_\delta = L_m \cdot \sigma_\delta$. It is the winding factor of the different harmonic numbers, k_{wv}, that affects the air gap harmonic leakage factor [72]:

$$\sigma_\delta = \sum_{\substack{v=1 \\ v\neq p}}^{v=+\infty}\left(p \cdot \frac{k_{wv}}{v \cdot k_{w1}}\right)^2 \tag{4.31}$$

The winding factors are found using the star of slots method.

The slot is assumed to have parallel sides, an even distribution of turns within the slot, and a slot wedge in the opening. The total slot leakage inductance of a phase winding is [53]

$$L_{slot} = \mu_0 L(N n_{cs})^2 \lambda_s \frac{4N_{ph}}{Q} \tag{4.32}$$

where

$$\lambda_s = k_1\frac{d_{slot} - d_{wedge}}{3w_{slot}} + k_2\frac{d_{wedge}}{w_s lot} \tag{4.33}$$

Table 4.11: Permeance factors of end windings

	λ_{lew}	λ_{ew}
Concentrated	0.518	0.138
Distributed	0.493	0.074

In single-layer windings, in which a single slot is occupied by windings of only a single phase, $k_1 = k_2 = 1$. For double-layer windings, the flux contributions in a single slot may come from two different phases, in which case k_1 and k_2 become less than one:

$$k_1 = \frac{5+3G}{8} \quad k_2 = \frac{1+G}{2} \tag{4.34}$$

The parameter G represents the mutual influence of the upper and lower currents. If the phase shift between the currents in these two layers is γ, then G is the average value of $cos\gamma$.

A fraction of the flux entering the air gap from the stator teeth never crosses the air gap but instead returns through the adjacent tooth. This leakage flux is called the tooth tip leakage flux, and it can be significant in a machine with a relatively large air gap [53]:

$$L_{tt} = \mu_0 L (N n_{cs})^2 \lambda_t \frac{4N_{ph}}{Q} \tag{4.35}$$

$$\lambda_t = k_2 \frac{5(\frac{g+l_m/\mu_{pm}}{w_{slot}})}{5 + 4(\frac{g+l_m/\mu_{pm}}{w_{slot}})} \tag{4.36}$$

The end winding leakage inductance [53] is given by

$$L_w = \mu_0 q (N n_{cs})^2 l_w \lambda_w \frac{4N_{ph}}{Q} \tag{4.37}$$

$$l_w \lambda_w = 2 l_{ew} \lambda_{lew} + W_{ew} \lambda_{ew} \tag{4.38}$$

where l_{ew} and W_{ew} are the (axial) length and (tangential) width, respectively, of the end winding. The axial end winding length is estimated to be considerably larger in distributed windings than in concentrated windings. The tangential width is equal to the coil span length, which is typically longer in DWs than in FSCWs. The permeance factors for the two different winding configurations [53], [68] are listed in Table 4.11.

The total phase reactance, X, depends on the electrical frequency in radians, ω:

$$X = \omega \left(L_m + L_\delta + L_{slot} + L_{tt} + L_w + L_{sq} \right) \tag{4.39}$$

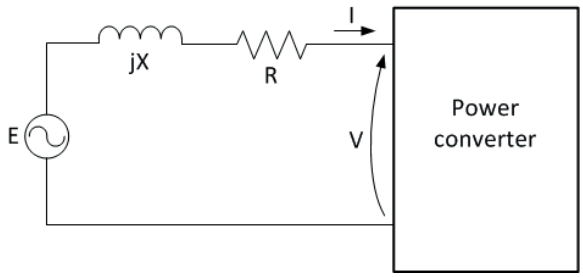

Figure 4.29: Per-phase equivalent electrical circuit

The phase reactances of Machines A-D are listed in Table 4.12.

4.5.3 Power factor

Figure 4.29 shows the per-phase equivalent electrical circuit for the generator. R is an equivalent resistance that includes the copper loss, P_{cu}; the iron loss, P_{iron}; and the magnet loss, P_{pm}:

$$R = \frac{P_{cu} + P_{pm} + P_{iron}}{3I_{ph}^2} \tag{4.40}$$

The resistance of the winding alone is

$$R_{cu} = R_{ac/dc}\frac{l_{winding}}{\sigma_{cu}A_c n_{pb}} \tag{4.41}$$

where $l_{winding}$ is the total length of the phase winding, σ_{cu} is the conductivity of copper at the operating temperature, A_c is the conductor cross section, and n_{pb} is the number of parallel branches, which is set equal to the number of base windings. The value of the AC/DC factor, $R_{ac,dc}$, is fixed to 1.2 in this analysis, as the winding details are outside the scope of this work. It is assumed that it is possible to wind the coils with wires that are sufficiently small to keep the AC losses at this level, using Litz wire, for example.

The no-load phase voltage is

$$E = \omega\frac{\phi_{g,nl}}{\sqrt{2}}Lk_w N n_{cs} \tag{4.42}$$

where $\phi_{g,nl}$ is the air gap flux under no-load conditions. The voltage quality of the machine is not investigated here. Consequently, the optimisation procedure will not differentiate between machines with low and high voltage total harmonic distortion (THD).

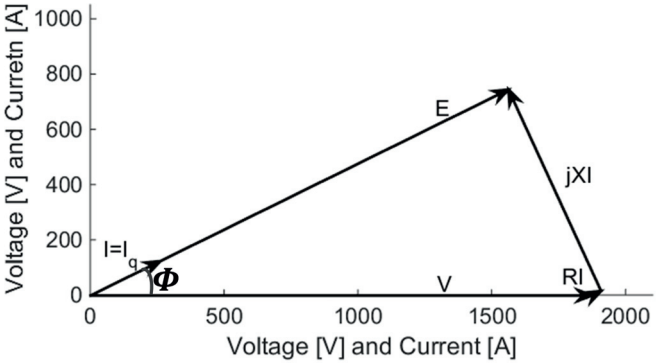

Figure 4.30: Phasor diagram

Table 4.12: Electrical circuit values

	Machine A	Machine B	Machine C	Machine D
Apparent power [MVAr]	1.75	1.59	1.56	1.57
Phase current [A]	304	282	276	278
No-load voltage [kV]	1.65	1.77	1.81	1.80
Phase reactance [pu]	0.32	0.22	0.20	0.22
Phase resistance[pu]	0.011	0.013	0.015	0.019
Power factor	0.84	0.92	0.94	0.93
Fill factor	0.55	0.50	0.52	0.49

The current is placed in the q-axis. This results in the highest produced torque per unit current in the machine. Figure 4.30 presents the phasor diagram in generator mode. From this figure, one can find the power factor, $cos(\phi)$. The induced voltages and power factors for Machines A-D are listed in Table 4.12.

4.6 Torque

The active machine length is obtained by calculating the produced torque using the following equation [73], [74]:

$$T = \frac{3}{2} p \phi_{g,nl} \frac{Q}{6} k_w \widehat{I}_s L \tag{4.43}$$

where $\widehat{I}_s$ is the amplitude of the slot current and k_w is the winding factor. L is the active length of the machine and can be found by letting T be the torque required to harness 1.5 MW of power at the rated speed.
The active lengths and air gap diameters of Machines A-D are listed in Table 4.13.

Table 4.13: Main dimensions

	Machine A	Machine B	Machine C	Machine D
L	0.441 m	0.367 m	0.537 m	0.416 m
Air gap diameter	2.762 m	2.940 m	2.796 m	3.102 m

No mechanical structures are included in the model, with the exception of the outer housing wall, the thickness of which is set to 5 cm regardless of the diameter and length. The cost of this housing is included in the objective function. One mechanical constraint is included in the model, namely, the maximum shear stress on the rotor shaft. The shaft stress is to be kept below 30 MPa. For a smooth cylinder, the relation between the shaft stress and the torque is described by the following equation:

$$\tau = T\frac{r}{J_T} \tag{4.44}$$

where T is the torque, τ is the shear stress, r is the shaft radius, and

$$J_T = \pi r^4/2 \tag{4.45}$$

is the torsion constant for a circular cross section.

The torque ripple is not calculated in this analysis. Fractional-slot machines with large air gaps often have low cogging torques. For a fractional-slot machine, a very detailed magnetic analysis of the forces is needed to calculate the torque ripple and cogging torque. Consequently, the optimisation procedure will not differentiate between designs with low and high torque ripples. However, machines with integer slots typically exhibit very high torque ripples. Therefore, in the case of integer-slot machines, the rotor is skewed by one slot pitch to avoid high cogging torques. This affects the winding factor, the leakage inductance and the cost of the rotor.

4.7 Loss analysis

4.7.1 Copper and iron losses

Copper loss, denoted by P_{cu}, occurs in both the active section and the end windings. The eddy-current and skin effects are undesired frequency-dependent effects that increase the copper loss. The magnitudes of the skin and eddy-current effects are not calculated. In the active region, the resistance is multiplied by an AC/DC factor of 1.2, whereas in the end winding region, the AC/DC factor is 1.
The conductivity of copper is highly dependent on temperature, and the conduct-

Table 4.14: Iron and copper losses

	Machine A	Machine B	Machine C	Machine D
Copper loss	18.5 kW	24.9 kW	30.1 kW	44.0 kW
Iron loss	12.8 kW	9.5 kW	6.5 kW	6.7 kW
Iron loss, no load	10.6 kW	9.2 kW	5.2 kW	5.3 kW

ivity at the winding temperature is obtained using a thermal model:

$$\sigma_{cu} = 58 \cdot 10^6 \frac{234.5 + 20}{234.5 + T_{cu}} \tag{4.46}$$

where T_{cu} is the copper temperature. An iteration in which the copper loss is updated according to the copper temperature ensures an error in the winding temperature of less than one degree.
The iron losses that develop in the stator laminations are estimated using the Steinmetz equation, which combines the hysteresis loss, p_h, with the eddy-current loss, p_e:

$$P_{iron} = p_h + p_e = k_h B^\beta \omega + k_e B^2 \omega^2 \tag{4.47}$$

k_h, k_e and β are hysteresis and eddy-current coefficients, where $k_h = 50$, $k_e = 0.06$ and $\beta = 1.9$ [75]. This expression is valid for a sinusoidal flux density. In analytical calculations, the no-load field is typically used to predict the iron losses [63]. However, this approach can result in underestimation of the iron losses. Here, B is the average flux density amplitude in the teeth or the stator yoke and is the result of combining the no-load and armature reaction fluxes as described in Chapter 4.4.4. The iron loss is divided into tooth loss and yoke loss, as the teeth and the yokes experience different flux densities. The iron losses computed using the flux densities obtained for both load and no-load conditions are listed in Table 4.14, together with the copper losses.

Frictional losses are not included in the model. It is assumed that these will be of approximately the same magnitude regardless of the geometric dimensions. Consequently, the calculated efficiency will be slightly higher than the actual efficiency of the generator.

4.7.2 Permanent magnet losses

Introduction

Rare-earth magnet materials have revolutionised the design of electrical machines, enabling machines with high torque densities and high efficiencies. However, the

conductivity of the permanent magnet material is high, causing variations in the flux density in the magnets to induce currents and losses that result in high magnet temperatures. The losses induced in the permanent magnets contribute to magnet heating and possible demagnetisation [76]. These flux density variations originate from three sources: MMF harmonics rotating at speeds other than the synchronous speed, reluctance variations caused by stator slotting, and time harmonics in the stator currents. It is assumed here that the generator will operate in synchronous mode and that only the fundamental time harmonic is present, thereby eliminating losses induced by current harmonics.

The induced currents are complex and are not easily predicted using analytical equations. FEA yields the most precise estimations, but it is time-consuming and impractical for optimisation purposes. Various methods have been developed to analytically predict the eddy-current losses in the magnets for both no-load [77]–[80] and armature reaction [78], [79], [81]–[85] operation.

Few studies have evaluated and compared the various methods of calculating eddy-current losses in magnets. One exception is a paper by Alexandrove et al. [86] that compares two methods of calculating MMF-induced eddy currents and one for calculating no-load eddy currents using FEA results. Published research that compares analytical results with FEA results is mainly focused on small machines with few poles and slots. The exception is [81]; however, the electrical insulation between the magnetic poles is not considered.

In this thesis, several methods, some of them modified, for the calculation of the no-load eddy currents in the magnets are compared with 2D FEA simulations for two large machines with large magnets and many slots and poles. For the MMF-induced eddy-current losses in the magnets, two of the same methods, along with a third, are compared with the FEA results for the same machines. Different levels of magnet laminations are also investigated. Several remarks regarding the validity of the methods are offered, and weaknesses of the models are identified.
Although the analytical and FEA results do not show a very good match, some of the investigated methods are selected for calculating the no-load and MMF-induced eddy-current losses in the machine analysis. These calculations provide an approximation of the PM losses.

Eddy-current magnet loss models for no-load operation

No-load eddy-current losses are induced by reluctance variations in the stator. These reluctance variations cause the magnetic fields in the magnets to fluctu-

ate, thereby inducing voltages and, consequently, resistive losses. Wider slots and larger slot pitches result in higher no-load losses.

In [77], the no-load eddy-current losses in the rotor magnets are determined using conformal mapping, which requires software for calculating the *modulation function* created by the slotting. The segmentation of the magnets is not included in the model. This method is also used in [86], and the discrepancy between the analytically and FEA-computed losses is large. This method is discussed here under the names Method 1 and Method 1a.
Carter's theory for predicting the magnetic field variation due to slotting is used in [79]. Two different analyses are used, one for bulky magnets that are wider than the harmonic wavelengths of the flux variations and one for laminated magnets. The no-load loss calculation is discussed here under the name Method 2.

Method 1: Markovic and Perriard
Marcovic and Perriard present a fairly simple method of determining the eddy-current losses in permanent magnets due to slotting in [77]. The flux density variations caused by slotting are found via a *conformal mapping*. This is a complex function that transforms the magnet and air gap region into another configuration in which the magnetic field can be calculated analytically. In the special case in which the the slot opening is small compared to the slot pitch, it is possible to use a closed-form equation to find the magnetic field.
It is assumed that only the slot opening affects the flux density variations; therefore, the slots are treated as infinitely deep. It is also assumed that the eddy currents are resistance-limited, which means that the field they generate is too weak to influence the external field. It is stated that the condition for the weak diffusion effect is that the skin effect must be "sufficiently" higher than the PM dimensions.
First, the magnetic field in the *slotless* case is determined.

$$B_m = \frac{l_m}{l_m + \mu_{PM} g} B_R \tag{4.48}$$

B_R is the remanent flux density of the PMs. In [87], the conformal mapping is replaced with a closed-form equation, presented in [57], to find the relative permeance due to slotting. The Fourier series coefficient for harmonic number k of the modulation function is

$$K_k = \Lambda \frac{4}{\pi k} \sin\left(1.6\pi k \frac{w_{slot}}{\tau_s}\right) \left[0.5 + \frac{\left(k\frac{w_{slot}}{\tau_s}\right)^2}{0.7815 - 2\left(k\frac{w_{slot}}{\tau_s}\right)^2}\right] \tag{4.49}$$

Table 4.15: No-load PM losses, Method 1

	Machine A	Machine B	Machine C	Machine D
Method 1	254 kW	233 kW	399 kW	314 kW
Method 1a	223 kW	188 kW	351 kW	278 kW

where τ_s is the slot pitch and

$$\Lambda = \frac{1}{2}\left[1 - \left(1 + \left(\frac{w_{slot}}{2g'}\right)^2 + (1+v^2)\right)^{-0.5}\right] \tag{4.50}$$

Here, v is determined using equation 20 in [57] at a position midway between the stator bore and the rotor yoke. (In [87], Λ has been simplified.) The total loss in the magnets due to reluctance variations becomes

$$P_{pm,1} = \frac{1}{2} V_{pm} B_m^2 (R_s\Omega)^2 \sigma_{pm} \sum_k K_k^2 \left[1 - \left(\frac{\tau_s}{\pi k w_m} \sin\frac{\pi k w_m}{\tau_s}\right)^2\right] \tag{4.51}$$

V_{pm} is the total PM volume, Ω is the mechanical speed in rad/s, and $\sigma_{pm} = 0.694 \cdot 10^6$ Siemens/m is the conductivity of the PM material. Only the five lowest harmonics are included.

Method 1a

Method 1 is criticised for its inaccurate calculation of the flux densities [86]. Fang et al. emphasise that a Carter factor should be included to account for the reduced mean flux density in a machine with a large ratio of the slot opening to the air gap length. In Method 1a, a Carter coefficient is included in the expression for B_0:

$$B_m = \frac{l_m}{l_m + \mu_{PM} g k_C} B_R \tag{4.52}$$

The total loss is found using equation 4.51.

Method 2: Pyrhönen et al.

Method 1 is suitable only for magnets that are not laminated. The method presented by Pyrhönen et al. [79], henceforth called Method 2, can be used to calculate the harmonic losses under both load and no-load conditions and for both bulky magnets and laminated magnets.

The calculation of the flux density variations in the magnets due to stator slotting

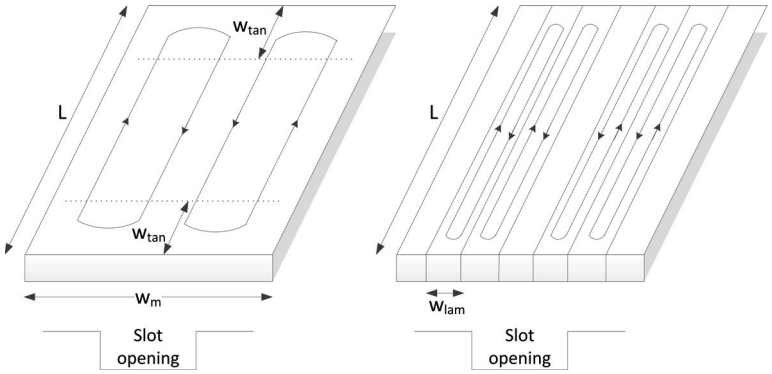

Figure 4.31: Eddy-current paths in wide magnets (left) and laminated magnets (right)

is based on Carter's theory [88]. Figure 4.31 illustrates how eddy currents form paths in wide, bulky magnets (left) and in laminated magnets (right).

The variations in the air gap flux density on the rotor surface, according to Carter, are described by

$$\beta = \frac{B_0}{B_{max}} = \frac{1 + u^2 - 2u}{2(1 + u^2)} \tag{4.53}$$

$$u = \frac{w_{slot}}{2g} + \sqrt{1 + \left(\frac{w_{slot}}{2g}\right)^2} \tag{4.54}$$

Figure 4.32 illustrates the variation in the flux density over one slot pitch. δ is the air gap length, denoted by g in this thesis, and b_1 is the slot width. The amplitude of the flux variation harmonic k, according to [79], is

$$\hat{B}_k = B_{av}\beta k_C \frac{2\sin\left(k\pi\frac{b_1'}{\tau_s}\right)}{k\pi\left[1 - \left(k\frac{b_1'}{\tau_s}\right)^2\right]} \tag{4.55}$$

The average flux density in the magnets, B_{av}, is equal to the magnet no-load flux density found in Chapter 4.4.2, $B_{m,nl}$. The parameter b_1' can be found in [79]. τ_s is the slot pitch. The pole pitch for each harmonic is $\tau_k = \tau_s/(2k)$.

In magnet segments that are wider than the slot pitch, the width of the eddy-current loop is determined by the wavelength of the magnet flux harmonic. The width of the magnet segment does not affect the no-load losses per magnet volume.

It is assumed that the current density is not constant throughout the thickness of the magnet. The current density for a given harmonic decreases with increasing depth

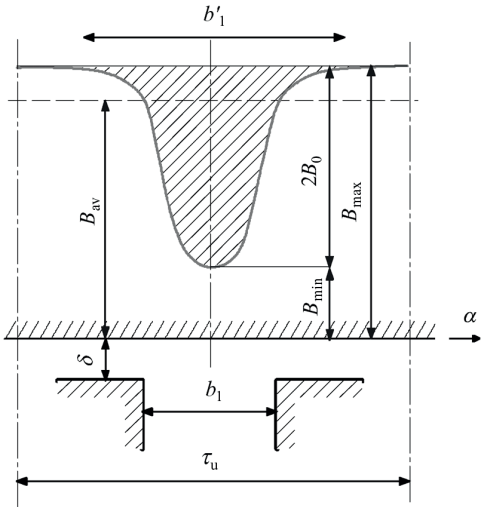

Figure 4.32: Distribution of the air gap flux density over a distance of one slot pitch, τ_s ©[2012] [79]

at a rate that depends on the skin depth for the corresponding harmonic frequency.

The resistances of the eddy-current loops formed by the various harmonics are found. It is noted that *if the magnet piece is longer than the penetration depth*, then the skin depth can be used as the end area to approximately calculate the eddy-current path resistance. However, in slowly rotating or very short machines, the penetration depth can even be greater than the machine length. In such a case, the cross-sectional surface of the tangential path in a machine with a skin depth that is larger than the magnet thickness is set to

$$S_{PM,tan,k} = w_{tan} \times h \approx \frac{L}{2} \times \frac{\delta_{PM,k}}{2} \left(1 - e^{-2l_m/\delta_{PM,k}}\right) \tag{4.56}$$

and the length of the axial path is set to $2 \cdot L/2$.

Method 2a

Here, an alternative calculation is proposed. It will be referred to as Method 2a. Regardless of the skin depth, the width of the tangential path is assumed to be no greater than its length, and the cross-sectional surface becomes

$$S_{PM,tan,k} = w_{tan} \times h \approx \tau_k \times \frac{\delta_{PM,k}}{2} \left(1 - e^{-2l_m/\delta_{PM,k}}\right) \tag{4.57}$$

The length of the axial path becomes $2(L - \tau_k)$. If the harmonic pole pitch is larger than $L/2$, then the expression given in (4.56) is used.

The eddy-current loss under one harmonic pole pitch due to harmonic k is

$$P_{pm,ec,k} = E_{PM,k} I_{PM,k} cos(\pi/4) \tag{4.58}$$

$E_{PM,k}$ is the induced voltage of one eddy-current loop due to harmonic k, and $I_{PM,k}$ is the rms eddy current in the loop. The total eddy-current loss in a machine with $2p$ magnets is

$$P_{pm,2} = 2p \frac{w_m}{\tau_k} \sum_k P_{pm,ec,k} \tag{4.59}$$

Method 2b

The eddy-current losses can be reduced by laminating the magnets in N_{lam} pieces and placing electrical insulation between the laminations. This increases the eddy-current resistance and reduces losses.

To consider such laminations, another modified version of Method 2 is presented in [79]. In a case in which $\tau_k/n < w_{lam} < \tau_k$, where $n \in (3, 4, 5...)$, the flux, resistance and cross-sectional surfaces are modified. It is now assumed that the eddy-current loop width is determined by the lamination width, not the pole pitch of the harmonic. Additionally, although this is not mentioned in [79], equation 4.59 must be modified as follows:

$$P_{pm,2b} = 2pN_{lam} \sum_k P_{pm,ec,k} \tag{4.60}$$

Method 3

Pyrhönen et al. provide a second equation for the case in which the lamination width is significantly narrower than the harmonic pole pitch ($w_m/N_{lam} << \tau_k$). This equation is also used to calculate the eddy-current losses in lamination sheets [53]. The eddy-current loss in the total magnet volume V_{PM} due to no-load flux density harmonic k, $\hat{B_k}$, is

$$P_{pm,3,k} = \frac{1}{6} V_{PM} \pi^2 f_{PM,k}^2 w_{lam}^3 \hat{B_k}^2 \sigma_{PM} \tag{4.61}$$

$w_{lam} = w_m/N_{lam}$ is the lamination width, and

$$f_{PM,k} = \frac{n}{60} kQ \tag{4.62}$$

is the frequency of harmonic k. n is the rotational speed (rpm), and Q is the number of slots. This equation holds only for flux density harmonics with a pole pitch wider than the lamination width. The loss is proportional to the square of the speed and the cube of the lamination width.

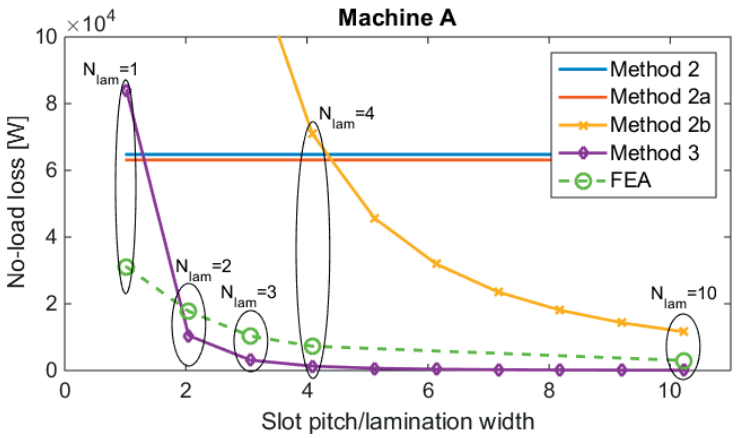

Figure 4.33: No-load losses in Machine A computed using various methods

Calculated no-load magnet losses

To evaluate the presented methods, 2D COMSOL models have been created in which the no-load losses are calculated with various degrees of segmentation for Machines A-D. The models neglect all end effects. Constraints are imposed on the currents flowing through each magnet, ensuring zero net current in each segment at each time step. All calculations are performed for a rated speed of 80 rpm, with the magnets energised and the stator currents set to zero.

Methods 2 and 2a are intended to be used only for magnet segments that are wide compared to the slot pitch. The lamination width is not a parameter in the loss computation. In Machine A, the magnet width is approximately equal to the slot pitch. The first harmonic of the reluctance variation is $\tau_1 = 0.51 w_m$. When the magnets are laminated, the lamination width is smaller than the pole pitch of the first harmonic. It is therefore expected that the no-load losses in Machine A should be lower than the resulting losses computed using Methods 2 and 2a. Method 2b is relevant for harmonic pole pitches that are comparable to the lamination width. Method 3 is valid only for harmonics that are much larger than the lamination width. When the magnets in Machine A are laminated 10 times, $\tau_1 = 5.1 w_{lam}$.

Figure 4.33 shows how the no-load loss of Machine A varies with the lamination rate. Each lamination rate corresponds to a lamination width that is smaller than the slot pitch. The results are compared with FEA results. Methods 2 and 2a indicate losses that are considerably higher than the FEA results. Method 2b overestimates the no-load losses; however, the results approach the FEA results as the lamination rate increases. Method 3 overestimates the no-load losses when there is only one segment per pole, and the loss reduction gained through lamination is

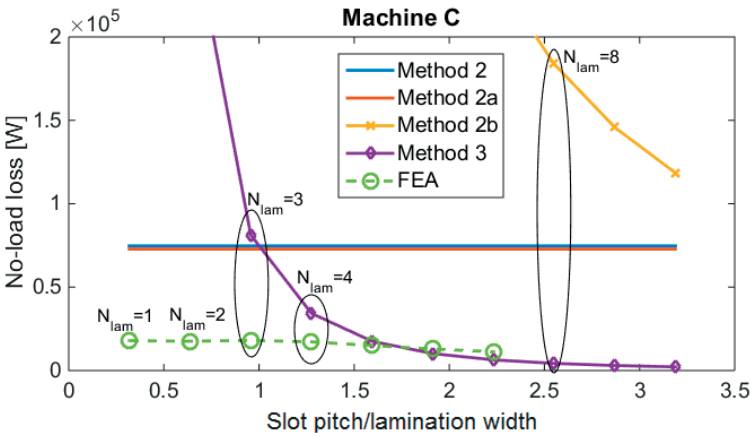

Figure 4.34: No-load losses in Machine C computed using various methods

greatly overestimated.
Methods 1 and 1a calculate very high no-load losses. For unsegmented magnets, the loss predictions of these methods are 366 kW and 321 kW, respectively.

The magnets in Machine C are considerably wider than the slot pitch; hence, Methods 2 and 2a are appropriate to use when the number of segments is low. For a high number of segments, other methods must be used. Figure 4.34 illustrates the no-load losses in Machine C computed using Methods 2, 2a, 2b and 3, in addition to the FEA results. Methods 2 and 2a greatly overestimate the no-load losses in Machine C. Method 2b is expected to overestimate the losses for a low degree of segmentation and to approach the correct value when N_{lam} is high. However, the curve produced using Method 2b does not show good agreement with the FEA results even when the number of segments is high. As expected, Method 3 overestimates the no-load losses when N_{lam} is low. When the number of laminations is 5, 6 or 7, the calculated no-load losses agree fairly well with the FEA results. The no-load PM losses for Machine C calculated using Methods 1 and 1a are 575 kW and 505 kW, respectively.

A challenge related to the analytical calculation of eddy-current losses is the sensitivity of such calculations to certain key parameters. The variations in the flux density are the driving force giving rise to the eddy currents. In the analytical methods shown in Figures 4.33 and 4.34, the ratio of the variation in the magnetic flux density is described by the parameter β. If the calculated value of β is inaccurate, it has an enormous effect on the loss estimation. A sensitivity analysis

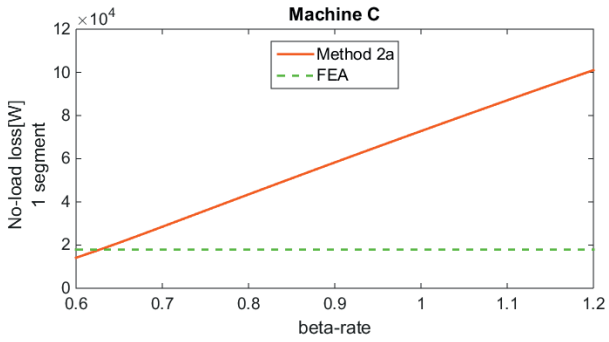

Figure 4.35: No-load loss as a function of β

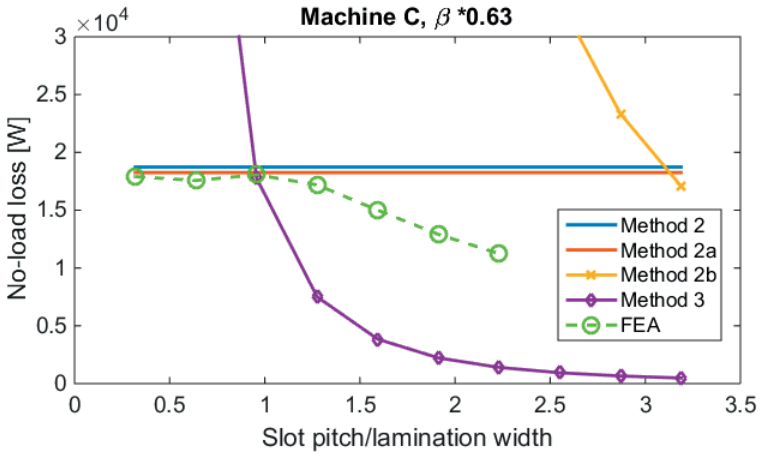

Figure 4.36: No-load losses in Machine C with β multiplied by 0.63

performed for the parameter β is presented in Figure 4.35. This figure shows how a change in β affects the total eddy-current loss (calculated using Method 2a). An inaccurate calculation of β significantly affects the calculated no-load loss. Figure 4.36 shows the calculated no-load losses calculated when the value of β is reduced to 63%.

The results given above show that the eddy-current magnet losses under no-load operation cannot be easily predicted using the investigated methods. More accurate methods are needed to correctly estimate these losses. Next, the eddy-current losses caused by MMF harmonics are presented.

Eddy-current losses in the PMs induced by the armature

A variety of methods have been developed for predicting the eddy-current losses caused by stator MMF harmonics, not considering the air gap permeance variation due to slotting. In [81], the PMs are modelled as a single layer of magnetic material, with no insulation between magnet poles. This assumption leads to computed losses that are much higher than those in a machine with physically separated magnets or segmented magnets.
The segmentation of magnets is considered in [82] and [83]. The models presented by Atallah et al. in [83] and by Polinder et al. in [82] are compared for a case study in [86]. It is found that the losses computed using Atallah's method are well consistent with the FEA results. The Polinder method is found to give somewhat lower losses, especially when the magnet segments are small. Ishak et al. further develop Atallah's method in [84] to obtain the PM losses produced by different time harmonics. The Carter coefficient is introduced in [87] to account for the larger effective air gaps in machines with large slot openings.
In other methods, such as [58], [78], [85], differential equations are used to solve the magnet field and rotor loss problem, in which the eddy-current reaction field is considered. These methods are very complex and not very practical.

Method 4: Ishak et al.
The methods used in [84] and [87] to predict the MMF-induced eddy-current losses in PMs are collectively referred to as Method 4 in this thesis. These are extensions of the model presented in [83] by Atallah et al. No-load losses are not considered. It is assumed that induced losses arise only in the magnets and that the current is resistance-limited, i.e., that the skin depth is greater than the PM dimensions. The low rotational speed of the generator and the lack of high-order current harmonics ensure a large skin depth. The effect of eddy currents on the applied magnetic field is neglected. An infinite length is assumed, which means that end effects are also neglected.

The details of Method 4 are presented in Appendix A.

Methods 2b and 3: Pyrhönen et al.
Methods 2, 2a, 2b and 3 can also be applied to magnetic flux density variations due to MMF harmonics. [79] provides an equation for the flux density harmonics originating from the armature reaction. However, the air gap fluxes from the armature that have already been found in Chapter 4.4.3 can be used for flux density variation estimations. A Fourier analysis of $B_{gap} = \phi_{gap,ar}/\tau_s$ yields the flux density amplitude at harmonic number n, $\widehat{B}_n$. $\phi_{gap,ar}$ is an array containing the

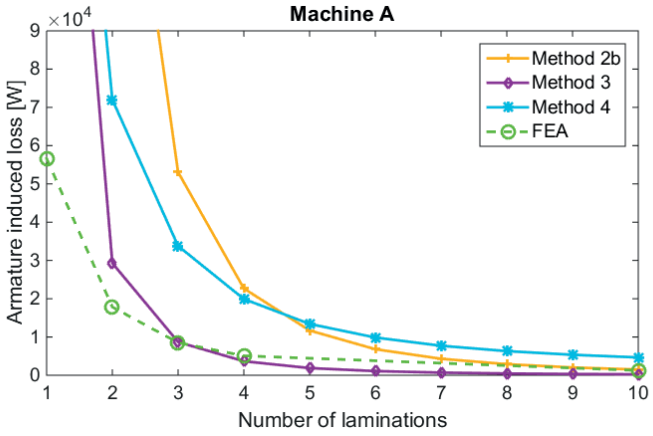

Figure 4.37: Armature-induced magnet loss in Machine A

fluxes in $Q*$ consecutive teeth at one instant in time. The flux density harmonic interacts with the rotor at a frequency of

$$f_{pm,n} = (p \pm np_s)\Omega \tag{4.63}$$

When $n = 3N_{ph} + m$, the $\pm$ in $f_{pm,n}$ is taken to be $-$; when $n = N_{ph}k - m$, it is taken to be $+$.
$n = 1$ represents the lowest harmonic produced by the stator windings. k is an arbitrary integer number, and m is either -1 or 1, depending on the winding layout. If the lowest harmonic, with p_s pole pairs, rotates in the same direction as the main harmonic, with p pole pairs, then $m = 1$. If the rotation is opposite, $m = -1$. Equation 45 in [63] is used to find the rotational directions.
The lowest harmonics are responsible for the gross part of the armature-induced magnet loss [89]. The number of harmonics included in the loss calculation is limited here to the number of pole pairs in one base winding + 5. These harmonics have a wide pole pitch, often covering several magnet poles. Therefore, Methods 2b and 3 are most appropriate for calculating the armature-induced magnet loss.

Calculated armature-induced loss

Figures 4.37 and 4.38 show how the loss decreases with an increasing lamination rate for Machines A and C, respectively. The losses calculated using Methods 2b, 3 and 4 are compared with the results of FEA simulations performed with de-energised magnets and the rated current in the stator windings.
Similar to the analytical no-load calculations, the analytical on-load calculations overestimate the losses when the magnets are not laminated, and they overestimate the loss reduction caused by the lamination.

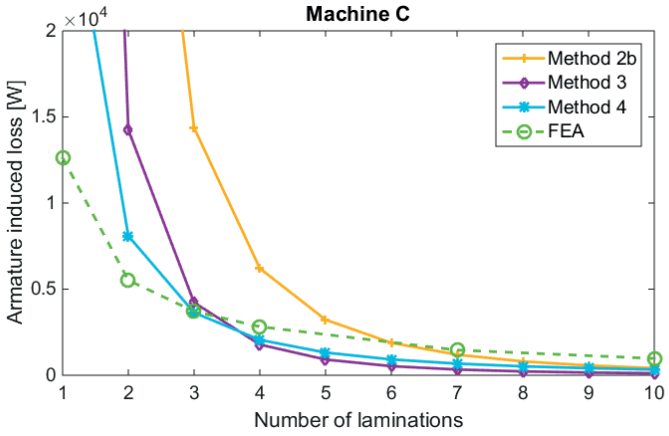

Figure 4.38: Armature-induced magnet loss in Machine C

The reason for the overestimation of the loss at low rates of lamination may be that the effect of eddy currents on the applied magnetic field is neglected. When the amplitude of the eddy currents becomes large, they will have a damping effect on the flux density variations, thereby reducing the total losses.

It can be concluded that analytical models that do not account for the effect of eddy currents on the magnetic field are not necessarily suitable for machines with large magnets. An FEA investigation of the flux densities in Machine A when induced losses are present and not present shows that the maximum flux in the machine decreases from 1.49 T when induced losses are not present to 1.14 T when induced losses are present. The magnets are not segmented. This proves that the flux density distribution in the machine is significantly affected by the eddy currents.

The analytically calculated losses are lower than the FEA simulation results when the magnets are highly segmented. The reason for this may be that the leakage flux is not included in the models and purely radial magnet fields are assumed. When the magnet segmentation is low, the current is mainly flowing into the magnet on one side and out of the magnet on the other side; see Figure 4.39. When the magnet segmentation is high, this current path is blocked, but there are still currents flowing into the magnets at the top and out of the magnet at the bottom or vice versa. This is shown in Figure 4.40. These eddy currents are neglected in the analytical equations presented here, which may be a cause of the discrepancy between the FEA results and the analytical calculations.

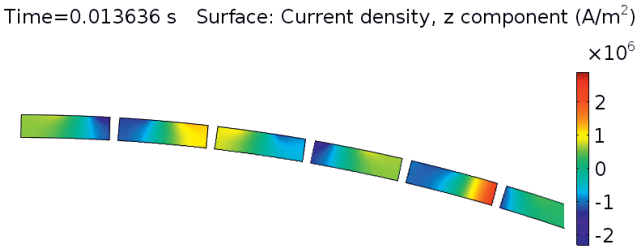

Figure 4.39: Induced currents in unsegmented magnets in Machine A

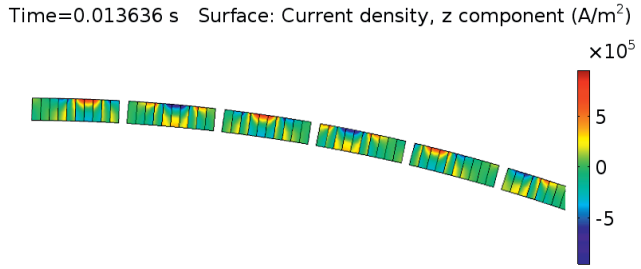

Figure 4.40: Induced currents in segmented magnets in Machine A

Selected methods

As the results presented above show, the analytical calculation of eddy-current loss is a difficult task. The physical phenomena are complex, and many assumptions must be made that do not hold for all machines. For more accurate results, more advanced analytical models, such as those presented in [78], [85], or FEA must be used.

In the analysis presented in this thesis, one of the analytical models presented above will be employed. Although not very precise, they are able to estimate the losses to the correct order of magnitude. Machine designs that result in high magnet temperatures will include magnet laminations, and machine designs that have excessively high magnet temperatures despite many laminations will be discarded by the optimisation routine. The method used to select the number of laminations is explained below.

The methods presented by Pyrhönen et al. are selected for calculating both the no-load and armature-induced losses.

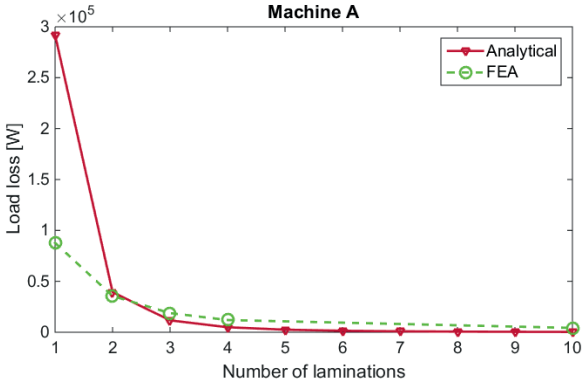

Figure 4.41: Eddy-current load loss in Machine A

Methods 2 and 2a are combined. The width of the tangential path, w_{tan}, is set to the minimum of the following parameters: $L/2$, τ_k and $\delta_{PM,k}$. The length of the axial path is set to the maximum of $L/2$ and $L - w_{tan}$.

Both Method 2 and Method 3 are applied. $P_{pm,2,k}$ and $P_{pm,3,k}$ are calculated for each harmonic, and the total no-load magnet loss becomes

$$P_{pm,nl} = \sum_k \min(P_{pm,2,k}\ P_{pm,3,k}) \tag{4.64}$$

The same procedure is used for the loss induced by the armature, $P_{pm,ar}$.
The analytically calculated eddy-current loss under load is the sum of the no-load and armature-induced losses.

The total PM loss in Machine A as a function of the segmentation rate is presented in Figure 4.41. The largest discrepancy between the analytical and FEA calculations *in terms of watts* is found when the magnets are not laminated. The load loss is overestimated by 204 kW. In a machine with such high rotor losses, the magnets will be laminated. The largest discrepancy *in terms of percentage* is found when each magnet is segmented into 10 pieces. The loss obtained using the analytical equations is only 7% of the loss found in the FEA calculation.
The corresponding results for Machine C are presented in Figure 4.42. At a low level of segmentation, the discrepancy is large. For unsegmented magnets, the analytical results are 5.4 times higher than the FEA results. When $N_{lam} = 10$, the analytical result is 25% of the FEA result.

The different MMF harmonics cause magnet losses of different magnitudes. Tables

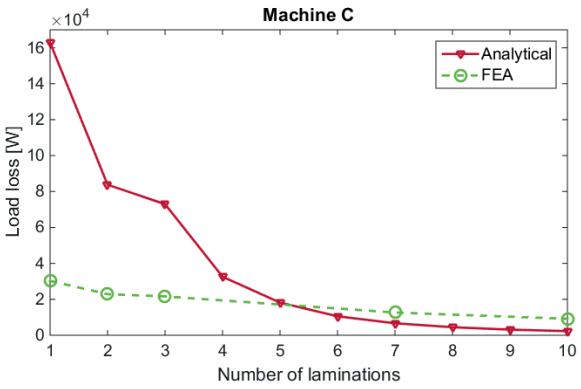

Figure 4.42: Eddy-current load loss in Machine C

Table 4.16: Armature-induced eddy-current losses in all magnets [kW/m]

Space harmonic, n	Machine A $N_{lam} = 1$	$N_{lam} = 2$	$N_{lam} = 3$	$N_{lam} = 4$
1	195.7	24.5	7.3	3.1
5	3.4	0.4	0.1	0.1
7	26.6	3.3	1.0	0.4
11	0	0	0	0
13	299.1	37.4	11.1	4.7
Total	524.9	65.6	19.4	8.2

4.16 and 4.17 list the armature-induced eddy-current losses per meter caused by the different MMF harmonics in Machines A and C. In Machine A, the first and 13$^{\text{th}}$ harmonics induce the highest magnet losses, whereas in Machine C, the first and 4$^{\text{th}}$ harmonics are the main sources of eddy-current loss.

Segmentation

The analysis includes a method that ensures that in machines with high magnet losses, the magnets are laminated. N_{lam} is not a variable in the optimisation routine; rather, its value is chosen in an inner loop. The greatest threat to the electrical machine that is posed by the induced magnet losses is over-heating of the magnet materials, which can reduce both the magnet remanence and lifetime and increase the risk of demagnetisation. The magnets are segmented into as many pieces as are required to limit the magnet temperature to below 90 °C.
A flowchart of the segmentation procedure is presented in Figure 4.43. First, the temperatures are calculated with zero magnet loss. If, when the magnet loss is

Table 4.17: Armature-induced eddy-current losses in all magnets [kW/m]

Space harmonic, n	Machine C $N_{stk}=1$	$N_{stk}=2$	$N_{stk}=3$	$N_{stk}=4$
1	86.8	10.8	3.2	1.4
2	10.1	1.3	0.4	0.2
4	63.4	7.9	2.3	1.0
7	7.3	1.3	0.4	0.2
8	1.0	0.1	0.0	0.0
10	0.3	0.1	0.0	0.0
Total	168.8	21.6	6.4	2.7

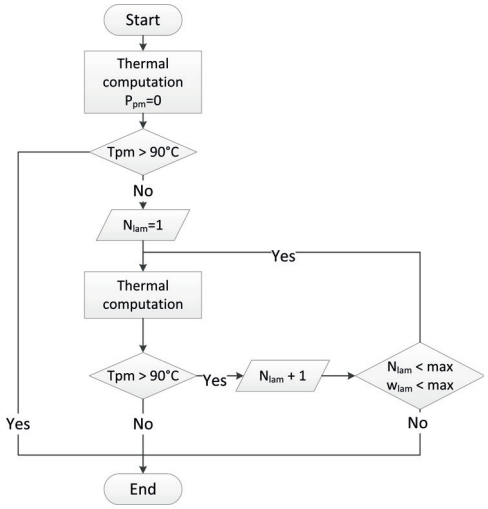

Figure 4.43: Flowchart showing the selection of N_{lam}

neglected, the magnet temperature is above the limit, then the machine design is immediately discarded. Otherwise, N_{lam} is initially set to one, and the magnet temperature is found and compared against the limiting value. If the temperature is too high, then the segmentation rate is increased until an acceptable temperature is found. If the PM temperature is not sufficiently low when the maximum number of magnet segments or the minimum segment width has been reached, the design is *discarded*.

A small cost is associated with magnet segmentation, as described in Chapter 4.10.

Conclusion of Chapter 4.7.2

The prediction of the eddy-current losses in an electrical machine is a demanding task. Here, various analytically predicted results have been compared with the results of FEA simulations. However, FEA simulations do not necessarily yield accurate results either.

Although the methods presented here have previously been used to calculate losses in other machines with fairly high accuracy, it has been shown here that they fail to correctly estimate the losses in two investigated machines. The optimisation procedure presented in this thesis requires an analysis that is valid for a wide variety of machine types and layouts.

For more precise results regarding eddy-current losses, more accurate models would be required. It is possible that the analytical methods presented in [78], [80], [90], [91], which involve complex differential equations, are capable of producing better results. However, the most accurate results would be achieved by including FEA in the optimisation routine. With the help of supercomputing and parallel processing, this may be a possibility for future work on the optimisation of electrical machines.

4.7.3 Lifetime energy loss

With information about the expected operation of the generator, the expected lifetime and the loss profile of the generator, it is possible to calculate the lifetime energy loss of the generator. The energy that is lost in the conversion of power from mechanical energy to electricity on the grid can be seen as a cost to the operator of the tidal turbine. The cost of lost energy is calculated later, in Chapter 4.10.

For a tidal energy converter, its operation is easily predicted because the predictab-

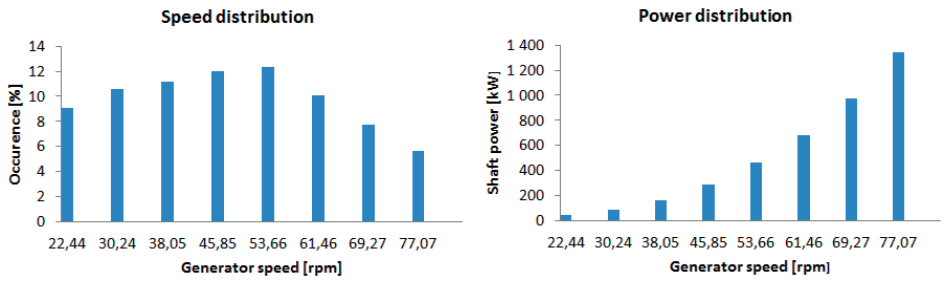

(a) Machine A **(b)** Machine D

Figure 4.44: Speed and power distributions for an 80 rpm turbine

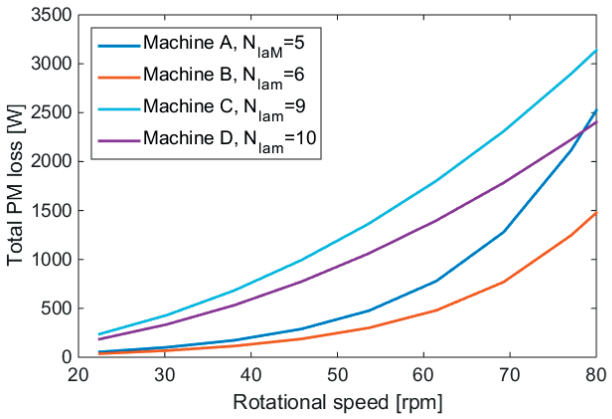

Figure 4.45: Eddy-current losses as functions of speed

ility of the tides allows the operating conditions of the turbine to be known many years in advance. Typical load characteristics for tidal turbines are used here. The power and speed distributions of the turbine are illustrated in Figure 4.44. The required torque is a function of both power and speed:

$$T = \frac{P}{2\pi \frac{n}{60}} \tag{4.65}$$

The current is proportional to the torque. The operation of the turbine is divided into 8 quantiles with equal step lengths in terms of speed. The mean current and the mean speed of each quantile are used to calculate the energy losses in different parts of the machine.

The magnet loss consists of two components: the no-load loss and the armature-induced loss. The no-load loss is proportional to the square of the speed. The armature-induced loss is proportional to the square of the speed and the square of the armature flux density. The armature flux is proportional to the stator current. The total eddy-current losses as functions of speed for Machines A-D are shown in Figure 4.45.

The copper loss is assumed to depend only on the current, not on the speed. The lamination loss depends strongly on the speed (frequency) and to a small extent on the current. In Figures 4.46 and 4.47, the losses in the different parts of the machine are shown as functions of the speed for Machines A and C. It is clear that at low speeds, the iron loss is dominant, whereas at high speeds, the copper loss is highest.

It is interesting to study the efficiency of the machine not only at its rated opera-

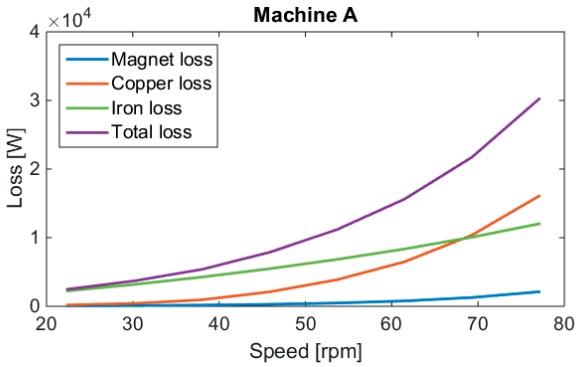

Figure 4.46: Losses as functions of speed in Machine A

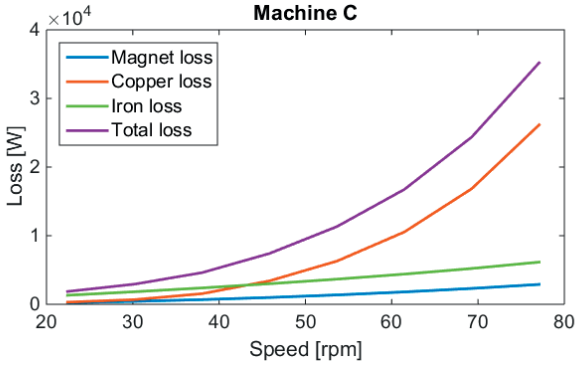

Figure 4.47: Losses as functions of speed in Machine C

tion point but also throughout the entire range of operating conditions. Figure 4.48 illustrates how the generator efficiencies change with the operating speed. All machines have efficiencies of greater than 96% above 40 rpm and lower efficiencies at low speeds. Machine D has the lowest rated efficiency, which peaks at 97.0% at 50 rpm. The efficiency of Machine C peaks at 97.5% near 60 rpm. The efficiencies of Machines A and B both peak at approximately 70 rpm. The efficiencies at rated operation are listed in table 4.18 together with magnet loss, copper loss and iron loss at rated operation.

The yearly energy loss, in kWh, is

$$E_{loss,yearly} = \sum_{q} (P_{cu,q} + P_{pm,q} + P_{iron,q}) O_q * H_{py} \tag{4.66}$$

where $P_{cu,q}$, $P_{pm,q}$ and $P_{iron,q}$ are the losses in the copper, magnets and laminations, respectively, in each quantile q; O_q is the percentage occurrence of quantile

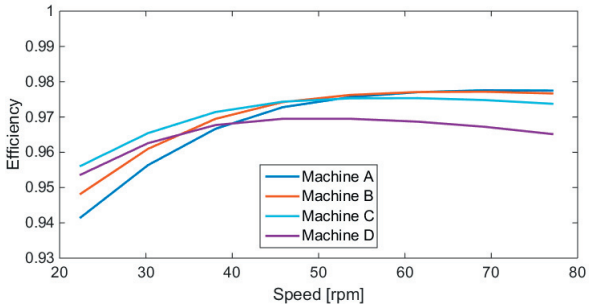

Figure 4.48: Generator efficiencies

Table 4.18: Energy losses and efficiencies

	Machine A	Machine B	Machine C	Machine D
Yearly energy loss	66.9 MWh	67.0 MWh	69.6 MWh	87.5 MWh
Rated efficiency	97.7 %	97.6%	97.3%	96.5%
Magnet loss	2.5 kW	1.5 kW	3.1 kW	2.4 kW
Copper loss	18.5 kW	24.9 kW	30.1 kW	44.0 kW
Iron loss	12.8 kW	9.5 kW	6.5 kW	6.7 kW

q, as illustrated in Figure 4.44(a); and $H_{py} = 8\ 765$ is the number of operating hours per year. The yearly energy losses of Machines A-D are listed in Table 4.18.

4.8 Thermal analysis

4.8.1 Lumped parameter thermal model

The steady-state machine temperatures at the rated operation point are calculated using a nodal network, shown in Figure 4.49, which assumes that there is no axial heat flow in the rotor and stator yokes and the housing. The heat is removed by water flowing around the generator. The nodes at which power is injected are coloured yellow.

For simplicity, the windings are modelled as a single block of coil material surrounded by mainwall insulation. Machining tolerances, air pockets and other mechanical uncertainties will lead to differences between the predicted and measured values. However, for optimisation purposes, the developed method should be sufficient, as all design variants will suffer from the same simplifications.

Losses are generated in the stator teeth, the stator yokes, the magnets, the end windings and the middle sections of the windings. The heat is removed through

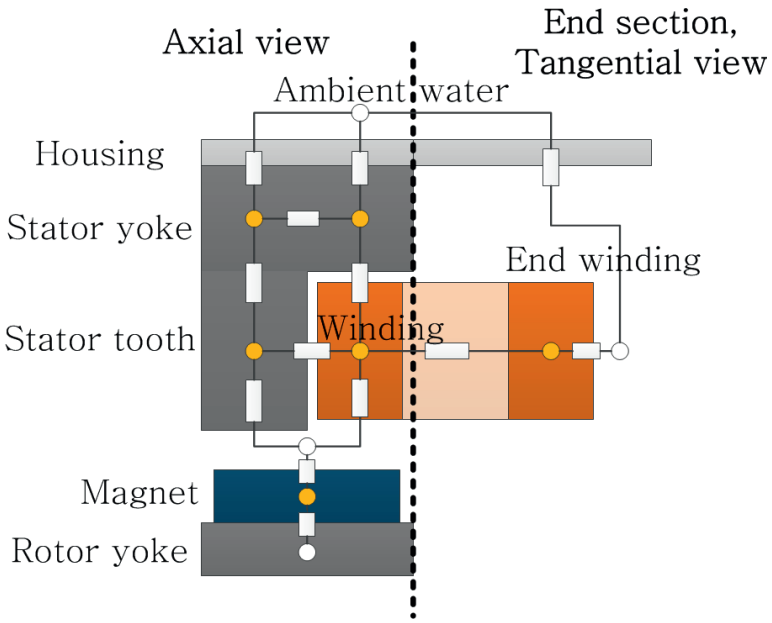

Figure 4.49: Thermal nodal network

conduction in the solids and convection between the solids and the air or water. In a solid, the thermal resistivity can be found as follows:

$$R = \frac{\delta}{\lambda A} \tag{4.67}$$

where λ is the specific thermal conductivity of the material, A is the area across which the heat is conducted, and δ is the material thickness.
For convective heat transfer, the thermal resistance is calculated as $R = 1/(\alpha \cdot A)$. In the air gap, the heat transfer coefficient is

$$\alpha = Nu \cdot \lambda / g \tag{4.68}$$

where Nu is the dimensionless *Nusselt number*. Another dimensionless quantity, the *Taylor number*, is used for convection calculations in the air gap:

$$Ta = Re^2 g / R_g \tag{4.69}$$

where Re is the *Reynolds number* and R_g is the radius at the air gap. It is assumed that there is no axial flow of air in the air gap. The relations between the *Nusselt* and *Taylor* numbers for laminar and turbulent flows can be found in [76]. For a laminar shear flow with a low *Taylor* number, the *Nusselt* number is constant [92],

Table 4.19: Thermal barriers

Description	Thickness	Conductivity
Slot wedge	1.5 mm	0.8 W/km
Housing (steel)	50 mm	40 W/km
Corrosion protection	0.15 mm	0.2 W/km
Magnet retention	0.7 mm	0.5 W/km
Turn insulation	0.15 mm	0.35 W/km
Slot insulation	2 mm	0.27 W/km
Conducting tape	0.15 mm	0.5 W/km
Glue	0.2 mm	0.2 W/km
Thermal paste	0.2 mm	0.2 W/km

Table 4.20: Conductivities of active materials

Material	Conductivity
Magnet	9 W/km
Laminated silicon steel	38 W/km
Copper	360 W/km
Winding (axial direction)	7 W/km
Air	0.023 W/km

[93], whereas for a laminar flow with vortices or a turbulent flow, it varies with the *Taylor number* as follows:

$$Nu = \begin{cases} 2 & \text{for} \quad Ta < 1700 \\ 0.128 Ta^{0.367} & \text{for} \quad 1700 < Ta < 10^4 \\ 0.409 Ta^{0.241} & \text{for} \quad 10^4 < Ta < 10^7 \end{cases} \tag{4.70}$$

The air that is contained in the end spaces and that surrounds the end windings has a low velocity. A heat transfer coefficient of $\alpha = 14 W/m^2 K$ is used [94] to calculate the convection from the end windings to the end-space air and from the end-space air to the housing.
At the rated operation point, the machine is cooled by seawater travelling with a speed of more than 1 m/s. The convection is good enough that the surface temperature can be assumed to be equal to the seawater temperature: $15\,^{\circ}\mathrm{C}$.
For accurate temperature estimation, all thermal barriers in the machine must be considered. These include the magnet retention, the glue, the insulation, the slot wedges and the corrosion protection. Table 4.19 lists the thicknesses and thermal conductivities of the various inactive parts in the machine. Table 4.20 lists the specific thermal conductivities of the active materials.

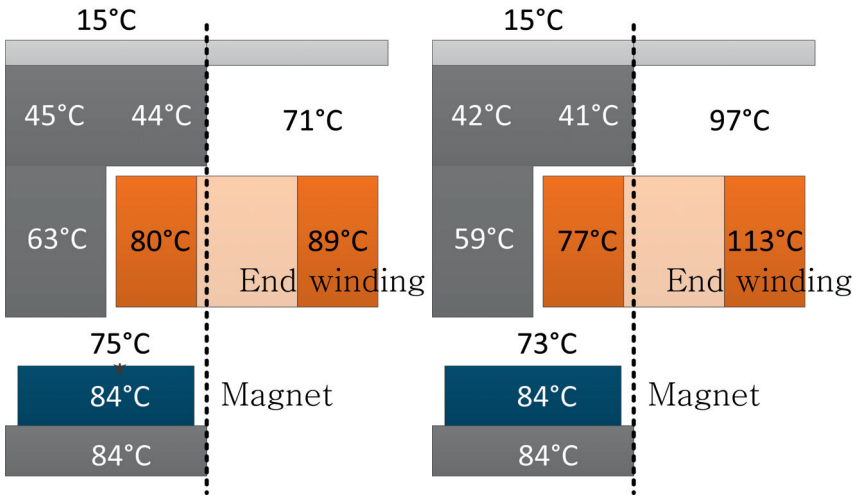

(a) Machine A **(b)** Machine C

Figure 4.50: Temperatures at all nodes

The nodal network consists of 13 thermal resistances connecting 10 nodes. The temperature rise at each node, ΔT, can be found using the following equation:

$$G\Delta\underline{T} + \underline{g}T_0 = \underline{P} \tag{4.71}$$

G and $\underline{g}$ are an inverse thermal resistance matrix and vector, respectively. T_0 is the ambient temperature, and $\underline{P}$ is the input power vector.

4.8.2 Machine temperatures

The temperatures at all nodes in Machines A and C are shown in Figure 4.50. In Machine A, the machine temperatures are relatively low, whereas in Machine C, the copper temperature is high because of the longer end windings. The power flow in Machine A is illustrated in Figure 4.51. The numbers denote the heat flows in units of kW. The yellow arrows signify power losses, and the internal heat flows are shown with blue arrows. Because of the rounding of the numbers, the values do not appear to sum correctly at all nodes. One can see that most of the heat is transmitted through the teeth.
The magnet and end winding temperatures in all four machines are listed in Table 4.21. Note that the end winding temperature in Machine D exceeds the constraint on the winding temperature, which is 135 °C.

Table 4.21: Magnet and end winding temperatures

	Machine A	Machine B	Machine C	Machine D
Magnet	84 °C	85 °C	86 °C	109 °C
End winding	89 °C	112 °C	114 °C	161 °C

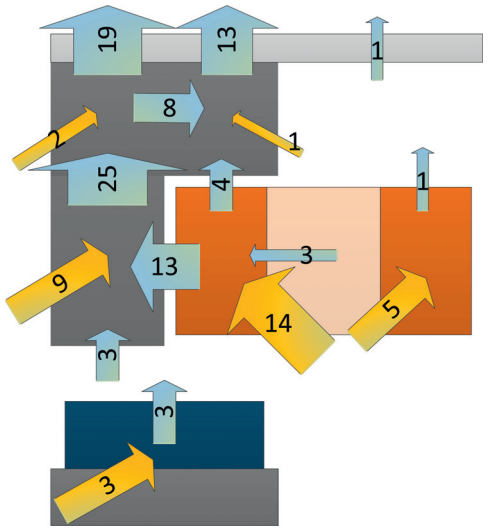

Figure 4.51: Heat flows between nodes in Machine A

4.9 Demagnetisation

The material that is most dependent on temperature is the PM material. The higher the temperature is, the lower the remanent flux density is, as shown in Figure 4.52. More importantly, the knee of the magnetisation curve moves upwards with increasing temperature. This is why the magnet temperature should not be allowed to rise above a certain limiting temperature. Here, this limit is set to 90 °C. If the flux density inside the magnet, in the magnetising direction, falls below the knee flux density value, B_D, then parts of the magnet will be permanently demagnetised. In this thesis, a B_D of -0.2 T is assumed.
The highest risk of demagnetisation occurs in the case of a short circuit on the machine terminals. The short-circuit current is

$$\widehat{I}_{sc} = 2\frac{\sqrt{2}E}{\sqrt{R_{cu}^2 + (2\pi f L_s)^2}} \tag{4.72}$$

The tooth flux density due to the armature reaction, $B_{t,ar}$, which is found in Chapter 4.4.3, is used to find the lowest magnet flux density occurring under short-

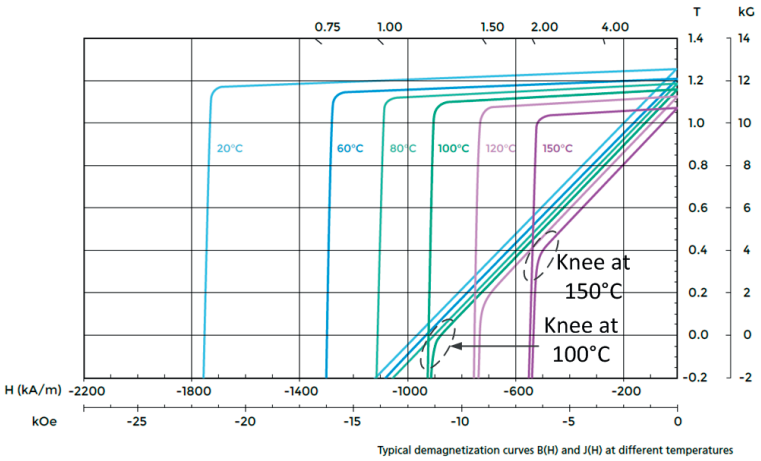

Figure 4.52: PM magnetisation curve[95]

Table 4.22: Minimum short-circuit magnet flux densities

	Machine A	Machine B	Machine C	Machine D
$B_{m,sc}$	-0.15 T	-0.01 T	-0.46 T	-0.16 T

circuit conditions:

$$B_{m,sc} = B_{m,nl} - B_{t,ar}\frac{\widehat{I_{sc}}}{\widehat{I}} \tag{4.73}$$

This equation is conservative: it does not consider iron saturation or tooth tip leakage, and it does not consider whether the short-circuit armature reaction field is located in the d-axis or the q-axis. If the short-circuit current is positive and located in the d-axis or if it is located in the q-axis, then the demagnetisation risk is considerably smaller. The minimum magnet flux densities under short-circuit conditions for Machines A-D are listed in Table 4.22.

4.10 Objective value - cost evaluation

The goal of minimising the cost of a machine is often in conflict with the goal of minimising the losses in the machine. If the energy loss is capitalised, it can be easily compared with the machine cost, and an optimal design choice that minimises the total cost can be made. In the published literature, electrical machine design optimisations have previously been presented in which the objective has been to minimise both the cost of the machine and the losses in the machine. In [96] and [97], a PM machine-converter system for wave energy applications is optimised with similar objectives; in [96], the objective is to both maximise the

power produced and minimise the cost of the system, whereas in [97] the first objective function is advanced, so that with the aid of operating profiles the energy produced is maximised. These papers present the Pareto front that arises from the two conflicting targets and offer several options to allow the designer to choose a particular balance between cost and power/energy production.
If the designer can estimate the price of electricity, it is possible to convert both objectives into the same dimension, namely, cost, and the optimisation procedure will automatically find the best weighting between them. This is done in [98], in which a generator for wave energy applications is optimised with respect to the cost of the machine and the income from energy production. In [99], a PM machine design is optimised with respect to the cost of the active materials and the cost of the losses. The machines are assumed to run at their rated speed for a given number of hours per year.

In this thesis, the cost of the machine is divided into two components: the cost of the active materials (including the housing) and the cost of the energy lost over the machine's lifetime.
The cost of the lost energy is discounted, as it will be incurred in the future.

$$\text{Energy cost} = \sum_{t=0}^{20} \frac{E_{loss,yearly} C_{energy} K_{export}}{(1+d)^t} \tag{4.74}$$

t denotes the time in years, and the expected energy price, C_{energy}, is set to 0.24 Eur/kWh. d is the discount rate, which is set to 0.2 as a conservative assumption regarding the appreciation of future income. The factor K_{export} accounts for availability and transmission loss [98]. The turbine is expected to be operational for 90% of the year, and 10% of the produced energy is assumed to be lost in transmission and in the power electronics.

The cost of the magnets, C_{pm}, depends on the magnet volume, the per-kilogram cost of the magnetic material (85 EUR/kg), the rate of segmentation and the skewing. The cost of segmenting the magnet poles is typically small. Here, the total PM cost is increased by 1% every time the number of magnet laminations is increased. As an example, a machine with 10 segments per pole will have a magnet cost that is 10% higher than the same machine with unsegmented magnets. The price of a skewed rotor is set to 1.3 times the price of an unskewed rotor.

The cost of a winding is the sum of the material cost and the cost of labour for winding and inserting the coils. The labour cost will typically be of a similar

Table 4.23: Machine costs [kEUR]

	Machine A	Machine B	Machine C	Machine D
Lifetime energy loss	70.6	69.7	73.5	92.3
Laminations + housing	32.1	25.3	49.3	44.4
Permanent magnets	41.6	35.6	49.0	38.5
Windings	12.6	16.1	22.7	31.3
Total cost	156.9	146.6	194.5	206.6

magnitude to the material cost. Here, the labour cost is modelled as proportional to the number of coils and the cost of the material:

$$C_{windings} = M_{cond} C_{cond} \left(1 + K_{labour} N_c\right) \tag{4.75}$$

$C_{windings}$ is the total cost of the windings, M_{cond} is the mass of the conductors, C_{cond} (11 Eur/kg) is the cost of the conductors, and K_{labour} is the cost of winding one coil relative to the total cost of the conductor material. The labour costs are minimised when all coils in the machine are identical. In single-layer DW machines, at least two different coil shapes are used in the windings, and K_{labour} is set to 0.013. In all other winding configurations, K_{labour} is set to 0.01. In a machine with 100 coils, the winding cost becomes twice the material cost in a double-layer or FSCW machine.

The resulting cost of the active materials is

$$\begin{aligned} \text{Material cost} = (M_{r,y} + M_{s,y}) C_{lam} + C_{windings} \\ + M_{house} C_{steel} + C_{pm} \end{aligned} \tag{4.76}$$

$M_{s,y}$, $M_{r,y}$ and M_{house} are the weights of the stator yoke, the rotor yoke and the housing, respectively. C_{lam} = 4 EUR/kg and C_{steel} = 6 EUR/kg are the costs of the laminations and steel, respectively. The values of the costs per kg are chosen based on previous experience, and they are not exact, as they will vary with dimensions, machining, supplier, etc. However, these cost parameters include, to the greatest possible extent, the costs related to production. For the magnets, coating and machining are included; for the laminations, stamping and stacking are included; for the steel, machining is included; and for the winding wires, insulation is included. The total costs and the subdivisions of the costs for Machines A-D are listed in Table 4.23.

There are some features that are not considered in this thesis. A low cogging torque, low voltage harmonics and a fault-tolerant design are examples of qualities

that are sought after in electrical machines but are not quantified here. However, the cogging torque and voltage harmonics are highly dependent on design details such as the shape of the slot openings and the shape and magnetisation direction of the magnets. Such design details are outside the scope of this thesis work.

4.11 Model verification with FEA

The four investigated machines have been modelled using the FEA approach in COMSOL to verify some of the analytical results. A comparison between the stator yoke fluxes found using the FEA and LPM methods was presented in Chapter 4.4.4. Analytically calculated values for the eddy-current PM losses were compared with FEA simulation results in Chapter 4.7.2.
Table 4.24 lists the no-load voltage values obtained via FEA simulations and analytical calculations. In the FEA simulations, the magnets are energised, the stator current is set to zero, and the rotor is revolved in a time-stepped mode. The induced voltages from all coils belonging to the same phase are summed, resulting in the total no-load phase voltages. The analytical calculations overestimate the no-load voltages by 15% for Machine A and 3% for Machine B. The analytical results are 5% and 13% lower than the FEA results for Machines C and D, respectively. The THD values for the no-load voltages obtained from the FEA simulations are also listed in the table. The third harmonic is responsible for the gross part of the harmonic distortion. The third harmonic is cancelled when the three phases are combined through a Y connection.

Table 4.24 presents the mean torques obtained in time-stepped COMSOL simulations run with energised magnets and the current placed in the q-axis for all machines. The table also presents the analytical results for comparison. The analytical equations overestimate the produced torques by 8% and 13% in Machines A and B, respectively. For Machines C and D, both results are the same. It is suspected that the expression for the Carter factor might be more correct for DW machines than for FSCW machines, which may be the cause of the more inaccurate results for the induced voltages and torques in Machines A and B. The FEA results show that the torque ripples in all machines are less than 6% of the mean torque. The torque ripple is highest in Machine D.

The FEA inductance calculations are performed in stationary mode. The current in one phase is set equal to the rated current, and the currents in the other two phases are set to zero. The amounts of magnetic energy stored in the slots, the air gap and the magnets are computed, and the self-inductance is found from the following

Table 4.24: FEA verification of the analytical results

Machine		A	B	C	D
No-load voltage (rms) [kV]	Analytical	1.65	1.59	1.56	1.57
	FEA	1.43	1.54	1.65	1.80
THD of no-load voltage	FEA	5.4%	5.4%	8.3%	3.1%
Torque [kNm]	Analytical	179	179	179	179
	FEA	166	159	179	179
Torque ripple [kNm]	FEA	3.5	4.1	5.6	10.3
Self-inductance [mH]	Analytical	7.13	5.06	9.52	9.27
	FEA	7.07	4.07	8.95	8.67

equation:

$$W_{self} = \frac{1}{2} L_{self} I^2 \tag{4.77}$$

The analytical self-inductance is

$$L_{self} = (L_{mph} + L_{\delta} + L_{slot} + L_{tt} + L_{sq}) \tag{4.78}$$

Among the values compared in Table 4.24, the end winding inductance is not included. The results show that the difference is less than 7% in all machines except Machine B, for which the difference is 24%.
The presented results indicate that the analytical calculations are able to estimate the performance of the machines to a sufficient degree, but they could be further improved. The calculation of the Carter coefficient is a matter of concern. It is possible that different equations should be used for FSCW and DW machines; however, it is necessary to establish the best criterion for determining which equation should be used. The inductance calculation for double-layer FSCW machines should also be improved.

Figure 4.53 shows the flux density and flux lines in Machine D at the rated load.

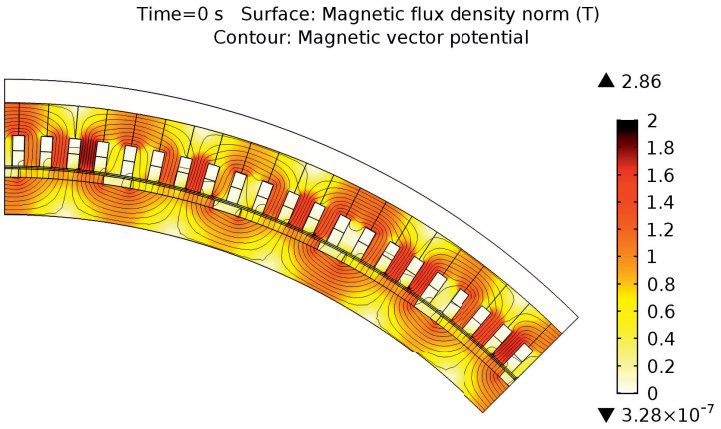

Figure 4.53: Flux density and flux lines in Machine D at the rated load

Chapter 5

Optimisation

5.1 Introduction

This chapter begins with a description of nonlinear optimisation and an explanation of the differences between the two main categories of optimisation methods used for engineering problems. Two different methods, one gradient-based algorithm and one genetic algorithm, are chosen for this study, and they are both described here. Thereafter, the settings for the algorithms are presented, followed by a discussion of the methods' abilities to locate the global minimum.

The optimisation itself is split into two parts. First, a gradient-based algorithm is used to solve the problem. The gradient-based solver solves a reduced subproblem in which the winding layout is restricted to a single-layer concentrated design with a limited number of possible slot-and-pole combinations. Although this method is not capable of searching between the different winding types, the algorithm can be very useful for machine designers and is used here to illustrate different trends and relationships.
Second, a direct optimisation method is used to solve the problem. It is combined with the gradient-based algorithm to form a hybrid optimisation procedure that takes advantage of the strengths of each method.

Optimisation with variable numbers of slots and poles

The choice of the optimal slot-and-pole combination is often discussed in the literature in relation to the cogging torque [60]. However, in problems involving the minimisation of the cost or weight of a machine, the numbers of poles and slots are often fixed [100], [101], or the number of slots per pole and phase is fixed [102].

A study that resembles the one presented in this thesis can be found in [102]. It addresses the optimisation of a wind energy conversion system, including the gear system. The system cost is found as a function of both the rated power and the gear ratio. For each combination of gear ratio and power, the main dimensions of the generator are optimised. The number of slots per pole and phase is fixed to 1 in all cases. The optimal number of poles as a function of the gear ratio is not shown. The results indicate that the optimal gear ratio varies from 4.55 for a 750 kW turbine to 9.7 for a 10 MW turbine.

In [103], six different slot-and-pole combinations are investigated. The winding factor is the same for all six combinations. The stator and rotor dimensions are optimised for each case, and the resulting designs are compared. The cogging torque, torque density, iron losses and eddy-current losses are compared. It is shown that for the same current density and slot area, the torque density varies even when the winding factors are the same. This finding indicates that it is not sufficient to focus on the winding factors alone when optimising electrical machines.

5.2 Nonlinear optimisation

Constrained minimisation is the task of finding the set of n variables $\mathbf{X}$=(x_1, ..., x_n) that result in the lowest possible scalar value $f(\mathbf{X})$ subject to a set of m constraints, $G_k(\mathbf{X}) \leq 0$, k=1, ..., m. The feasible region is the set of sets $\mathbf{X}$ for which all constraints $G_k(\mathbf{X}) \leq 0$ are satisfied.
At the optimal point, X_o, a constraint can be either *active* or *non-active*. For active constraints, $G_k(\boldsymbol{X})$ = 0, whereas for non-active constraints, $G_k(\boldsymbol{X}) < 0$. As an example, the constraint on the maximum active length (3 m) is non-active at the optimal point for most cases presented in this chapter. This means that in the optimal design, the active length is less than 3 m. At the same point, other constraints may be active. For example, the maximum outer diameter (3.5 m) is active in many of the considered cases. This means that the outer diameter of the optimal design is 3.5 m; the constraint actively prevents the optimal point from shifting into the infeasible region. One property of an active constraint is that the optimal value of f will change if the value of the constraint is altered. If the change results in an increase in the size of the feasible region, then the optimum will improve, whereas if the change causes a reduction of the feasible region, the optimum will deteriorate.
In iterative optimisation algorithms, the investigated point moves in the direction of the optimal point. Each investigated point will have a different set of constraints that are active.
In a linear problem, the objective function f is a linear function of $\mathbf{X}$, and the con-

straint function $G_k(\mathbf{X})$ is also a linear function of $\mathbf{X}$. Such problems can be solved using the relatively simple simplex method, and the optimal value will always lie in a corner of the feasible region.
PM generator design is a nonlinear problem, which means that the global optimum may lie either on the edge of the feasible solution space or in the middle of the feasible solution space. Nonlinear problems can also have several local minima. Some optimisation algorithms are able to locate several minima, whereas others can find only one.

Optimisation techniques can be roughly divided into two classes: *direct optimisation* techniques and *gradient-based optimisation* techniques.

Gradient-based optimisation algorithms are iterative methods that use either the gradient or the Hessian of the objective function to find a search direction. Gradient-based algorithms converge to either a local optimum, a global optimum or an infeasible solution, depending on the starting point. One shortcoming of these methods is their inability to solve problems with integer variables and non-smooth objective functions and constraints. This is because the gradient cannot be evaluated throughout the entire region. The other disadvantage of gradient-based algorithms is that they can find only local minima. Direct optimisation methods require only the numerical values of the objective function and the constraints and can therefore cope with nonlinear, non-smooth and mixed-integer problems. The downside of direct optimisation is the time required to find the solution, especially when there are many variables and the variables have wide bounds.

Both types of optimisation methods are used in this work. In the first section of Chapter 6, a reduced problem is solved in which the integer variables are fixed. The global minimum is found by searching the variable space from numerous starting points. In the second section, the full problem is solved. A direct optimisation method is used in an initial search for the global minimum in this case. Finally, a hybrid method incorporating both of the aforementioned methods is used to locate the minimum.
First, a reduced problem is created in which the integer variables are fixed. The global minimum is found by searching the variable space from numerous starting-points. Second, the full problem is solved. A genetic algorithm is initially used to search for the general vicinity of the global minimum in this case. Thus, a hybrid method incorporating both of the aforementioned methods is used to locate the global minimum.

5.3 Gradient-based optimisation

5.3.1 Introduction

There are many types of gradient-based methods with different levels of complexity and efficiency. A gradient-based algorithm evaluates either Hessians, gradients, or merely function values. The Hessians are the second-order derivatives of the objective function with respect to the variables. The computational complexity per iteration is highest when the Hessians are computed; however, fewer iterations are usually necessary before the minimum is found. Which method is best suited for a problem depends on the application.
One disadvantage of iterative methods is that they can only locate local minima. The starting point of the search determines which minimum is found. By repeating the search from many starting points, it is possible to find several minima.
Another shortcoming is that such methods require smooth problems and no integer variables. In the PM generator optimisation problem, there are four integer variables. Problems with only a few integer variables can be solved to a certain extent. An integer variable can be transformed into a continuous variable, as is done in [104], or a basic grid search can be performed separately from the optimisation process.
In the first section of Chapter 6, the problem is reduced to include only one integer variable: the number of base windings. A grid search investigating each possible number of base windings is performed, and the optimum is found for each. The procedure is further explained below.

It has been argued that a global optimisation technique is necessary for machine design optimisation, simply because of the existence of many local minima. Despite this, however, many researchers in this area have used various gradient-based algorithms. In [101], [105], sequential quadratic programming (SQP) methods are used to optimise synchronous reluctance motors. The pole face of a synchronous machine is optimised using the SQP method in [106], and SQP is also used in [107] to optimise a PM generator design.

5.3.2 MATLAB gradient-based optimisation method, *fmincon*

A minimisation method that is readily available to most machine designers is tested in this work. Three algorithms are available for the *fmincon* function in MATLAB R2014a. These were investigated by the author in [41], and based on that work, the algorithm named *sqp* is selected for this study because it is more likely to find a feasible solution from a random starting point than the other two algorithms are.

The *sqp* algorithm uses the Karush-Kuhn-Tucker equations to solve the constrained

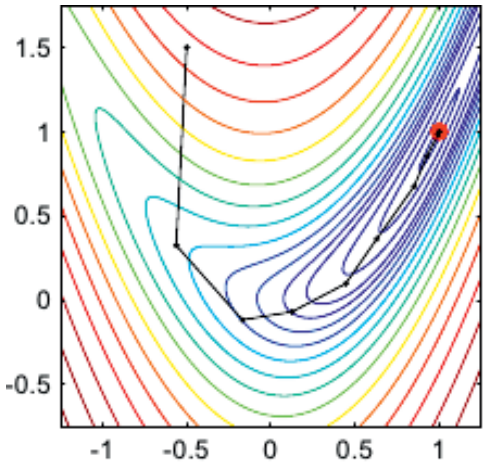

Figure 5.1: Newton line search (source: [109])

problem [108]. These equations form the basis of many nonlinear programming algorithms. In each major iteration, the Hessian of the Lagrangian function is approximated using a quasi-Newton updating method. This approximation is then used to generate a quadratic programming subproblem whose solution is used to choose a search direction for a line search procedure. The active nonlinear constraints are linearised in each subproblem iteration.

The user supplies a starting point, and the algorithm uses quasi-Newton approximation to compute the Hessian, which dictates the direction of the search for the next point. At each new point, the Hessian is recalculated, until the solver converges to a solution or stops because it cannot find a feasible solution. Figure 5.1 shows how each iteration converges to the optimum for the Rosenbrock function when Newton's method is used together with an optimal line search strategy [109].

A search for multiple minima can be performed by starting from multiple different starting points. The MATLAB functions *MultiStart* and *GlobalSearch* use a random search within the specified bounds to search the variable space for different minima [108]. Here, the *MultiStart* procedure is used. The algorithm generates a specified number of random points within the given bounds, and *fmincon* is run from each initial point, each resulting in either a feasible or infeasible point. Each run is independent of the others, and the procedure can be run in parallel.

5.3.3 Implementation of a gradient-based method (*fmincon*)

The *fmincon* algorithm is an iterative method that can be applied to problems with only real-valued variables. Hence, the full problem presented in this thesis cannot be solved using this algorithm. However, it is of interest to demonstrate the possibilities that this method provides for the optimisation of electrical machine designs. A reduced problem is constructed in which the number of variables is reduced from 12 to 9 (see Table 5.1). The integer variables p, $Q_p/2$, N_{layer} and y_{sp} are eliminated, and a new integer variable, n_{base}, is introduced. The machine now consists of n_{base} base windings, each with 22 poles and 24 slots. The number of winding layers is set to 1. This is an FSCW machine with the same slot-and-pole configuration as that of Machine A. This is a slot-and-pole combination with which the author has considerable experience. The winding topology provides a low cogging torque and simple assembly.

The number of base windings is an integer, and a basic grid search is conducted to solve the problem. One iterative optimisation procedure with 8 real-valued variables is performed for each possible number of base windings. The flowchart in Figure 5.2 illustrates the workflow for the grid search. For the case of a one-stage gear train, n_{base} cannot be higher than 13 because of the constraint on the generator frequency.
Another integer parameter that is used in the analysis is the number of magnet laminations. The procedure for finding the optimal number of laminations is a non-smooth operation, and the *fmnincon* algorithm can have difficulty converging when the problem is not smooth. Therefore, the value of the parameter N_{lam} is fixed in this reduced problem.

A similar optimisation routine was presented by the author in [41]. The fitness function did not include the energy loss; however, a constraint was imposed on the minimum efficiency. The feasible solution space for that problem was very small because of the constraint on the efficiency. As a result, it was challenging for the optimisation algorithms to locate a feasible solution. The *fmincon* algorithm proved to be an effective tool; however, a multistart method was needed to find the global optimum. For verification, a GA was also used to search for the global optimum, but it was unable to locate a feasible solution unless the bounds on the variables were narrowed considerably.

Bounds

The bounds on the optimisation variables prevent the algorithm from investigating solutions with variable values that are not feasible.

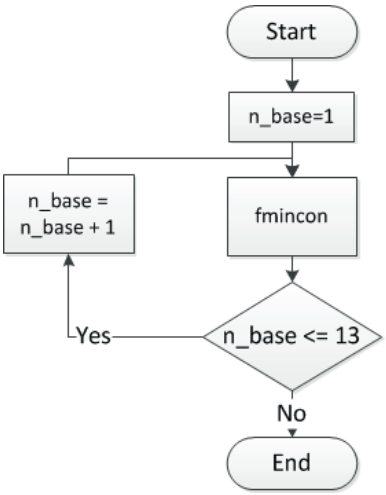

Figure 5.2: Grid search with *fmincon* and the integer-valued variable n_{base}

Table 5.1: Bounds for *fmincon*

Variable		Lower	Upper
R_{inner}	m	0.229	1.676
$d_{s,yoke}$	mm	5	1 000
d_{slot}	mm	6	400
w_{slot}	mm	4.5	437
l_m	mm	2	100
α_m		0.5	0.97
$d_{r,yoke}$	mm	5	1 000
J	A/mm^2	0.1	10
n_{base}	int	1	13

A constraint on the shaft strain ensures a shear stress on the shaft of less than 30 MPa. The relationship between the shear stress, the torque and the radius of a shaft with a circular cross section is described by equations (4.44) and (4.45). This constraint sets a lower limit on the shaft radius. This becomes the lower bound on the inner radius of the generator:

$$R_{inner,min} = \sqrt[3]{2T/30 \text{ MPa}} = 0.229 \text{ m} \tag{5.1}$$

The rated torque, T, of the generator is 179 kNm in the case of a single-stage gear train.

The upper bound on the inner radius of the generator is found from the maximum outer diameter, 3.5 m; the minimum thicknesses of the yokes, magnets and slot

depth; and the air gap length and housing thickness.
The highest possible stator bore radius is 1.689 m. The maximum slot width can be expressed as a function of the number of base windings:

$$w_{slot,max} = \tau_u - w_{tooth,min} = \frac{2\pi 1.689 \text{ m}}{24 \cdot n_{base}} - 5 \text{ mm} \tag{5.2}$$

τ_u is the slot pitch, and $w_{tooth,min}$ is the minimum tooth width. When n_{base} is 1, the maximum slot width is 437 mm.
The upper bounds on the yoke thicknesses, slot depth and current density are set for reasons of practicality.

Global minimum

The global minimum can be located by running the *fmincon* algorithm from multiple starting points. Each run results in either an infeasible point or a feasible local minimum. Many of these local minima may be so close that they can be considered identical. The user can specify the tolerances on the objective value and the Euclidean distance between points that are used to determine whether two points are identical. Here, the tolerance on the objective value for considering two points to be identical is set to 1000 EUR, and the tolerance on the distance between points is set to 0.03. A small tolerance will result in many solution points, and a large tolerance will lead to fewer solution points.

In the PM machine design problem presented by the author in [41], the *MultiStart* function in MATLAB was used to investigate the presence of local minima. From 10 different starting points, 6 minima were located. Five of these minima had very similar variable values, with the objective values varying by 6%. The last local minimum exhibited an objective value that was 3.7 times higher than the global minimum.

For the problem considered in this work, *MultiStart* is also used to search for local minima. With the number of base windings fixed at 7, among 364 runs from different starting points, 193 of these runs result in feasible solutions. Forty of the runs yield the same point, namely, the global minimum. Ninety-seven (50%) of the feasible solutions have objective values that are less than 1000 EUR higher than the global minimum, and 117 have objective values that are less than 5% higher. The highest of the local minima is 4.1 times higher than the global minimum.

The random starting points generated by *MultiStart* have variable values that lie within the specified variable bounds. When the bounds on the variables are far apart, a large proportion of the generated starting points will not yield feasible results. Table 5.1 provides the limiting bounds for the reduced problem. If these bounds are used in the *MultiStart* procedure, only a few feasible points are gener-

ated. Therefore, the bounds are adjusted manually to ensure that the global minimum is located.

Various gear ratios

Three different gear ratios are considered for optimisation. First, a single-stage gear train is assumed, corresponding to a generator speed of 80 rpm. The number of base windings is allowed to vary from 1 to 13, and the optimal machine design and the active constraints are recorded for each number of base windings.
Second, a direct-drive generator is investigated. The number of base windings is allowed to vary between 1 and 36; however, feasible solutions are only found for n_{base} values from 3 to 22.
Finally, the optimal generator with a two-stage gear train and a speed of 360 rpm is investigated. Here, the maximum number of base windings is 3.

5.4 Direct optimisation

5.4.1 Introduction

In many direct optimisation methods, neither gradients nor Hessians are evaluated. These methods are also called *heuristic* or *global* optimisation methods. Only the objective value of each individual is calculated and used as the basis for generating new individuals; therefore, these methods can be used to solve problems for which gradients cannot be calculated. Because such a method does not require a starting point, the solution is not trapped into a local minimum by the chosen starting point. Consequently, direct optimisation methods are more effective at searching for the global minimum. Direct optimisation methods tend to require many more evaluations than iterative methods do, but it is typically possible to take advantage of parallel computing for individual evaluations. A direct optimisation method often yields a quasi-global solution that is close to the optimum. This solution can then be refined using a gradient-based algorithm.

The list of direct optimisation methods is long, and its length is increasing, as new methods are continuously being developed. In [110], a review of various optimisation techniques (both gradient-based and direct optimisation) that are used for electrical machines problems is presented. Global optimisation methods include, but are not limited to,

- Memetic algorithms
- Differential evolution

- Evolutionary algorithms
- Dynamic relaxation
- Genetic algorithms (GAs)
- Particle swarm optimisation (PSO)
- Artificial bee colony optimisation
- Simulated annealing

GAs have been widely used in electrical machine design optimisation [100], [102], [111], [112]; however, other evolutionary algorithms, such as immune algorithms, evolution strategies, differential evolution [113], [114] and particle swarm optimisation [115], [116] also show good results.
In many cases, a hybrid solution is employed in which an evolutionary algorithm is used to find the general vicinity of the global minimum and a local search algorithm is then used to find the precise location of the minimum [116]–[119]. This drastically reduces the number of evaluations that must be performed.

The author participated in evaluating hybrid optimisation methods using both a GA and PSO in [116]. The problem specification resulted in a very narrow solution space because of its tight constraints, and neither the GA nor the PSO algorithm was able to find a feasible solution. However, when they were combined with the gradient-based *fmincon* function, both were able to find designs close to the global minimum. The two methods yielded comparable results. The hybrid PSO method showed slightly better performance; however, because MATLAB provides a GA that is easy to use, this latter method has been chosen as the direct optimisation method applied in the current study.

5.4.2 Genetic algorithm

Genetic algorithms use concepts from evolutionary theory and hereditary. A GA mimics the process of natural selection by choosing the best individuals from a population to produce the next generation using crossover and mutation operators [120].
First, an *initial population* is created. This is usually a selection of individuals with variable values that are randomly selected from between the upper and lower bounds. User-defined initial populations can also be specified. The diversity of the population is important for the performance of the GA, as explained in [121]. The diversity is controlled first by the initial range of the population and thereafter

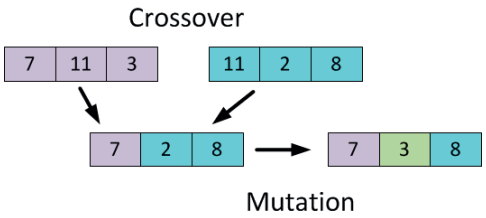

Figure 5.3: Crossover and mutation operations

by the extent of mutation. The creation of the initial population for this work is explained in the next section.
Subsequently, the fitness values of all individuals in the initial population are evaluated, and the best individuals are selected for crossover. The objective values of these individuals can have a large spread. To remove the effect of the spread, a *scaling function* is used to scale the objective value based on the rank of each individual instead of using its raw objective value [122]. An individual of rank r has a scaled score proportional to $1/\sqrt{r}$.
The *selection* of the parents for the next generation can be performed in several different ways (e.g., roulette, tournament, or remainder). For mixed-integer problems, MATLAB uses the stochastic universal sampling method, in which the probability of selecting an individual as a parent is proportional to its scaled fitness value.
When the parents have been chosen, the children that will constitute the new generation are created.
The majority of the children in the new generation are created through *crossover*. Each child receives a combination of genes from two parents from the preceding generation. Thus, the best genes are passed to the next generation.
Other children are created through *mutation*. This process introduces a small, random change in the genes of each such child, thereby providing genetic diversity and expanding the search space. Figure 5.3 illustrates how the crossover and mutation operations function.
A small number of the best-ranked individuals in each generation, the *elite*, are directly passed to the next generation. This ensures that the best genes are preserved; however, it also increases the risk of converging to a local minimum.
New generations are repeatedly created until a stopping criterion is met. One possible stopping criterion is a maximum number of generations. Another is that the best fitness value remains unchanged after several generations.

Although GAs are among the class of optimisation methods referred to as global optimisation methods, there is no guarantee that a GA will be able to locate the

Table 5.2: GA bounds

Variable		Lower	Upper
p		1	400
$Q_p/2$		1	40
N_{layer}		1	2
y_{sp}		0	2
R_{inner}	m	0.229	1.676
$d_{s,yoke}$	mm	5	1 000
d_{slot}	mm	6	800
w_{slot}	mm	4.5	437
l_m	mm	2	100
α_m		0.45	0.97
$d_{r,yoke}$	mm	5	1 000
J	A/mm^2	0.1	10

global minimum. The variable bounds are very important in this respect. If the bounds are set too wide, there is a risk that none of the individuals in the initial population will be feasible. In that case, the GA will most likely not find the global optimum.

In theory, to ensure that the global optimum is found, the population size must approach infinity, and the number of generations must be very high. In reality, however, the population size and the number of generations must be limited. The solution may therefore not be the global optimum. In [116], GA optimisation was repeated either 100 or 200 times for each case. This study produced statistical data that revealed that the minimum cost found varied dramatically from one run to another.
For the analysis reported in this thesis, the population size is much larger than that in [116], but the GA is not repeated many times. Therefore, it is possible that the optimal results presented here do not represent the global minimum. However, the general trends are clear from analysing the results, which is sufficient for the scope of this thesis.

5.4.3 Implementation of the genetic algorithm

Bounds and constraints

The bounds on the first 8 variables presented in Table 5.1 also apply to the problem solved using the genetic algorithm. The allowed number of poles varies with the generator speed. At 15 rpm, the number of pole pairs can be as high as 800 before

the electrical frequency limit of 200 Hz is reached. At 1050 rpm, the maximum allowed number of pole pairs is 22. The number of slots is limited by the minimum slot width and tooth width and by the maximum outer diameter. The number of slots cannot be higher than 240. Only single-layer and double-layer windings are investigated, and the short-pitch factor cannot be greater than 2.

To reduce the size of the variable space, the bounds presented in Table 5.2 must be narrowed in each optimisation run. The upper bounds are reduced, and the lower bounds are increased; both modifications are made manually.

Still, certain combinations of variable values that lie within these bounds yield machine designs that are infeasible. As an example, a machine with $Q_p/2 = 28$ (168 slots), a stator inner radius of 1.4 m and a slot width of 55 mm would have a slot width larger than the slot pitch (52.5 mm). Performing an analysis of this machine would yield a negative tooth width, which, in turn, would result in a negative flux density, a negative iron loss, and possibly time-consuming thermal calculations. In a GA, random combinations of variable values are created, and consequently, the majority of individuals may be infeasible. Therefore, a number of linear constraints are included to reduce the number of infeasible designs. The first linear constraint maintains the maximum outer diameter:

$$2(R_{inner} + d_{r,yoke} + l_m + g + d_{slot} + d_{s,yoke} + d_{house}) \leq 3.5 \text{ m} \tag{5.3}$$

The next linear constraint ensures that the slot pitch is always larger than or equal to the sum of the minimum tooth width and the minimum slot width:

$$\frac{2\pi}{Q}(R_{inner} + d_{r,yoke} + l_m + g) \geq (5 + 4.5) \text{ mm} \tag{5.4}$$

A machine with a number of slots that is much smaller than the number of poles has a very low pitch factor and will not correspond to the optimal generator design. According to [123], machines with q values lower than 0.25 have pitch factors of less than 0.866. Thus, a constraint is imposed to ensure that q will not be lower than 0.25:

$$q = \frac{Q}{2pN_{ph}} \geq 0.25 \tag{5.5}$$

To limit the number of possible outcomes, an upper limit is also placed on q:

$$q = \frac{Q}{2pN_{ph}} \leq 3 \tag{5.6}$$

Only machines with distributed windings and double-layer windings are allowed to be short-pitched. A linear constraint is added to ensure that the short-pitch factor is zero if the number of winding layers is one:

$$y_{sp} \leq 2(N_{layer} - 1) \tag{5.7}$$

Initial population

The default method of creating an initial population is to create random combinations of variables between the upper and lower boundaries. If this is done, a very small portion of the initial population will satisfy the imposed linear constraints, and the initial population will likely contain no feasible solutions at all. Therefore, a user-defined initial population is created.

For each new individual, p and $Q_p/2$ are randomly chosen to lie between the upper and lower boundaries. If the combination satisfies equation 5.5 and 5.6 and the number of slots is not equal to the number of poles, then a machine design is created. In the case of an 80 rpm design, the initial individuals are created with the following characteristics:

- Rotor yoke thickness = 0.6 · Pole pitch
- Random magnet length
- Slot width = 0.5 · Slot pitch
- Stator yoke thickness = Rotor yoke thickness
- Slot depth = 2 · Slot width
- Outer diameter between 3.3 and 3.5 m
- Random current density
- Random number of winding layers
- Random short-pitch factor, if allowed

Some of these characteristics change when the generator speed is higher or lower than 80 rpm. For higher-speed machines, the outer diameter is not specified. The inner radius is randomly chosen to lie between specified lower and upper boundaries.

Only individuals that satisfy the set of linear equations are accepted into the initial population. A majority of the initial individuals are not feasible with respect to the nonlinear constraints. However, with a sufficiently large population, enough feasible individuals are created for the GA to solve the problem.

Table 5.3: GA settings

GA parameter	Value
Population size	1000-1500
Crossover fraction	0.75-0.8
Elite count	25
Stall generation limit	20-30
Maximum number of generations	100

GA settings

The population must be large enough to exhibit a sufficiently high diversity. The number of individuals in each population is set to a minimum of 1000. The population size setting is listed in Table 5.3 along with the other settings for the genetic algorithm.
The crossover fraction is the fraction of children in one generation that are created through crossover between parents from the previous generation. The elite count is the number of the best-ranked individuals that are carried over to the next generation. If the best individual does not change from one generation to the next, then the number of stall generations increases by one. If the number of stall generations reaches the stall generation limit before a better individual is found, then the algorithm stops. The algorithm also stops when the number of generations reaches the maximum number of generations.

5.5 Hybrid algorithm

5.5.1 Introduction

The genetic algorithm finds a quasi-optimal solution in the vicinity of the optimal solution; however, the number of generations needed to navigate from the region around the optimal solution to the very best solution is very high. A more effective method is to use the GA results as starting points for a gradient-based algorithm. In the hybrid algorithm, the two techniques presented in this chapter are employed as two sequential stages of optimisation. First, the GA locates the regions that are most likely to contain the global minimum. Then, the gradient-based algorithm takes over. This methodology is also used in [119], in which the single best individual found by a GA is used as a starting point for a sequential quadratic programming algorithm.

A similar hybrid method is to apply the iterative algorithm to all individuals in the current generation and then returning the newly improved individuals to the popu-

lation [124]. However, this cannot be done using MATLAB's built-in GA function. The use of hybrid optimisation techniques that combine several different optimisation techniques is fairly common for engineering problems [117]–[119], [124], [125]. In [110], the authors present a review of various optimisation algorithms used to address PM electrical machine design problems.

5.5.2 Implementation of the hybrid algorithm

The thirty best individuals from the final population are selected for further optimisation. This subpopulation contains individuals with different numbers of poles, slots and winding layers and various pole pitch factors. These integer variables cannot be treated as variables in the *fmincon* algorithm. Some of the individuals in the subpopulation will share the same set of integer variables. Only one of each set of individuals with the same integer values is selected as a starting point for the iterative solver. The selected individuals from the list of the thirty best individuals are highlighted in Figure 5.4. The integer-valued variables are fixed, and one optimisation is run with each individual as the starting point, using *fmincon* as the optimisation algorithm.

5.5.3 Investigations

In the next chapter, the case of a generator with a single-stage gear train is thoroughly investigated. The difference between the results obtained from the GA and the hybrid solver is discussed. The calculated sensitivities to certain machine parameters are reported.

Thereafter, the optimal machine design is described as a function of the generator speed. The optimal generator designs are found for six different generator speeds.

The workflows of the two optimisation procedures are illustrated in Figure 5.5. As shown on the left side of the figure, the gradient-based optimisation begins with the reduction of the problem (by fixing the values of the integer variables), followed by the solution of a series of problems with an increasing number of base windings. The machine design with the lowest cost is the solution to the reduced problem. This procedure is repeated for three different generator speeds. As shown to the right, the genetic algorithm is applied to the full problem and produces a set of individuals that are passed on to the gradient-based solver. Each of these individuals is improved, and the best one is selected as the result of the hybrid solver. This procedure is repeated for six different generator speeds.

R_{inner}	$d_{s,yoke}$	d_{slot}	w_{slot}	l_m	α_m	$d_{r,yoke}$	J	$Q_p/2$	p	N_{layer}	Y_{sp}
1.48	0.0427	0.0773	0.0381	0.0123	0.945	0.0377	3.16	**21**	**56**	**2**	**0**
1.47	0.0523	0.0753	0.0411	0.0168	0.916	0.0451	3.22	**18**	**48**	**2**	**0**
1.48	0.0417	0.0765	0.0354	0.0155	0.890	0.0331	3.28	**22**	**55**	**2**	**0**
1.48	0.0472	0.0718	0.0352	0.0140	0.891	0.0325	3.35	**22**	**55**	**2**	**0**
1.48	0.0472	0.0760	0.0364	0.0152	0.884	0.0419	3.35	**20**	**50**	**2**	**0**
1.48	0.0471	0.0760	0.0364	0.0152	0.884	0.0420	3.36	**20**	**50**	**2**	**0**
1.43	0.0509	0.0716	0.0404	0.0145	0.902	0.0440	3.22	**20**	**50**	**2**	**0**
1.48	0.0471	0.0760	0.0364	0.0152	0.884	0.0421	3.36	**20**	**50**	**2**	**0**
1.50	0.0532	0.0743	0.0400	0.0170	0.915	0.0435	3.27	**18**	**48**	**2**	**0**
1.49	0.0498	0.0718	0.0359	0.0143	0.889	0.0329	3.37	**22**	**55**	**2**	**0**
1.48	0.0470	0.0761	0.0363	0.0153	0.884	0.0420	3.35	**20**	**50**	**2**	**0**
1.46	0.0502	0.0713	0.0354	0.0139	0.890	0.0332	3.40	**22**	**55**	**2**	**0**
1.46	0.0502	0.0713	0.0354	0.0139	0.890	0.0332	3.40	**22**	**55**	**2**	**0**
1.46	0.0502	0.0713	0.0354	0.0139	0.890	0.0332	3.40	**22**	**55**	**2**	**0**
1.46	0.0502	0.0713	0.0354	0.0139	0.890	0.0332	3.40	**22**	**55**	**2**	**0**
1.46	0.0502	0.0713	0.0354	0.0139	0.890	0.0332	3.40	**22**	**55**	**2**	**0**
1.46	0.0502	0.0713	0.0354	0.0139	0.890	0.0332	3.40	**22**	**55**	**2**	**0**
1.45	0.0506	0.0719	0.0349	0.0140	0.891	0.0333	3.42	**22**	**55**	**2**	**0**
1.48	0.0345	0.0761	0.0356	0.0155	0.883	0.0333	3.20	**22**	**55**	**2**	**0**
1.48	0.0346	0.0760	0.0355	0.0155	0.883	0.0334	3.21	**22**	**55**	**2**	**0**
1.49	0.0437	0.0769	0.0380	0.0151	0.878	0.0442	3.06	**20**	**50**	**2**	**0**
1.47	0.0409	0.0737	0.0383	0.0164	0.876	0.0369	3.12	**22**	**55**	**2**	**0**
1.48	0.0345	0.0761	0.0354	0.0155	0.883	0.0336	3.212	**22**	**55**	**2**	**0**
1.47	0.0303	0.0725	0.0387	0.0172	0.877	0.0287	3.23	**22**	**55**	**2**	**0**
1.43	0.0462	0.0752	0.0366	0.0149	0.884	0.0473	3.36	**20**	**50**	**2**	**0**
1.56	0.0414	0.0587	0.0354	0.0204	0.894	0.0301	2.91	**29**	**71**	**2**	**0**
1.39	0.0648	0.0544	0.0321	0.0203	0.894	0.0291	2.32	**19**	**75**	**2**	**0**
1.42	0.0406	0.0611	0.0304	0.0188	0.914	0.411	3.07	**21**	**57**	**2**	**0**
1.35	0.0439	0.0609	0.0441	0.0189	0.870	0.0235	3.20	**20**	**64**	**2**	**0**
1.52	0.0394	0.0514	0.0300	0.0208	0.889	0.0421	2.81	**23**	**73**	**2**	**0**

Figure 5.4: Individuals selected as starting points for *fmincon*

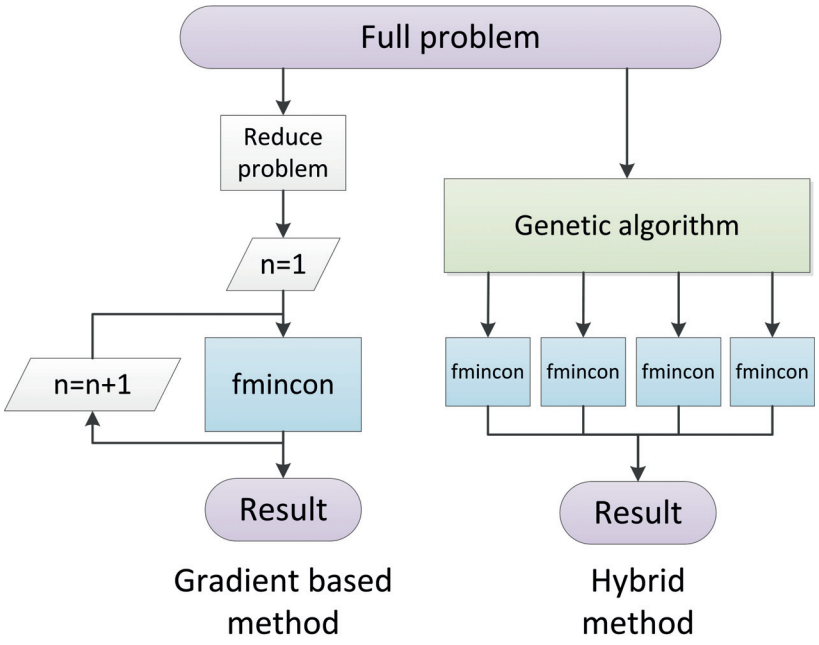

Figure 5.5: Workflows of the optimisation methods

Chapter 6

Results

6.1 Introduction

An optimisation tool can be used for more than simply finding one optimal machine design. The strength of such a tool is that it can also be used to reveal trends and to determine the machine cost as a function of any parameter.

Without an optimisation tool, it is still possible to find the cost of a machine as a function of a few parameters, such as the current density, the active length, the slot depth and the magnet length. However, when it comes to machine properties that depend on a number of parameters, this is extremely difficult. The power factor is one such parameter. When an optimisation tool is available, one can perform a number of optimisation runs with increasing values of the constraint on the power factor. This allows one to find the cost of the generator as a function of the power factor.

If one objective is to search for the cost as a function of the generator speed, it is necessary to let the numbers of both poles and slots vary. If, for example, the number of poles is fixed for all generator speeds, then the results will be suboptimal. The highest-speed machine considered in this thesis can have a maximum of 22 poles (because of the frequency constraint). If the number of poles were also to be fixed at 22 for the lower-speed machines, then the generator cost would be many times higher than the global minimum.

The optimisation tool presented in this thesis is able to find the optimal machine designs as a function of every input parameter, including the generator speed. No similar results have been found in the literature.

The goal of this thesis is not to identify the very best electrical machine design. The analytical analysis used here is not sufficiently precise to do so, nor is the level of detail sufficiently rich. A future solution in which the analytical models are replaced with FEA models could perhaps achieve this purpose. Instead, the aims of this thesis are to identify trends and to illustrate how the design and cost of a PM machine vary with different parameters.

6.2 Gradient-based method

Although gradient-based methods suffer from some limitations, as discussed in the previous chapter, such a method can still be used to identify trends and relationships related to the optimal machine design. Because the optimal design can be found for each fixed number of base windings, it easy to illustrate how the various machine parameters vary with the number of poles. Using a gradient-based method, it is also possible to plot the minimum cost as a function of the power factor constraint, for example. A GA is much more time-consuming than a gradient-based algorithm, and repeated GA optimisation runs with small changes to one constraint would require a great deal of time and would probably not yield markedly different results from those of a gradient-based method.

This chapter reports the use of the gradient-based method *fmincon* implemented in MATLAB to optimise a reduced problem with only one integer-valued variable, as explained in Chapter 5.3.3.

If the problem were smooth and possessed no local minima in the feasible region, then a single run of *fmincon* would be sufficient to locate the global minimum. However, this is not the case for the problem considered here. Based on the result of the multistart test presented in Chapter 5.3.3, it is likely that a point with an objective value that is less than 1000 EUR above the global minimum can be found using a multistart method with a sufficient number of starting points.

6.2.1 Generator designs for a one-stage gear train

The number of magnet laminations is fixed at 10 in the reduced problem when a one-stage gear train is used, and the generator speed is 80 rpm.

Number of base windings

As explained in the previous chapter, the optimal number of base windings (and the optimal number of poles) is found using a basic grid search. For each number of base windings, 25 runs of a *MultiStart* procedure are performed. The minimum total cost as a function of the number of base windings is shown in Figure 6.1.

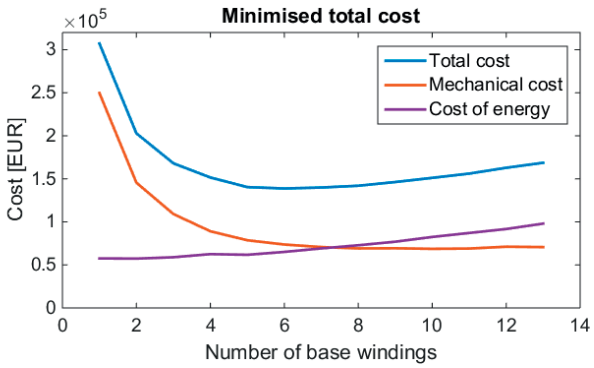

Figure 6.1: Minimum total cost as a function of n_{base} for a single-stage gear train

Table 6.1: Trends

Low numbers of poles	High numbers of poles
• High tooth flux density	• High outer diameter
• High stator yoke flux density	• High current density
• High end winding temperature	• High power factor
• High magnet temperature	
• Low short-circuit magnet flux density	

(The first column of Table 6.2 shows the optimal generator design for the reduced problem.) The best machine has 6 base windings, 132 poles and 144 slots, and the efficiency is 97.8%.

Figure 6.1 illustrates how the mechanical cost and the cost of energy vary with the number of base windings. Chapter 3.3 states that an increase in the number of poles typically leads to a lower machine cost but an increase in frequency-dependent losses. These two curves illustrate this tendency.

Based on the optimal machine designs for the different numbers of base windings, a few conclusions can be drawn. In machines with many poles, the optimal outer diameter, the optimal current density and the optimal power factor are all higher than in machines with few poles. In machines with few poles, the optimal tooth flux density, the optimal stator yoke flux density and the machine temperatures are higher than in machines with many poles. These trends are summarised in Table 6.1.

From Figure 6.1, it can be seen that in low-pole-number machines, the cost of energy is a smaller proportion of the total cost than in high-pole-number machines. Hence, the higher the price of energy is, the lower the optimal number of poles will be. Energy losses affect machines with high and low numbers of poles differently. In low-pole-number machines, the total energy loss is relatively low; however, they suffer from high end winding and magnet temperatures. In high-pole-number machines, the machine temperatures are not the limiting factors, although the total energy losses are higher.

It is worth noting that the flux density in the stator yoke is lower than the limiting value of 1.4 T. This is because of the energy loss in the stator yoke. With a thinner stator yoke, the mechanical cost would be lower, but the cost of the lost energy would be even higher. In many optimisation problems, the stator yoke flux density is fixed, as this reduces the number of variables by one. If the stator yoke flux density were fixed to 1.4 T in this problem and the stator yoke thickness were determined to obtain this value, then the resulting generator would have a higher total cost; thus, the result would be suboptimal.
Note that fixing the number of laminations to 10 may also cause the results to be suboptimal. The price of the magnets could be reduced by reducing the number of laminations.

Active constraints

It is interesting to investigate which constraints are active for an optimal solution. The active constraints are those that actively limit the optimum. By relaxing one of these constraints, it is possible to obtain a less expensive generator. When such a constraint is restricted, the solution space decreases and the optimal machine cost increases.
The active constraints for the machine presented in the first column of Table 6.2 are the constraints on the

- Maximum outer diameter
- Minimum power factor
- Maximum rotor yoke flux density
- Maximum tooth flux density

Hence, the constraints on the machine temperatures are not active for this design. The power losses of the machine are low because of the lost energy cost, not because of the constraints on the maximum temperatures.

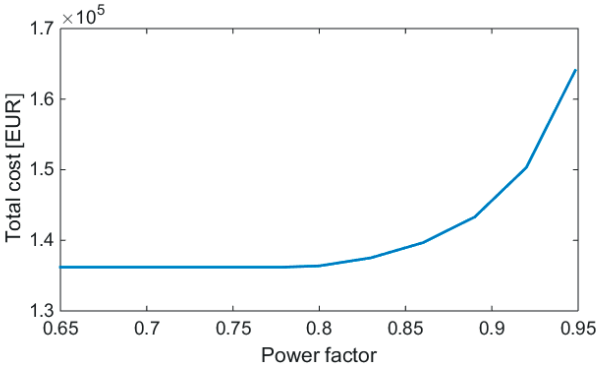

Figure 6.2: Cost as a function of the power factor

The constraint on the power factor is included for the sake of the power converter. A machine with single-layer concentrated windings often has a relatively high inductance because of the air gap leakage inductance, resulting in a low power factor. A low power factor leads to higher apparent power and higher power converter costs. However, it is possible that this higher converter cost can be compensated by a lower generator cost, or a higher generator cost due to a higher power factor may be compensated by a lower converter cost.
This possibility can be investigated by finding the generator cost as a function of the power factor. By running the optimisation for different values of the power factor constraint, a Pareto curve illustrating the total cost as a function of the power factor can be obtained; see Figure 6.2. A machine with a power factor of 0.92 is 11 300 EUR more expensive than a machine with a power factor of 0.85. This increase amounts to 15% of the cost of the active materials for the machine. If the converter cost is known as a function of the apparent power, then the optimal power factor can be chosen.

Active material cost as the objective

It is quite common in electrical machine design optimisation to minimise the cost of only the active materials, or the weight of the active materials. The most appropriate objective function depends on the application. In aerospace applications, the total weight of the system can be a reasonable objective function. For a seabed-mounted tidal turbine, it is reasonable to minimise the cost of the system combined with the cost of the lost energy.
Column two of Table 6.2 shows the optimal machine design when the optimisation objective is based on the mechanical cost alone. The resulting design is dramatically different from that represented in column one. The machine is longer and

Table 6.2: Optimised machine parameters

	Min. total machine cost	Min. mechanical machine cost
Lifetime cost	139 kEUR	179 kEUR
Active material cost	74 kEUR	63 kEUR
Lost energy cost	65 kEUR	116 kEUR
Variables		
R_{inner}	1.52 m	1.62 m
$d_{s,yoke}$	49 mm	15 mm
d_{slot}	54 mm	27 mm
w_{slot}	35 mm	29 mm
l_m	19 mm	12 mm
α_m	0.92	0.91
$d_{r,yoke}$	54 mm	21 mm
J	3.54 A/mm^2	6.93 A/mm^2
n_{base}	6	12
Machine parameters		
Outer diameter	3.5 m	3.5 m
Active length	310 mm	446 mm
Weight	6.29 tons	4.70 tons
Efficiency	97.8%	95.8%
Power factor	0.85	0.84
Number of poles	132	264
Number of slots	144	288
Magnet laminations	10	10
Magnet sc flux density	-0.02 T	0.45
Stator yoke flux density	1.22 T	1.40
Rotor yoke flux density	1.20 T	1.20
Tooth flux density	1.60 T	1.40
End winding temperature	109 °C	135 °C
Magnet temperature	82 °C	83 °C

slimmer, and it has a higher current density. The numbers of slots and poles are doubled, and the efficiency is reduced from 97.7% to 95.8%.
The cost of the active materials is 15% lower for the machine optimised for the minimum mechanical cost. At first glance, this might seem like a better generator. The efficiency is fairly high, although lower than that of the machine optimised for the minimum total cost. However, the lost energy cost is almost twice as high as the mechanical cost. This results in a total cost that is 28% higher than that for the machine with the minimum total cost. This illustrates how important it is to optimise for the correct target.

The active constraints for the optimal minimum-active-cost machine are those on the

- Maximum outer diameter
- Minimum power factor
- Maximum rotor yoke flux density
- Maximum stator yoke flux density
- Maximum winding temperature

When the lost energy cost is not included in the objective function, the winding temperature and the stator yoke flux density increase to their upper limits.

6.2.2 Direct-drive generator designs

The power train of a tidal turbine may or may not include gears. A gearless solution will require a larger and more expensive generator. Gear losses are eliminated, at the expense of higher generator losses. The reliability of the power train will improve in the absence of gears; however, the reliability of the generator and the bearings may be lower in a gearless system than in a geared system. The lower speed of the generator leads to lower frequency-dependent losses. Therefore, the number of magnet laminations is set to 2, as opposed to 10 in the one-stage case.
In the previous section, the number of base windings was restricted to a maximum of 13 by the maximum allowed frequency. When the generator speed is only 15 rpm, the number of base windings can be as high as 36. However, it is not possible to find a feasible solution with such a high number of poles. Feasible solutions have been found for designs with 3 to 22 base windings.

Figure 6.3 shows the cost of the generator as a function of the number of base windings. It can be seen that the optimal number of base windings is 7 for a direct-

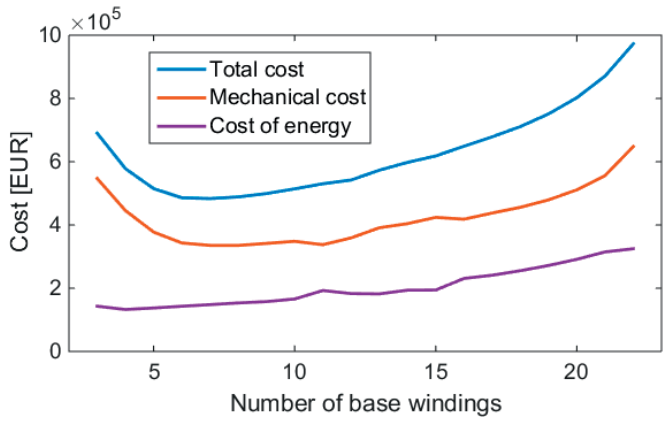

Figure 6.3: Total cost as a function of n_{base} for a direct drive

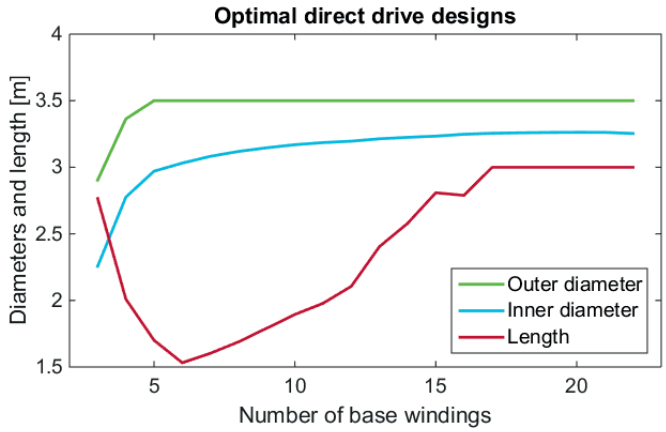

Figure 6.4: Optimal diameter and length values as functions of n_{base}

drive generator. Both the mechanical cost and the energy cost increase when the number of base windings is greater than n_{base}=8. The maximum length is an active constraint for machines with more than 16 base windings. This causes a fairly rapid increase in the mechanical cost at high numbers of base windings.

Based on the optimal generator designs for the various numbers of base windings, the following trends can be seen: The optimal current density increases with an increasing number of base windings. The magnet temperature decreases with an increasing number of poles.
The optimal outer diameter increases with an increasing number of base windings. For n_{base} higher than 4, the optimal outer diameter is at its limit of 3.5 m. This is illustrated in Figure 6.4. The figure also shows that the optimal active length

Table 6.3: Optimal generator designs

	Nom. speed 15 rpm	Nom. speed 80 rpm	Nom. speed 360 rpm
Lifetime cost	483 kEUR	139 kEUR	93 kEUR
Active material cost	335 kEUR	74 kEUR	45 kEUR
Lost energy cost	148 kEUR	65 kEUR	49 kEUR
Variables			
R_{inner}	1.54 m	1.52 m	1.01 m
$d_{s,yoke}$	34 mm	49 mm	85 mm
d_{slot}	57 mm	54 mm	43 mm
w_{slot}	31 mm	35 mm	44 mm
l_m	20 mm	19 mm	27 mm
α_m	0.92	0.92	0.54
$d_{r,yoke}$	43 mm	54 mm	49 mm
J [A/mm^2]	3.39	3.54	3.49
n_{base}	7	6	3
Machine parameters			
Outer diameter	3.5 m	3.5 m	2.54 m
Active length	1.60 m	0.31 m	0.29 m
Weight	25.4 tons	6.29 tons	4.69 tons
Efficiency	94.0%	97.8%	98.4%
Power factor	0.85	0.85	0.85
Number of poles	154	132	66
Number of slots	168	144	72
Magnet laminations	2	10	10
Magnet sc flux density	0.49 T	-0.02 T	0.17 T
Stator yoke flux density	1.4 T	1.22	0.68 T
Rotor yoke flux density	1.2 T	1.2 T	1.2 T
Tooth flux density	1.6 T	1.6 T	1.10 T
End winding temperature	91 °C	109 °C	123 °C
Magnet temperature	73 °C	82 °C	90 °C

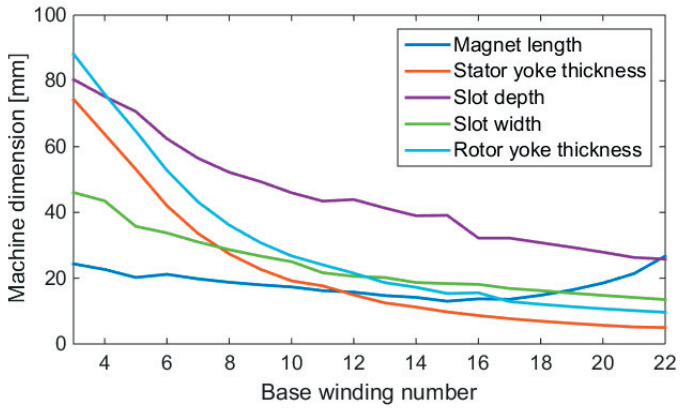

Figure 6.5: Optimal machine dimensions as functions of n_{base}

decreases with an increasing number of base windings as long as the outer diameter is increasing. When the outer diameter reaches its upper limit, the length continues to increase with the number of base windings until its upper limit of 3 m is reached. Figure 6.5 shows the optimal machine dimensions for the different numbers of base windings. The yoke thicknesses and the slot width are expected to decrease with an increasing number of poles because the pole width decreases. The optimal magnet length also varies with the number of base windings. For high and low numbers of base windings, the optimal magnet length is greater than 20 mm, whereas the optimal magnet length is only 13 mm when n_{base} is 15.

The active constraints for the optimal direct-drive generator design are those on the

- Maximum outer diameter
- Minimum power factor
- Maximum flux densities in the teeth and in the rotor and stator yokes

6.2.3 Generator designs for a two-stage gear train

A turbine with a two-stage gear train requires a generator with a higher speed and a lower torque than one with a one-stage gear train does. The generator cost is reduced, the cost for the gears is increased, and the reliability of the gear is reduced. A generator speed of 360 rpm is considered for the case of a two-stage gear train. At this high rotational speed, frequency-induced losses are high; therefore, the

number of magnet laminations is set to 10. Because of the electrical frequency limit of 200 Hz, the maximum allowable number of base windings is only 3.

The best generator design in this case has three base windings, and the details are presented in Table 6.3 together with the optimal designs for the direct-drive generator and the generator with the one-stage gear train.
The total cost of the high-speed generator is 67% of that of the medium-speed generator. The cost of the medium-speed generator is 29% of that of the low-speed generator. The table illustrates that the material cost decreases with increasing speed to a greater extent than the lost energy cost does. For a complete understanding of the optimal choice of gearing, it is necessary to evaluate the gear cost, the gear losses and the reliability of both the generator and the gear(s). Additional comparisons among generator designs for various gear ratios will follow in the next section.

The active constraints for the optimal generator with a two-stage gear train are those on the

- Maximum electrical frequency
- Minimum power factor
- Maximum flux density in the rotor yoke
- Maximum magnet temperature

The constraint on the magnet temperature has an especially marked effect on the final design. If the winding layout produced lower spatial flux subharmonics, the induced eddy-current losses in the magnets would be smaller, and the optimal generator design would be different.

6.2.4 Conclusions from the gradient-based optimisation

This subchapter has shown how a gradient-based optimisation algorithm can be used to investigate various aspects of generator design. The *fmincon* solver is fast and efficient; however, the need for a multistart solver and a grid search results in a fairly long total optimisation time.
The method produces a large number of results, enabling the investigation of various machine parameters as functions of the number of base windings. This provides knowledge regarding the choice of the number of poles. It has been shown that in the case of a one-stage gear train, the optimal number of base windings is a trade-off between the conflicting objectives of minimising the mechanical cost

and minimising the cost of lost energy. When the mechanical cost alone is the objective, the optimal number of poles is twice as large as when the total cost is the objective. Consequently, if the expected energy price increases, the optimum number of poles decreases, and vice versa.
By optimising the generator with respect to two different objectives, namely, total cost and mechanical cost, it has been shown that the resulting generator designs differ and that the difference in the total cost is 40 000 EUR.
Moreover, it has been shown that the total cost is influenced by the values of the active constraints. The power factor of the generator in the case of a one-stage gear train can be increased from 0.85 to 0.92 at an expense of 11 300 EUR, which amounts to 15% of the cost of the active materials. The Pareto curve that shows the cost as a function of the power factor can be used to determine the optimal power factor and the required power converter rating.

Optimal generator designs have also been found for the cases of direct-drive and two-stage gear train solutions. For the direct-drive generator, the mechanical cost dominates. The minimum total cost is achieved when the number of base windings is 7.
The cost of the generator designed for a two-stage gear train is dominated by high frequency-dependent losses, which result in high magnet temperatures. The resulting design involves relatively narrow magnets (small magnet segments), thick PMs (resulting in a large effective air gap, which reduces the eddy-current losses) and low flux densities in the teeth and the stator yoke.
The high-speed generator is the lightest and least expensive generator, and it has the highest efficiency. This comes at the expense of the cost of a gear train with a large gear ratio, increased losses in the gear train and reduced reliability of the gear train. The total cost of the medium-speed generator is 29% of that of the low-speed generator, and the cost of the high-speed generator is 67% of that of the medium-speed machine.

6.3 Hybrid method

In the hybrid optimisations, the full problem is solved, with four integer-valued variables. The number of poles, the number of slots and the number of winding layers are allowed to vary freely within the boundaries specified in Chapter 5.4.3. The short-pitch factor can be higher than one only for double-layer windings and if the slot-and-pole combination results in a distributed winding with a winding pitch greater than one.

R_{inner}	$d_{s,yoke}$	d_{slot}	w_{slot}	l_m	α_m	$d_{r,yoke}$	J	$Q_p/2$	p	N_{layer}	y_{sp}
1.48	0.0427	0.0773	0.0381	0.0123	0.945	0.0377	3.16	**21**	**56**	**2**	**0**
1.47	0.0523	0.0753	0.0411	0.0168	0.916	0.0451	3.22	**18**	**48**	**2**	**0**
1.48	0.0417	0.0765	0.0354	0.0155	0.890	0.0331	3.28	**22**	**55**	**2**	**0**
1.48	0.0472	0.0718	0.0352	0.0140	0.891	0.0325	3.35	**22**	**55**	**2**	**0**
1.48	0.0472	0.0760	0.0364	0.0152	0.884	0.0419	3.35	**20**	**50**	**2**	**0**
1.48	0.0471	0.0760	0.0364	0.0152	0.884	0.0420	3.36	**20**	**50**	**2**	**0**
1.43	0.0509	0.0716	0.0404	0.0145	0.902	0.0440	3.22	**20**	**50**	**2**	**0**
1.48	0.0471	0.0760	0.0364	0.0152	0.884	0.0421	3.36	**20**	**50**	**2**	**0**
1.50	0.0532	0.0743	0.0400	0.0170	0.915	0.0435	3.27	**18**	**48**	**2**	**0**
1.49	0.0498	0.0718	0.0359	0.0143	0.889	0.0329	3.37	**22**	**55**	**2**	**0**
1.48	0.0470	0.0761	0.0363	0.0153	0.884	0.0420	3.35	**20**	**50**	**2**	**0**
1.46	0.0502	0.0713	0.0354	0.0139	0.890	0.0332	3.40	**22**	**55**	**2**	**0**
1.46	0.0502	0.0713	0.0354	0.0139	0.890	0.0332	3.40	**22**	**55**	**2**	**0**
1.46	0.0502	0.0713	0.0354	0.0139	0.890	0.0332	3.40	**22**	**55**	**2**	**0**
1.46	0.0502	0.0713	0.0354	0.0139	0.890	0.0332	3.40	**22**	**55**	**2**	**0**
1.46	0.0502	0.0713	0.0354	0.0139	0.890	0.0332	3.40	**22**	**55**	**2**	**0**
1.46	0.0502	0.0713	0.0354	0.0139	0.890	0.0332	3.40	**22**	**55**	**2**	**0**
1.45	0.0506	0.0719	0.0349	0.0140	0.891	0.0333	3.42	**22**	**55**	**2**	**0**
1.48	0.0345	0.0761	0.0356	0.0155	0.883	0.0333	3.20	**22**	**55**	**2**	**0**
1.48	0.0346	0.0760	0.0355	0.0155	0.883	0.0334	3.21	**22**	**55**	**2**	**0**
1.49	0.0437	0.0769	0.0380	0.0151	0.878	0.0442	3.06	**20**	**50**	**2**	**0**
1.47	0.0409	0.0737	0.0383	0.0164	0.876	0.0369	3.12	**22**	**55**	**2**	**0**
1.48	0.0345	0.0761	0.0354	0.0155	0.883	0.0336	3.212	**22**	**55**	**2**	**0**
1.47	0.0303	0.0725	0.0387	0.0172	0.877	0.0287	3.23	**22**	**55**	**2**	**0**
1.43	0.0462	0.0752	0.0366	0.0149	0.884	0.0473	3.36	**20**	**50**	**2**	**0**
1.56	0.0414	0.0587	0.0354	0.0204	0.894	0.0301	2.91	**29**	**71**	**2**	**0**
1.39	0.0648	0.0544	0.0321	0.0203	0.894	0.0291	2.32	**19**	**75**	**2**	**0**
1.42	0.0406	0.0611	0.0304	0.0188	0.914	0.411	3.07	**21**	**57**	**2**	**0**
1.35	0.0439	0.0609	0.0441	0.0189	0.870	0.0235	3.20	**20**	**64**	**2**	**0**
1.52	0.0394	0.0514	0.0300	0.0208	0.889	0.0421	2.81	**23**	**73**	**2**	**0**

Figure 6.6: The 30 best individuals in the final GA population

6.3.1 Generator designs for a one-stage gear train

First, a thorough analysis of the optimal design for a generator with a one-stage gear train is performed. The rotational speed of the generator is 80 rpm.

Genetic and hybrid algorithms

The problem is first solved using a genetic algorithm. The 30 best individuals from the final population are listed in Figure 6.6. All of them have windings of the concentrated double-layer type. The best cost found is 134 074 EUR.
The second stage of the optimisation procedure is the gradient-based algorithm. Together, the GA and the *fmincon* algorithm constitute a hybrid algorithm. Some of the best individuals from the final population generated by the GA are selected as starting points for the iterative solver (see Figure 6.7), for which the integer-valued variables are fixed. The best cost found using the hybrid algorithm is 131 769 EUR.

R_{inner}	$d_{s,yoke}$	d_{slot}	w_{slot}	l_m	α_m	$d_{r,yoke}$	J	$Q_p/2$	p	N_{layer}	Y_{sp}
1.48	0.0427	0.0773	0.0381	0.0123	0.945	0.0377	3.16	**21**	**56**	**2**	**0**
1.47	0.0523	0.0753	0.0411	0.0168	0.916	0.0451	3.22	**18**	**48**	**2**	**0**
1.48	0.0417	0.0765	0.0354	0.0155	0.890	0.0331	3.28	**22**	**55**	**2**	**0**
1.48	0.0472	0.0760	0.0364	0.0152	0.884	0.0419	3.35	**20**	**50**	**2**	**0**
1.56	0.0414	0.0587	0.0354	0.0204	0.894	0.0301	2.91	**29**	**71**	**2**	**0**
1.39	0.0648	0.0544	0.0321	0.0203	0.894	0.0291	2.32	**19**	**75**	**2**	**0**
1.42	0.0406	0.0611	0.0304	0.0188	0.914	0.411	3.07	**21**	**57**	**2**	**0**
1.35	0.0439	0.0609	0.0441	0.0189	0.870	0.0235	3.20	**20**	**64**	**2**	**0**
1.52	0.0394	0.0514	0.0300	0.0208	0.889	0.0421	2.81	**23**	**73**	**2**	**0**

Figure 6.7: Individuals selected as starting points for the iterative algorithm

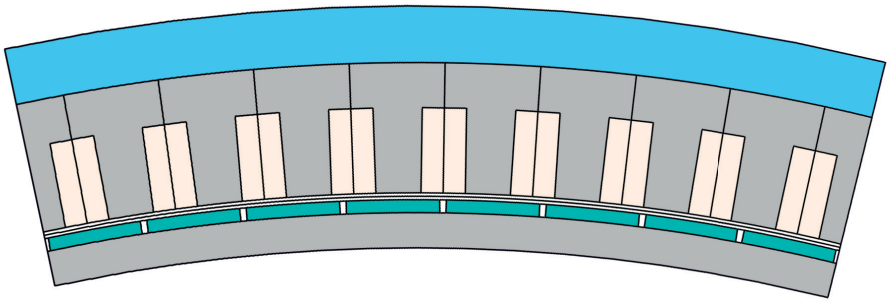

Figure 6.8: Optimal machine design for a speed of 80 rpm

The optimal machine designs found using the GA and the hybrid algorithm are shown in Table 6.4. The optimal number of slots per pole and phase is 3/8, which results in a machine with 14 base windings, each containing 8 poles and 9 slots. One 14^{th} of the machine is illustrated in Figure 6.8.

The result of the hybrid algorithm is slightly better than that of the pure GA; the cost is 2% lower. The improvement is primarily achieved by increasing the outer diameter to its maximum limit and reducing the yoke thicknesses.

The loss distribution of the optimal machine is illustrated in Figure 6.9. The copper losses dominate above 50 rpm, and the magnet losses are negligible. The resulting efficiency lies between 96% and 98% throughout most of the operational range, and at the rated operation point, the efficiency is 97.6%.

Sensitivity

Outer diameter

The total cost of the generator is more sensitive to some parameters and constraints than to others. The maximum outer diameter is an active constraint, and the sensitivity to this constraint is found at the point where D_{outer} is 3.5 m.

Table 6.4: Optimal generator designs (full problem)

	Genetic algorithm	Hybrid algorithm
Lifetime cost	134 kEUR	132 kEUR
Active material cost	68 kEUR	65 kEUR
Lost energy cost	66 kEUR	66 kEUR
Variables		
p	56	56
$Q_p/2$	21	21
N_{layer}	2	2
y_{sp}	0	0
R_{inner}	1.48 m	1.54 m
$d_{s,yoke}$	43 mm	40 mm
d_{slot}	77 mm	75 mm
w_{slot}	38 mm	39 mm
l_m	12 mm	12 mm
α_m	0.94	0.93
$d_{r,yoke}$	38 mm	31 mm
J	3.16 A/mm^2	3.22 A/mm^2
Machine parameters		
Outer diameter	3.41 m	3.5 m
Active length	321 mm	446 mm
Weight	6.05 tons	5.76 tons
Efficiency	97.7%	97.6%
Power factor	0.87	0.87
Number of poles	112	112
Number of slots	126	126
q	3/8	3/8
Magnet laminations	9	9
Magnet sc flux density	0.44 T	0.43
Stator yoke flux density	0.77 T	0.84
Rotor yoke flux density	0.98 T	1.20
Tooth flux density	1.33 T	1.46
End winding temperature	113 °C	115 °C
Magnet temperature	89 °C	90 °C

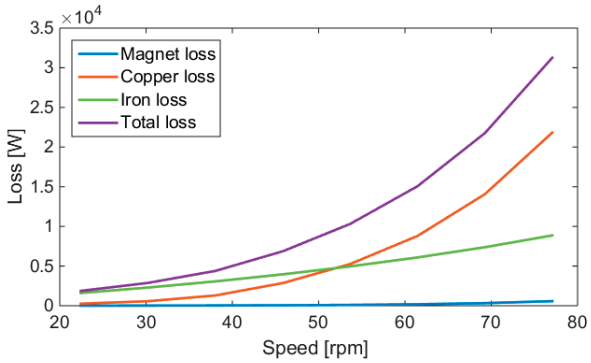

Figure 6.9: Losses as functions of speed in the optimal 80 rpm machine

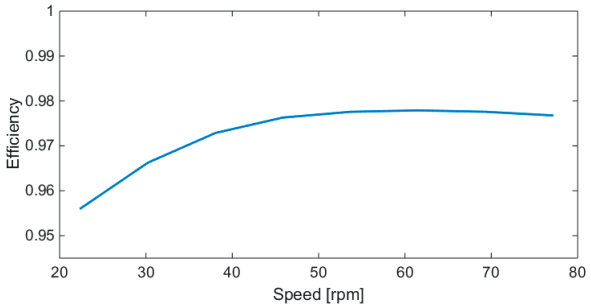

Figure 6.10: Efficiency as a function of speed in the optimal 80 rpm machine

To find the sensitivity, gradient-based optimisations are run with p, $Q_p/2$, N_{layer} and y_{sp} fixed and with a slight increase and a slight decrease in the constraint on the outer diameter.
Reducing or increasing the outer diameter results in a change in the cost of approximately 9 000 EUR/m. This means that by increasing the outer diameter by 10 cm, the cost can be reduced by roughly 900 EUR.

Power factor
The power factor of the optimised machine is 0.863. This is above the lower limit, which means that 0.863 is the optimal power factor, regardless of the imposed constraint. It is possible to increase the power factor at the expense of an increased generator cost.
The sensitivity of the cost to the power factor *at this point* is approximately 12 700 EUR/unit power factor. Consequently, an increase from 0.863 to 0.873 would cause the total cost to increase by 127 EUR.

Energy price and PM price
The results of the optimisation are a direct consequence of all input parameters. However, the values of some of these parameters are highly uncertain. If more updated estimates of the values of one or more parameters are obtained, then a newly updated optimisation can be performed, which might alter the outcome of the optimisation.
The price of energy and the price of the PM material are two of the most uncertain parameters in the analysis. The future price of energy is unreliable and strongly depends on political decisions. The prices of the rare-earth metals that are used in PMs have been fluctuating over the last few years, and the availability of these materials is also a matter of uncertainty that is subject to global political strategies. Therefore, it is meaningful to investigate how the optimal design and cost are affected when the estimates of the price of energy and the price of magnets are either doubled or halved. These different cases are compared with the base case, in which the energy price is 0.24 EUR/kWh and the cost of the PM material is 85 EUR/kg.

Table 6.5 lists the various machine parameters for the optimal generator designs obtained with the different energy prices as inputs. The higher the energy price is, the lower the current density is, and the thicker the magnets are. The optimal number of poles decreases when the estimated energy price is doubled. The cost of energy, the material cost and the total cost are shown in Figure 6.11 as functions of the input energy price (in blue).
Although the cost of lost energy is 100% higher in the third case than in the base case, the energy cost is not 100% higher. The optimisation tool finds a different design that has lower losses but a higher material cost. Thus, the total cost becomes 44% higher than in the base case.

Table 6.6 lists the generator parameters for the optimal machine designs for the different PM prices. When the price of the PM material is doubled, the cost of the optimal machine increases by 17%. When the PM price is halved, the total cost is reduced by 11%. The optimal numbers of poles and the optimal winding distributions are different for all three machines. The magnet length is 19 mm in the case of the low PM price, 12 mm in the case of the medium PM price and 10 mm in the case of the high PM price. The cost elasticity of the machines is also illustrated in Figure 6.11. The cost elasticity with respect to the energy price is plotted in blue, with triangular markers. The cost elasticity with respect to the PM price is plotted in red, with circular markers. The same reduction or increase in either price leads to the same mechanical cost; however, the different energy prices lead to much larger variations in the cost of energy than do the different PM

Table 6.5: Optimal 80 rpm machines with varying energy prices

Energy price [EUR/kWh]	0.12	0.24	0.48
Speed [rpm]	80	80	80
Winding type	FSCW	FSCW	FSCW
Number of winding layers	2	2	2
Number of poles	112	112	94
q	3/8	3/8	14/47
Total cost [kEUR]	97.1	131.8	190.0
Mechanical cost [kEUR]	60.6	65.3	88.3
Energy cost [kEUR]	36.5	66.5	101.7
Weight [tons]	5.46	5.76	8.07
Efficiency [%]	97.4	97.7	98.3
Current density [A/mm^2]	3.63	3.22	2.41
End winding temp. [°C]	126	115	98
Magnet temp. [°C]	90	90	82
Magnet length	10	12	18
Magnet segmentation	10	9	8

prices.
The results presented in Tables 6.5 and 6.6 illustrate that the optimal machine design strongly depends on the input parameters of the analytical model.

Winding layers
The optimal number of winding layers is 2, although double-layer windings have lower fill factors and twice as many coils as single-layer windings. A machine with the same numbers of slots and poles but with single-layer windings instead of double-layer windings would have

- A higher fill factor
- A higher subharmonic flux content
- Higher leakage inductance and a lower power factor
- A higher on-load flux density and more saturated yokes
- Higher iron loss
- Higher magnet loss and higher magnet temperatures

Table 6.6: Optimal 80 rpm machines with varying PM prices

PM price [EUR/kg]	42.5	85	170
Speed [rpm]	80	80	80
Winding type	FSCW	FSCW	FSCW
Number of winding layers	2	2	2
Number of poles	106	112	90
q	16/53	3/8	2/5
Total cost [kEUR]	117.6	131.8	153.8
Mechanical cost [kEUR]	60.6	65.3	89.5
Cost of energy [kEUR]	57.1	66.5	64.3
Weight [tons]	6.40	5.76	6.40
Magnet weight [kg]	387	256	239
Efficiency [%]	98.0	97.7	97.7
Current density [A/mm^2]	2.83	3.22	2.97
End winding temp. [°C]	114	115	116
Magnet temp. [°C]	86	90	90
Magnet length	19	12	10
Magnet segmentation	9	9	10

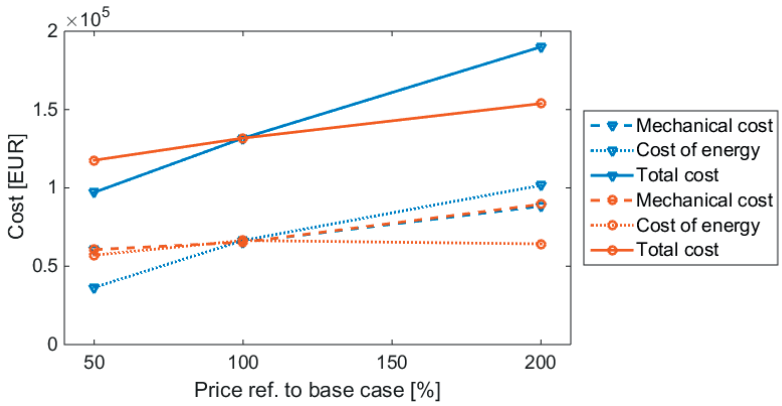

Figure 6.11: Cost elasticity with respect to the energy price (blue) and the PM price (red)

Therefore, the optimal machine with 112 poles and 126 slots and single-layer windings has thicker yokes, the slots are less deep, and the magnets are thicker and narrower. The total cost of the generator is 137 kEUR. Because of the higher armature reaction, the magnet short-circuit flux density is -0.2 T.

6.3.2 Various gear ratios

For a turbine speed of 15 rpm, a one-stage gear train typically yields a generator speed of 80 rpm. A two-stage gear train typically yields a generator speed of 360 rpm, whereas a three-stage gear train yields a generator speed of 1050 rpm.

One hypothesis made at the beginning of this study was that the optimal winding type would change with the rated speed of the machine. FSCW machines are known to have properties that are very beneficial for low-speed, high-torque machines that require high efficiencies. DW machines have other properties, such as low PM losses, that are especially beneficial for higher-speed machines.

Prior to the optimisation, it was thought that the concentrated design would be optimal for machines with the lower gear ratio and that the distributed design would be optimal for machines with the higher gear ratio.
However, the optimisation results indicate that the double-layer FSCW layout is optimal for all six cases investigated. Table 6.7 lists the key machine parameters of the optimal machines for the various gear ratios.

High-speed generator designs

A closer study of generators with a rated speed of 1050 rpm shows that it is possible to manufacture machines with both FSCW and DW layouts at comparable costs. The parameters for the optimal machines with DWs and FSCWs are shown in Table 6.8. The distributed winding machine is only 1% more expensive than the concentrated winding machine. Notice that the DW machine is an integer-slot machine with 1 slot per pole and phase and that it has a single-layer winding design.
DW machines may also be suitable for the second highest speed, 360 rpm. The cost of the optimal DW machine is compared with that of the optimal FSCW machine in Table 6.9. The DW machine is 19% more expensive than the FSCW machine.
The factor that makes the greatest contribution to the difference between the costs of the DW and FSCW machines is the size of the end windings. The longer end windings of DW machines lead to a higher conductor cost, a higher cost for producing the windings, and a higher cost of energy due to higher copper losses.
The end winding lengths are modelled rather roughly in this work. The axial length of the end windings in a DW machine is fixed regardless of the winding dimen-

Table 6.7: Optimal machine parameters for various gear ratios

Gear ratio	1:1	1:2	1:5.33	1:10.66	1:24	1:70
Speed [rpm]	15	30	80	160	360	1050
Torque [kNm]	955	477	179	90	40	14
Winding type	FSCW	FSCW	FSCW	FSCW	FSCW	FSCW
Number of winding layers	2	2	2	2	2	2
q	2/5	3/8	3/8	11/35	9/31	11/36
Total cost [kEUR]	409.6	238.4	131.8	104.7	80.1	64.8
Mechanical cost [kEUR]	255.9	139.9	65.3	55.7	38.1	29.7
Cost of energy [kEUR]	153.7	98.5	66.5	49.0	42.0	35.1
Weight [tons]	18.9	11.9	5.76	5.67	4.23	3.60
Efficiency [%]	93.7	96.1	97.7	98.3	98.7	98.9
Power factor	0.85	0.85	0.87	0.85	0.85	0.85
Current density [A/mm^2]	3.27	3.12	3.22	2.84	3.17	2.87
End winding temp. [$^\circ$C]	116	117	115	117	121	135
Magnet temp. [$^\circ$C]	80	84	90	90	90	90
Magnet segmentation	4	6	9	9	10	16

Table 6.8: High-speed machines with FSCW and DW designs

	Speed	Total cost	Efficiency	Number of poles	q	Layers
DW	1050 rpm	65 700 EUR	98.8%	22	1	1
FSCW	1050 rpm	64 800 EUR	98.9%	22	11/36	2

sions or the coil throw. It is possible that a more detailed model of the end winding topology could alter the results somewhat, potentially allowing the DW designs to become more competitive.
It is also important to note that the FEA verification presented in Chapter 4.11 showed that in the case of FSCW machines, the analytical analysis overestimates the magnetic field produced by the magnets. Hence, this analysis may underestimate the costs of FSCW machines.

To conclude, it seems that the transition between optimal FSCW and DW layouts lies in the speed range near 1000 rpm. For speeds below 1000 rpm, FSCWs are more suitable, whereas for higher speeds, DWs might be preferable. These findings are, of course, limited to the particular application considere here, with the specified constraints and assumptions.

Table 6.9: Medium-speed machines with FSCW and DW designs

	Speed	Total cost	Efficiency	Number of poles	q	Layers
DW	360 rpm	95 500 EUR	98.3%	44	15/22	2
FSCW	360 rpm	80 100 EUR	98.7%	62	9/31	2

How the designs vary with the gear ratio

Figure 6.12 shows how the cost of the active materials, the cost of energy and the total cost decrease as the rated speed increases (note that the x axis is logarithmic). This is expected, as, in theory, the size of the machine should be approximately proportional to the torque. The cost reduction gained by switching from a direct drive to a one-stage gear train (from 15 rpm to 80 rpm) is as high as 277 900 EUR, which is a reduction of 68%.
The cost of a generator with a two-stage gear train (360 rpm) is 51 700 EUR (31%) less than that of a generator with a one-stage gear train.
The cost difference between the optimal generator designs for a three-stage gear train (1050 rpm) and a two-stage gear train (360 rpm) is 15 300 EUR (20% reduction).

The owner of the tidal power system should consider the total generator cost, the gear cost, the lifetime cost of the energy lost in the gear(s), and both the gear reliability and the generator reliability when determining the gear ratio for the power train. The optimisation tool presented here makes this task easier because it allows the optimal generators to be identified for various speeds. The choice of gears also affects the dynamic torque experienced by the propeller. The stress on the turbine blades depends on the system inertia. This was illustrated by Matveev and the author in [126]: "Low system inertia 'seen by the propeller' will be an advantage as it lets the generator 'give a slack' - to absorb the 'hit' by letting the propeller accelerate a bit and then bring it back to the right speed." A high gear ratio increases the inertia and results in a stiffer drive train with higher stress on the turbine blades.

Figure 6.13 illustrates how the main dimensions of the generators vary with speed. Below 100 rpm, the outer diameter is limited to its maximum value of 3.5 m. Above this speed, the outer diameter decreases as the generator speed increases. The optimal thickness of the generator remains approximately the same for all speeds. The reason for this may be that the same cooling is applied in all cases.
When the outer diameter is at its limit, the active length decreases with increasing speed. However, at higher speeds, when the outer diameter is no longer dictated by

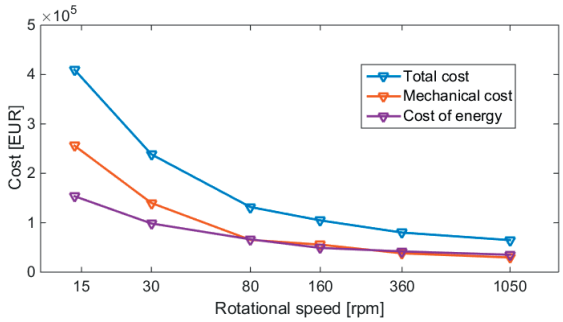

Figure 6.12: Costs versus speed

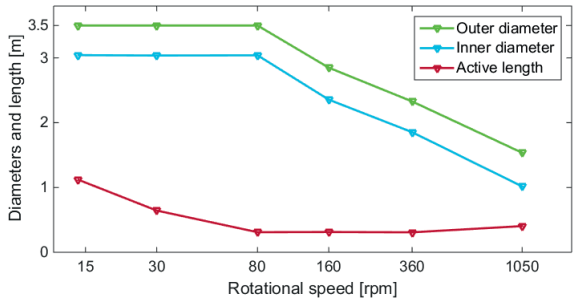

Figure 6.13: Main dimensions versus speed

its constraint, the optimal length remains fairly constant and even increases slightly for higher-speed machines.

Low-speed machines must produce higher torques than high-speed machines for the same rated power. Torque production requires current and space, and higher currents and larger machines produce higher losses. Figure 6.14 shows how the efficiency increases with an increasing generator speed. The direct-drive machine has a rated efficiency of 93.7%, whereas the highest-speed machine has a rated efficiency of 98.9%.
An estimate of the gear efficiency provides an approximation of the total efficiency of the drive train (excluding the power converter). Note that the frictional losses of the generator are not included. These frictional losses will depend on the size, weight and speed of the generator. The red line in Figure 6.14 represents the combined efficiency of the generator and the gear train. It can be seen that the highest total efficiency is achieved with a two-stage gear train.

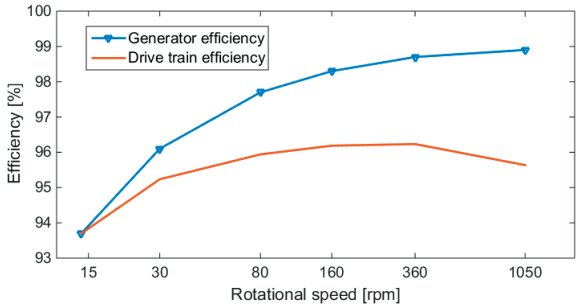

Figure 6.14: Efficiency as a function of speed

6.3.3 Conclusions from the hybrid optimisation

The results of the hybrid optimisation show that double-layer FSCW machines offer the lowest turbine generator costs for the speeds investigated (up to 1050 rpm). In a generator equipped with a three-stage gear train, either FSCWs or DWs can be used at comparable costs.

For the 80 rpm case, a single-layer FSCW machine has a higher cost because the winding MMF produces higher subharmonics, which induce higher on-load fluxes in the yokes and teeth and higher losses in the iron and the magnets.

The price of the generator decreases with an increasing gear ratio, as expected. The reduction is most significant at the transition from a direct drive to a one-stage gear train. The curve showing the cost as a function of the generator speed can help guide the system owner in selecting the drive-train topology. Based on gear efficiency estimates, it is found that the highest efficiency can be achieved with a two-stage gear train.

It has been demonstrated how the optimal design depends on the input parameters. The optimal design changes when either the energy price or the price of the PM material is doubled or halved. The sensitivities to the outer diameter constraint and the power factor have been quantified.

Chapter 7

Conclusions

A large amount of energy can be harvested from marine currents around the world. Of the different types of marine currents, tidal currents have the highest potential, and almost 6% of the UK's total electricity consumption can already be generated from tidal power using *existing* technology. The tidal energy sector is currently in a stage characterised by extensive development. The first commercial arrays of turbines will likely be connected to the grid this year, 2016.
The first contribution of this thesis is a review of different tidal turbine concepts. The results show that horizontal-axis turbines, which resemble wind turbines, are in a majority. Permanent magnet generators and induction generators are currently the two preferred generator technologies. For direct-drive systems, permanent magnet machines are applied. For geared machines, both types are used. Most tidal turbines are geared. Few specifications can be found regarding the gear types, but both two- and three-stage gear trains have been identified.
The greatest challenges facing the tidal energy industry are the high costs of the devices and the difficulty of their maintenance. To produce electricity in a cost-effective manner, the industry must develop maintenance-free, high-reliability components for all parts of the energy conversion system, from cables and converters to gears and generators.
The technology review has yielded a set of generator specifications: a 1,5 MW turbine with a nominal speed of 15 rpm and a 3,3 kV voltage rating. The nominal speed of the generator may range from 15 rpm to 1000 rpm.

The chosen generator topology is a radial-flux machine with an inner rotor and surface-mounted magnets. The stator is slotted, and the stator and rotor yokes are made of laminated steel. The generator is a three-phase machine with the current

placed in the q-axis, and it has internal passive air cooling. The machine may have either distributed windings or concentrated windings.
Constraints are imposed on various parameters to prevent a machine design that cannot be manufactured in practice or will lead to unnecessary costs in other parts of the tidal energy system. The maximum outer diameter and active length are 3.5 m and 3 m, respectively. To keep the converter costs down, the electrical frequency must be below 200 Hz, and the power factor must be no less than 0.85. The maximum allowed hot-spot temperature at full load is $135\,^{\circ}\mathrm{C}$, and the magnet temperature should be no higher than $90\,^{\circ}\mathrm{C}$ because of the risk of demagnetisation. The same demagnetisation risk dictates that the flux density in the magnets under short-circuit conditions must be above -0.2 T. The maximum flux densities in the teeth, the stator yoke and the rotor yoke must be no more than 1.6 T, 1.4 T and 1.2 T, respectively.

Once a set of input variables has been defined, an electrical machine analysis can be performed. A novel feature of the proposed analysis approach is that it can consider various winding types. For a given input, including the number of slots, the number of poles and the number of winding layers, an appropriate winding layout is found, and a magnetic analysis, an electrical analysis, a loss analysis and a thermal analysis are performed. The result of the analysis is a set of key machine parameters specific to the specified machine design. The outputs are the objective value (fitness) of the machine design and a vector containing the values of all parameters that are subject to constraints.

In the analytical analysis of PM machines, it is common to calculate the flux densities in the teeth and yokes only in the no-load case. It has been shown here that the armature reaction flux should also be considered, especially when the current loading is high.
One of the major contributions of this thesis is the description of the stator yoke flux patterns in fractional-slot machines, together with a simple method for calculating these fluxes. It has been shown that the flux amplitudes in the stator yoke are not the same behind every slot of the stator. In a fractional-slot machine, the winding layout may cause the flux amplitude produced by the armature reaction to be distributed unevenly. An even larger variation can be observed under load, when the permanent magnet flux and the armature reaction flux are *combined*. The phase shift between the PM flux and the armature reaction flux varies from slot to slot. It has been shown that in one of the investigated machines, the on-load flux behind one slot is 10 times higher than that behind another slot. The largest variations are found in machines with winding layouts that produce magnetic fields with a high subharmonic content.
With the correct information about the fluxes in the machine, one can choose the

thickness of the yokes such that saturation is avoided. The designer can also place the holes for bolts or for cooling in positions that are less saturated. It is also possible to deliberately allow the yoke to saturate in some areas, thereby creating flux barriers and reducing the magnitude of the subharmonic fluxes traversing the machine, potentially reducing the rotor losses.

The analytical estimation of induced eddy-current losses has been identified as the most challenging part of the analysis. Various methods for the computation of eddy-current magnet losses exist, and a few of them have been analysed here. In this thesis, it has been shown that it is possible to find the order of magnitude of the eddy-current losses, but when the level of segmentation is either high or low, the analytical results do not agree well with the FEA results. This finding is another contribution of this thesis.
When the level of segmentation is low, the analytically predicted loss is too high. The probable reason for this is that the analytical equations do not account for the influence of the eddy currents on the magnetic field. FEA shows that the flux density distribution in a machine is significantly affected by the field produced by the eddy currents in the magnets.
When the level of segmentation is high, the analytical equations underestimate the magnet eddy-current losses. The reasons might be that the stator leakage flux is not included in the analytical models and that only radial magnet fields are assumed. FEA has shown that when the magnet segments are thin, the induced eddy currents are predominantly caused by tangential fields.
For more precise results on eddy-current losses, more accurate models would be required. Analytical methods involving complex differential equations may be capable of producing better results. However, the most accurate results would be achieved by including FEA in the optimisation routine. With the aid of supercomputing and parallel processing, this may be a possibility for future work on the optimisation of electrical machines.

The objective value considered in the optimisation includes both the cost of the active materials (including the housing) and the cost of the energy lost over the lifetime of the generator. The cost of the active materials includes, to a certain degree, the labour required for the production of the machine. The number of windings, the number of magnet laminations and the skewing of the rotor all incur small costs for the machine. The cost of lost energy is a function of the lifetime energy loss, which can be found using information about the expected operation of the turbine. Tidal turbine operation can be easily predicted many years in advance; hence, one can calculate the produced energy and the energy loss with a high degree of fidelity. The cost of lost energy is discounted, as it will occur in the future.

There are two main classes of optimisation methods: gradient-based optimisation and direct optimisation. The benefits of gradient-based optimisation algorithms are their low time consumption and their ability to locate the feasible region of the problem. One disadvantage is that in a single run, a gradient-based algorithm can only locate the local minimum that is dictated by the starting point for that run. Another downside is that such algorithms cannot be used to solve problems with integer-valued variables and non-smooth objective functions.
The benefits of direct optimisation methods are that they can locate the global minimum and are not dependent on a starting point. Their main shortcoming is the time required to find a solution. In addition, their ability to locate the global minimum depends on the number of individuals considered in the analysis and the diversity of the population.

This thesis illustrates the different opportunities offered by these two different optimisation methods. To solve the design problem using a gradient-based algorithm, a reduced problem was constructed in which the values of the integer variables are fixed. The gradient-based optimisation function *fmincon* in MATLAB was used to locate the optimal generator designs.
First, the optimal design solution to the reduced problem for a generator with a one-stage gear train was found. The cost of the active materials, the energy cost and the total cost were found as functions of the number of base windings. It was shown that the cost of the active materials decreases with an increasing number of base windings, whereas the lost energy cost increases; the minimum corresponds to an n_{base} of 6. By studying the optimal machine designs for the different numbers of base windings, it has been shown that in low-pole-number machines, the optimal designs have higher temperatures and flux densities and lower short-circuit magnet flux densities, whereas high-pole-number machines have larger outer diameters, higher current densities and higher power factors.

An optimisation tool can be used for more than simply finding one optimal machine design. The strength of such a tool is that it can also be used to reveal trends and to determine the machine cost as a function of any parameter. The generator cost as a function of the power factor has been presented. It was found that a machine with a power factor of 0.92 is 11 300 EUR more expensive than a machine with a power factor of 0.85. It was also possible to investigate how the optimal design would change as a function of the energy or PM price, for example.
Two designs were compared in which one was optimised for the total cost and the other was optimised for the mechanical cost alone. The two designs were dramatically different. The mechanical cost of the latter was 15% lower than that of the former; however, the total cost was 28% higher.

The gradient-based method was also used to find the optimal designs for a direct-drive generator and for a generator with a two-stage gear train. The highest-speed generator was the lightest and least expensive generator, and it had the highest efficiency. This was achieved at the expense of a gear system with a large gear ratio, higher gear losses and a reduced gear reliability.

The main goal of this PhD project was to determine whether concentrated windings or distributed windings are preferable for a tidal turbine generator. The initial expectation was that for low-speed generators, concentrated windings would be optimal, whereas for high-speed generators, distributed windings would be optimal. A direct optimisation method is necessary to answer this question, as the numbers of poles and slots must be free to vary.
The main contribution of this thesis is the development of an optimisation tool that can compare machine designs with different numbers of slots and poles. The algorithm does not differentiate between FSCW and DW layouts.
A hybrid optimisation algorithm has been developed that combines the benefits of a gradient-based algorithm and a direct optimisation algorithm. The hybrid optimisation revealed that double-layer FSCW machines provide the lowest turbine generator cost when the speed is less than approximately 1000 rpm. In a generator equipped with a three-stage gear train, either FSCWs or DWs can be used at comparable costs.
The price of the generator decreases as the gear ratio increases, as expected. The reduction is most significant at the transition from a direct drive to a one-stage gear train. The curve showing the cost as a function of the generator speed can help to guide the system owner in selecting the drive-train topology. Based on gear efficiency estimates, it has been found that the highest total efficiency can be achieved with a two-stage gear train.

7.1 Challenges and future work

At the end of a long PhD project, one is always left with a series of questions and tasks one would have liked to finish but that time did not allow.

As mentioned in the introduction, the quality of the analysis is very important to the performance of the optimisation routine. There are some weaknesses in my analysis. A better formulation of the Carter coefficient would likely have improved the magnetic analysis. At the very end of my project, I realised that the Carter coefficient expression that I chose, given by Nasar in [66], is quite accurate for the two distributed winding machines, but the Carter coefficient given by Ward and Lawrenson in [127] provides a more accurate calculation for the two concentrated winding machines. Yet another expression, given by F.W. Carter himself [88], is widely used in the literature [53]. A comparison of different Carter coefficient ex-

pressions for various machine configurations would have been helpful here. If it is true that one is typically better for FSCW machines and another for DW machines, then the greatest difficulty lies in knowing when to use one or the other, because the transition from FSCW to DW designs is really quite smooth.
The calculations of the inductance and the slot leakage in double-layer FSCW machines could also have been improved. Again, I discovered this late in the project. Compared with the FEA results, it is clear that the analytical expressions are not very accurate.

The topic that I have spent the most time investigating is the estimation of the induced eddy-current losses in the magnets. Initially, I wanted to include the losses in the solid stator yoke as well, but after months of work, I realised that this was too ambitious and should more appropriately be the topic of another PhD thesis in itself. I admit that I am disappointed that neither of the methods that I investigated for calculating the PM losses yielded very good results compared with 2D FEA simulations. I do hope that in the not so distant future, a more accurate analytical approach can be adopted by the machine design community. In the meantime, I will continue to use FEA for PM loss calculations.

There are, of course, several aspects that I had planned to include in my work but have been obliged to abandon. One of these is the cost and efficiency of the power converter. Had these been included in the objective function, I could have found the optimal load angle by treating it as one of the variables. I would also have liked to calculate the cogging torques of the machines and place a constraint on the maximum allowed cogging torque. However, I did not prioritise this task, as the detailed design of the magnets and teeth strongly affects the cogging torque and these design details were outside the scope of this work.
Optimally, the mechanical structure of the generator would also be included in the model. This might change the optimal designs.

When planning this PhD research, I wanted to include FEA in the optimisation procedure. However, I realised that if I were to do so, I would not be able to focus as much on the optimisation theory, and I would certainly have been obliged to limit the search space considered in the optimisation.
I do hope that some future PhD student will be able to use what I have learnt and apply it in an FEA-based optimisation with the same wide search space and as many variables as were considered here. One of the obstacles hindering such a study is the availability of software that enables parallel processing on many cores without an enormous increase in cost from the purchase of many licenses. I am confident that with the further development of supercomputers and parallel computing, this issue will be solved in the near future.

Appendix A

Armature-induced eddy-current loss in magnets: Method 4

The methodology described here is presented in [84] and [87] and is used to calculate the MMF-induced eddy-current losses in PMs. The cited references provide extensions of the model presented in [83] by Atallah et al.
It is assumed that induced losses arise only in the magnets and that the current is resistance-limited, i.e., the skin depth is greater than the PM dimensions. The stator current distribution is represented by an equivalent sheet current over the slot openings, and the separation of variables method is used to solve Laplace's equation in the air gap and magnet regions. The effect of the eddy currents on the applied magnetic field is neglected. An infinite length is assumed, which means that end effects are also neglected.

Under the assumption of balanced three-phase windings, the Fourier series expression for the sheet current, as a function of time (t) and position (θ), is

$$J_s(\theta,t) = \begin{cases} \sum\limits_n J_n cos\left[(p_r - np_s)\omega t - np_s\theta\right] & \text{for} \quad n = qk + m \\ -\sum\limits_n J_n cos\left[(p_r + np_s)\omega t + np_s\theta\right] & \text{for} \quad n = qk - m \\ 0 & \text{for} \quad n \neq qk \pm m \end{cases} \tag{A.1}$$

p_r and p_s are the numbers of fundamental rotor and stator poles, respectively. p_s is the lowest harmonic produced by the stator current, namely, n_{base}. $n = 1$ represents the lowest harmonic produced by the stator windings. q is the number of phases, k is an arbitrary integer value, and m is either -1 or 1, depending on the winding layout. If the lowest harmonic, with p_s pole pairs, rotates in the same

direction as the main harmonic, with p_r pole pairs, then $m = 1$. If the rotation is opposite, then $m = -1$. Equation 45 in [63] is used to find the rotational directions.

$$J_n = \frac{3\widehat{I}_s n_{cs}}{\pi R_s N_{lay}} k_{wn} K_{son} \tag{A.2}$$

$\widehat{I}_s$ is the amplitude of the total slot current, R_s is the stator bore radius, k_{wn} is the harmonic winding factor, and K_{son} is the slot opening factor [87]:

$$K_{son} = \frac{sin\left(nw_{slot}/2R_s\right)}{nw_s lot/2R_s} \tag{A.3}$$

When each magnet pole is segmented into N_{stk} pieces of width α_p, the total eddy-current loss per unit axial length is given by

$$P_{pm,4} = 2pN_{stk} \sum_n P_{cn} + P_{an} \tag{A.4}$$

$$\begin{aligned} P_{cn} = {} & \frac{\mu_0^2 \alpha_p}{\rho} p_r \sum_n^{\infty} \frac{J_n^2 (p_r \pm np_s)^2 \omega^2}{\left(1 - (R_r/R_s)^{2np_s}\right)^2 (np_s)^2} \\ & \times \left\{ \left(\frac{R_m}{R_s}\right)^{2np_s} \frac{R_s^2 R_m^2}{2np_s + 2} \left[1 - \left(\frac{R_r}{R_m}\right)^{2np_s+2}\right] \right. \\ & \left. + \left(\frac{R_r}{R_s}\right)^{2np_s} R_s^2 (R_m^2 - R_r^2) + \left(\frac{R_r}{R_s}\right)^{2np_s} R_s^2 R_r^2 F_v \right\} \end{aligned} \tag{A.5}$$

$$F_n = \begin{cases} \frac{\left(\frac{R_m}{R_r}\right)^{-2np_s+2} - 1}{-2np_s+2} & \text{for} \quad np_s \neq 1 \\ \ln\left(\frac{R_m}{R_r}\right) & \text{for} \quad np_s = 1 \end{cases} \tag{A.6}$$

$$\begin{aligned} P_{an} = {} & \left[-\frac{8\mu_0^2}{\alpha_p \rho} p_r \sum_n^{\infty} \frac{J_n^2 (p_r \pm np_s)^2 \omega^2}{\left(1 - (R_r/R_s)^{2np_s}\right)^2 (np_s)^4} \right. \\ & \left. \times \frac{H_n^2}{(R_m^2 - R_r^2)} \cdot sin^2(np_s \frac{\alpha_p}{2}) \right] \end{aligned} \tag{A.7}$$

$$H_n = \left(\frac{R_m}{R_s}\right)^{np_s} \frac{R_s R_m^2}{np_s + 2} \left[1 - \left(\frac{R_r}{R_m}\right)^{np_s+2}\right] + \left(\frac{R_r}{R_s}\right)^{np_s} R_s R_r^2 E_n \tag{A.8}$$

$$E_n = \begin{cases} \frac{\left(\frac{R_m}{R_r}\right)^{-np_s+2} - 1}{-np_s+2} & \text{for} \quad np_s \neq 2 \\ \ln\left(\frac{R_m}{R_r}\right) & \text{for} \quad np_s = 2 \end{cases} \tag{A.9}$$

ρ is the resistivity of the PM material. When $n = qk + m$, the $\pm$ in P_{cn} and P_{an} is taken to be $-$; when $n = qk - m$, it is taken to be $+$.
R_m is the outer radius of the rotor. $R_s = R_m + gk_c$ is the modified stator bore radius, and $R_r = R_m - l_m$ is the outer radius of the rotor yoke.

Bibliography

[1] R. Brooks, 'The world offshore energy renewable report 2004-2008', DTI's 2010 Target Team, UK, Tech. Rep., 2004.

[2] Carbon Trust, 'Accelerating marine energy: The potential for cost reduction - insights from the carbon trust marine energy accelerator', Carbon Trust, London, UK, Tech. Rep., 2011.

[3] P Asmus and D Gauntlett, 'Hydrokinetic and ocean energy: Renewable power generation from ocean wave, tidal stream, river hydrokinetic, ocean current, and ocean thermal technologyh', Pike Research, Market Research Report, 2012.

[4] *Emec. tidal developers*, Visited in January 2016. [Online]. Available: `http://www.emec.org.uk/marine-energy/tidal-developers` (visited on 26/01/2016).

[5] J King and T Tryfonas, 'Tidal stream power technology-state of the art', in *OCEANS 2009-EUROPE*, IEEE, 2009, pp. 1–8.

[6] TNEI, 'Marine energy electrical architecture, report 1: Landscape map and literature review', TNEI, ORE Catapult, Tech. Rep., Sep. 2015, PN000083-LRT-006.

[7] D. Magagna and A. Uihlein, '2014 jrc ocean energy status report', 2015, Report EUR 26983 EN.

[8] S. Bower, 'Drivetrain options for tidal stream', in *All Enegy Conference 2013*, 2013.

[9] L. I. Lago, F. L. Ponta and L. Chen, 'Advances and trends in hydrokinetic turbine systems', *Energy for Sustainable Development*, vol. 14, no. 4, pp. 287–296, 2010.

[10] M. Mueller and R. Wallace, 'Enabling science and technology for marine renewable energy', *Energy Policy*, vol. 36, no. 12, pp. 4376–4382, 2008.

[11] R. Bedard, 'Survey and characterization tidal in stream energy conversion (tisec) devices', EPRI, Tech. Rep., 2005.

[12] A. S. Bahaj, 'Generating electricity from the oceans', *Renewable and Sustainable Energy Reviews*, vol. 15, no. 7, pp. 3399–3416, 2011.

[13] M. S. Güney and K. Kaygusuz, 'Hydrokinetic energy conversion systems: A technology status review', *Renewable and Sustainable Energy Reviews*, vol. 14, no. 9, pp. 2996–3004, 2010.

[14] M. J. Khan, G. Bhuyan, M. T. Iqbal and J. E. Quaicoe, 'Hydrokinetic energy conversion systems and assessment of horizontal and vertical axis turbines for river and tidal applications: A technology status review', *Applied Energy*, vol. 86, no. 10, pp. 1823–1835, 2009.

[15] F. O. Rourke, F. Boyle and A. Reynolds, 'Marine current energy devices: Current status and possible future applications in ireland', *Renewable and Sustainable Energy Reviews*, vol. 14, no. 3, pp. 1026–1036, 2010.

[16] J. Hardisty, *The Ananlysis of Tidal Stream Power*. John Wiley & Sons Ltd., 2009.

[17] Z. Zhou, F. Scuiller, J. F. Charpentier, M. Benbouzid and T. Tang, 'An up-to-date review of large marine tidal current turbine technologies', in *Electronics and Application Conference and Exposition (PEAC), 2014 International*, IEEE, 2014, pp. 480–484.

[18] Strategic initiative for ocean energy, 'Ocean energy: State of the art', *Online report, December*, 2012.

[19] T. Corsatea and D. Magagna, *Overview of European innovation activities in marine energy technology*. Publications Office of the European Union, 2013.

[20] *Orpc*, visited in January 2016. [Online]. Available: `http://www.orpc.co/`.

[21] *Natural resources canada*, Visited in January 2016. [Online]. Available: `http://www.nrcan.gc.ca/science/story/11718`.

[22] *Pulse tidal*, Visited October 2012. [Online]. Available: `http://www.pulsetidal.com/`.

[23] *Open hydro*, Visited in January 2016. [Online]. Available: `http://www.openhydro.com`.

[24] *Atlantis resorces corporation*, Visited in January 2016. [Online]. Available: http://www.atlantisresourcescorporation.com/.

[25] *Andritz. tidal current turbines*, Visited in January 2016. [Online]. Available: https://www.andritz.com/index/hydro/hy-others-andritz-hydro/hy-tidal-current-turbine.htm.

[26] *Tidal generation ltd*, Visited Ocober 2012. [Online]. Available: http://www.tidalgeneration.co.uk/.

[27] *Powertechnology.com. alstom's oceade tidal turbine certified by dnv gl*, Visited January 2016. [Online]. Available: http://www.power-technology.com/news/newsalstoms-oceade-tidal-turbine-certified-by-dnv-gl-4649565.

[28] *Voith*, Visited October 2012. [Online]. Available: http://voith.com/.

[29] *Marine current turbines*, Visited January 2016. [Online]. Available: http://www.marineturbines.com/.

[30] C. A. Douglas, G. P. Harrison and J. P. Chick, 'Life cycle assessment of the seagen marine current turbine', *Proceedings of the Institution of Mechanical Engineers Part M: Journal of Engineering for the Maritime Environment*, vol. 222, no. 1, pp. 1–12, 2008.

[31] *Tidal energy ltd.* Visited January 2016. [Online]. Available: http://www.tidalenergyltd.com/.

[32] *Oceanflow*, Visited January 2016. [Online]. Available: http://www.oceanflowenergy.com/.

[33] *Scotrenewables*, Visited January 2016. [Online]. Available: http://www.scotrenewables.com/.

[34] A. Signahl and N. Hjerpe, 'Deep green i oceana strömmar-en konceptstudie', *Linköpings universitet*, 2010.

[35] *Minesto*, Visited January 2016. [Online]. Available: http://minesto.com/deep-green/.

[36] *Flumill as*, Visited January 2016. [Online]. Available: www.flumill.com.

[37] O Keysan, A McDonald and M Mueller, 'Integrated design and optimization of a direct drive axial flux permanent magnet generator for a tidal turbine', *Proceedings of the International Conference on Renewable Energies and Power Quality-ICREPQ, Granada, Spain*, pp. 23–25, 2010.

[38] *Control of permanent magnet synchronous motors for automotive applications*, Visited March 2016. [Online]. Available: http://wwwlea.uni-paderborn.de/en/research/pmsm-control.html.

[39] W. Chu, Z. Zhu and J. Chen, 'Analytical optimization and comparison of torque densities between permanent magnet and electrically excited machines', cited By (since 1996)0, 2012, pp. 1192–1198. [Online]. Available: http://www.scopus.com/inward/record.url?eid=2-s2.0-84870791531&partnerID=40&md5=ea214bc992bc81d542225f15248ac6a2.

[40] J. A. Stegmann and M. J. Kamper, 'Design aspects of double-sided rotor radial flux air-cored permanent-magnet wind generator', *IEEE Transactions on Industry Applications*, vol. 47, no. 2, pp. 767–778, 2011.

[41] A. Røkke, 'Gradient based optimization of permanent magnet generator design for a tidal turbine', in *Electrical Machines (ICEM), 2014 International Conference on*, Sep. 2014, pp. 1199–1205. DOI: 10.1109/ICELMACH.2014.6960334.

[42] *Emetor. number of winding layers*, Visited February 2016. [Online]. Available: http://www.emetor.org/glossary/number-of-layers/.

[43] O. Chiver, L. Petrean, L. Neamt and Z. Erdei, 'Study regarding end winding inductance of three phase ac windings in a single layer', in *Proceedings of the International Conference on ENERGY and ENVIRONMENT TECHNOLOGIES and EQUIPMENT*, 2010, pp. 20–22.

[44] *Abb*, Visited February 2016. [Online]. Available: http://new.abb.com/motors-generators/generators/generators-for-steam-and-gas-turbines/compact-high-voltage-turbine-generators.

[45] A. M. El-Refaie, 'Fractional-slot concentrated-windings synchronous permanent magnet machines: Opportunities and challenges', *Industrial electronics, IEEE Transactions on*, vol. 57, no. 1, pp. 107–121, 2010.

[46] P. M. Lindh, H. K. Jussila, M. Niemelä, A. Parviainen and J. Pyrhönen, 'Comparison of concentrated winding permanent magnet motors with embedded and surface-mounted rotor magnets', *Magnetics, IEEE Transactions on*, vol. 45, no. 5, pp. 2085–2089, 2009.

[47] A. M. El-Refaie and M. R. Shah, 'Comparison of induction machine performance with distributed and fractional-slot concentrated windings', in *Industry Applications Society Annual Meeting, 2008. IAS'08. IEEE*, IEEE, 2008, pp. 1–8.

[48] A. M. El-Refaie and T. M. Jahns, 'Comparison of synchronous pm machine types for wide constant-power speed range operation', in *Industry Applications Conference, 2005. Fourtieth IAS Annual Meeting. Conference Record of the 2005*, IEEE, vol. 2, 2005, pp. 1015–1022.

[49] J. K. Tangudu and T. M. Jahns, 'Comparison of interior pm machines with concentrated and distributed stator windings for traction applications', in *Vehicle Power and Propulsion Conference (VPPC), 2011 IEEE*, IEEE, 2011, pp. 1–8.

[50] S.-O. Kwon, S.-I. Kim, P. Zhang and J.-P. Hong, 'Performance comparison of ipmsm with distributed and concentrated windings', in *Industry Applications Conference, 2006. 41st IAS Annual Meeting. Conference Record of the 2006 IEEE*, IEEE, vol. 4, 2006, pp. 1984–1988.

[51] A. R. Muñoz, F. Liang and M. W. Degner, 'Evaluation of interior pm and surface pm synchronous machines with distributed and concentrated windings', in *Industrial Electronics, 2008. IECON 2008. 34th Annual Conference of IEEE*, IEEE, 2008, pp. 1189–1193.

[52] X. Chen, J. Wang, P. Lazari and L. Chen, 'Permanent magnet assisted synchronous reluctance machine with fractional-slot winding configurations', in *Electric Machines & Drives Conference (IEMDC), 2013 IEEE International*, IEEE, 2013, pp. 374–381.

[53] J. Pyrhonen, T. Jokinen and V. Hrabovcová, *Design of rotating electrical machines*. Wiley, 2009.

[54] M. Liwschitz-Garik, *Winding Alternating-Current Machines*. D. Van Nostrand Company, INc., New York, 1950.

[55] S. Skaar and R Nilssen, 'Distribution, coil-span and winding factors for pm machines with concentrated windings', *ICEM 2006*, pp. 2 –5, 2006.

[56] A. Røkke and R. Nilssen, 'Analytical calculation of yoke flux patterns in fractional-slot permanent magnet machines', *IEEE Transactions on Magnetics*, vol. 53, no. 4, pp. 1–9, 2017.

[57] Z. Zhu and D. Howe, 'Instantaneous magnetic field distribution in brushless permanent magnet dc motors. ii. armature-reaction field', *Magnetics, IEEE Transactions on*, vol. 29, no. 1, pp. 136–142, 1993.

[58] Z. Zhu, K. B. Ng and D. Howe, 'Analytical prediction of stator flux density waveforms and iron losses in brushless dc machines, accounting for load condition', in *Electrical Machines and Systems, 2001. ICEMS 2001. Proceedings of the Fifth International Conference on*, IEEE, vol. 2, 2001, pp. 814–817.

[59] F. Meier and J. Soulard, 'Analysis of flux measurements on a pmsm with non-overlapping concentrated windings', in *Industry Applications Society Annual Meeting, 2008. IAS '08. IEEE*, Oct. 2008, pp. 1–8. DOI: 10.1109/08IAS.2008.62.

[60] N. Bianchi, S. Bolognani and M. D. Pre, 'Magnetic loading of fractional-slot three-phase pm motors with nonoverlapped coils', *Industry Applications, IEEE Transactions on*, vol. 44, no. 5, pp. 1513–1521, 2008.

[61] G. Y. Sizov, D. M. Ionel and N. A. Demerdash, 'Modeling and design optimization of pm ac machines using computationally efficient-finite element analysis', in *Energy Conversion Congress and Exposition (ECCE), 2010 IEEE*, IEEE, 2010, pp. 578–585.

[62] D. Ionel and M. Popescu, 'Ultrafast finite-element analysis of brushless pm machines based on space-time transformations', *Industry Applications, IEEE Transactions on*, vol. 47, no. 2, pp. 744–753, Mar. 2011. DOI: 10.1109/TIA.2010.2102733.

[63] Ø. Krøvel, 'Design of large permanent magnetized synchronous electric machines', PhD thesis, Norwegian University of Science and Technology (NTNU), Norway, 2011.

[64] S. Meier, 'Theoretical design of surface-mounted permanent magnet motors with field-weakening capability', Master's thesis, M. Sc. thesis, KTH, 2002.

[65] D. C. Hanselman, *Brushless permanent-magnet motor design*. McGraw-Hill New York, 1994.

[66] S. A. Nasar, *Handbook of electric machines*. McGraw-Hill Companies, 1987.

[67] H. A. Toliyat and G. B. Kliman, *Handbook of electric motors*. CRC press, 2004, vol. 120.

[68] P. Salminen, 'Fractional slot permanent magnet synchronous motors for low speed applications', *Acta Universitatis Lappeenrantaensis*, 2004.

[69] D. Ionel and M. Popescu, 'Ultrafast finite-element analysis of brushless pm machines based on space-time transformations', *IEEE Transactions on Industry Applications*, vol. 47, no. 2, pp. 744–753, Mar. 2011. DOI: 10.1109/TIA.2010.2102733.

[70] G. Dajaku, W. Xie and D. Gerling, 'Reduction of low space harmonics for the fractional slot concentrated windings using a novel stator design', *Magnetics, IEEE Transactions on*, vol. 50, no. 5, pp. 1–12, 2014.

[71] G. Dajaku and D. Gerling, 'Analysis of different pm machines with concentrated windings and flux barriers in stator core', in *Electrical Machines (ICEM), 2014 International Conference on*, IEEE, 2014, pp. 375–384.

[72] P. Ponomarev, P. Lindh and J. Pyrhonen, 'Effect of slot-and-pole combination on the leakage inductance and the performance of tooth-coil permanent-magnet synchronous machines', *Industrial Electronics, IEEE Transactions on*, vol. 60, no. 10, pp. 4310–4317, 2013.

[73] A. M. El-Refaie and T. M. Jahns, 'Optimal flux weakening in surface pm machines using fractional-slot concentrated windings', *Industry Applications, IEEE Transactions on*, vol. 41, no. 3, pp. 790–800, 2005.

[74] T. A. Lipo, *Vector control and dynamics of AC drives*. Oxford university press, 1996, vol. 41.

[75] C. Mi, G. Slemon and R. Bonert, 'Modeling of iron losses of surface-mounted permanent magnet synchronous motors', in *Industry Applications Conference, 2001. Thirty-Sixth IAS Annual Meeting. Conference Record of the 2001 IEEE*, vol. 4, Sep. 2001, 2585–2591 vol.4. DOI: 10.1109/IAS.2001.955984.

[76] F. Sahin, 'Design and development of a high-speed axial-flux permanent-magnet machine', PhD thesis, TU Eindhoven, 2001.

[77] M. Markovic and Y. Perriard, 'A simplified determination of the permanent magnet (pm) eddy current losses due to slotting in a pm rotating motor', in *Electrical Machines and Systems, 2008. ICEMS 2008. International Conference on*, IEEE, 2008, pp. 309–313.

[78] L. Wu, Z. Zhu, D Staton, M Popescu and D Hawkins, 'Analytical model for predicting magnet loss of surface-mounted permanent magnet machines accounting for slotting effect and load', *Magnetics, IEEE Transactions on*, vol. 48, no. 1, pp. 107–117, 2012.

[79] J. Pyrhönen, H. Jussila, Y. Alexandrova, P. Rafajdus and J. Nerg, 'Harmonic loss calculation in rotor surface permanent magnetsůnew analytic approach', *Magnetics, IEEE Transactions on*, vol. 48, no. 8, pp. 2358–2366, 2012.

[80] L. Wu, Z. Zhu, D Staton, M Popescu and D Hawkins, 'Analytical modeling and analysis of open-circuit magnet loss in surface-mounted permanent-magnet machines', *Magnetics, IEEE Transactions on*, vol. 48, no. 3, pp. 1234–1247, 2012.

[81] E. Fornasiero, 'Advanced design of direct drive pm machines', PhD thesis, University of Padova, 2010.

[82] H Polinder and M. Hoeijmakers, 'Eddy-current losses in the segmented surface-mounted magnets of a pm machine', in *Electric Power Applications, IEE Proceedings-*, IET, vol. 146, 1999, pp. 261–266.

[83] K. Atallah, D. Howe, P. H. Mellor, D. Stone *et al.*, 'Rotor loss in permanent-magnet brushless ac machines', *Industry Applications, IEEE Transactions on*, vol. 36, no. 6, pp. 1612–1618, 2000.

[84] D. Ishak, Z. Zhu and D. Howe, 'Eddy-current loss in the rotor magnets of permanent-magnet brushless machines having a fractional number of slots per pole', *Magnetics, IEEE Transactions on*, vol. 41, no. 9, pp. 2462–2469, 2005.

[85] Z. Zhu, K Ng, N Schofield and D Howe, 'Improved analytical modelling of rotor eddy current loss in brushless machines equipped with surface-mounted permanent magnets', in *Electric Power Applications, IEE Proceedings-*, IET, vol. 151, 2004, pp. 641–650.

[86] J Alexandrova, H Jussila, J Nerg and J Pyrhö, 'Comparison between models for eddy-current loss calculations in rotor surface-mounted permanent magnets', in *Electrical Machines (ICEM), 2010 XIX International Conference on*, IEEE, 2010, pp. 1–6.

[87] Z. Fang, Z. Zhu, L. Wu and Z. Xia, 'Simple and accurate analytical estimation of slotting effect on magnet loss in fractional-slot surface-mounted pm machines', in *Electrical Machines (ICEM), 2012 XXth International Conference on*, IEEE, 2012, pp. 464–470.

[88] F. Carter, 'Air-gap induction', *Electrical world and engineering*, vol. 38, no. 22, pp. 884–888, 1901.

[89] E. Fornasiero, L. Alberti, N. Bianchi and S. Bolognani, 'Considerations on selecting fractionalůslot windings', in *Energy Conversion Congress and Exposition (ECCE), 2010 IEEE*, IEEE, 2010, pp. 1376–1383.

[90] Z. Zhu, K. B. Ng, N. Schofield and D. Howe, 'Analytical prediction of rotor eddy current loss in brushless machines equipped with surface-mounted permanent magnets. i. magnetostatic field model', in *Electrical Machines and Systems, 2001. ICEMS 2001. Proceedings of the Fifth International Conference on*, IEEE, vol. 2, 2001, pp. 806–809.

[91] ——, 'Analytical prediction of rotor eddy current loss in brushless machines equipped with surface-mounted permanent magnets. ii. accounting for eddy current reaction field', in *Electrical Machines and Systems, 2001. ICEMS 2001. Proceedings of the Fifth International Conference on*, IEEE, vol. 2, 2001, pp. 810–813.

[92] K. M. Becker and J. Kaye, 'Measurements of diabatic flow in an annulus with an inner rotating cylinder', *Journal of Heat Transfer*, vol. 84, no. 2, pp. 97–104, 1962.

[93] D. Howey, P. Childs and A. Holmes, 'Air-gap convection in rotating electrical machines', *Industrial Electronics, IEEE Transactions on*, vol. 59, no. 3, pp. 1367–1375, Mar. 2012. DOI: 10.1109/TIE.2010.2100337.

[94] G. Henneberger, K. Yahia and M. Schmitz, 'Calculation and identification of a thermal equivalent circuit of a water cooled induction motor for electric vehicle applications', in *7th Int. Conf El. Mach. Drives (Conf. Publ. No. 412)*, Sep. 1995, pp. 6–10. DOI: 10.1049/cp:19950825.

[95] Neorem, Dec. 2015. [Online]. Available: http://www.neorem.fi/files/neorem/product-PDF/500t/neorem-magneettikayra-malli-a5-576t.pdf.

[96] J. Aubry, H. Ahmed and B. Multon, 'Sizing optimization methodology of a surface permanent magnet machine-converter system over a torque-speed operating profile: Application to a wave energy converter', *Industrial Electronics, IEEE Transactions on*, vol. 59, no. 5, pp. 2116–2125, May 2012. DOI: 10.1109/TIE.2011.2163287.

[97] J. Aubry, H. Ben Ahmed and B. Multon, 'Bi-objective sizing optimization of a pm machine drive on an operating profile', in *Electrical Machines (ICEM), 2010 XIX International Conference on*, Sep. 2010, pp. 1–7. DOI: 10.1109/ICELMACH.2010.5608308.

[98] N. Hodgins, O. Keysan, A. McDonald and M. Mueller, 'Design and testing of a linear generator for wave-energy applications', *Industrial Electronics, IEEE Transactions on*, vol. 59, no. 5, pp. 2094–2103, May 2012. DOI: 10.1109/TIE.2011.2141103.

[99] G. R. Slemon and X. Liu, 'Modeling and design optimization of permanent magnet motors', *Electric Machines & Power Systems*, vol. 20, no. 2, pp. 71–92, 1992. DOI: 10.1080/07313569208909572. eprint: http://dx.doi.org/10.1080/07313569208909572.

[100] T. Hamiti, C. Gerada and M. Rottach, 'Weight optimisation of a surface mount permanent magnet synchronous motor using genetic algorithms and a combined electromagnetic-thermal co-simulation environment', in *Energy Conversion Congress and Exposition (ECCE), 2011 IEEE*, 2011, pp. 1536–1540.

[101] J. Legranger, G. Friedrich, S. Vivier and J. Mipo, 'Combination of finite-element and analytical models in the optimal multidomain design of machines: Application to an interior permanent-magnet starter generator', *IEEE Transactions on Industry Applications*, vol. 46, no. 1, pp. 232–239, 2010.

[102] H. Li, Z. Chen and H. Polinder, 'Optimization of multibrid permanent-magnet wind generator systems', *IEEE Transactions on Energy Conversion*, vol. 24, no. 1, pp. 82–92, 2009.

[103] R. Wrobel and P. H. Mellor, 'Design considerations of a direct drive brushless machine with concentrated windings', *Energy Conversion, IEEE Transactions on*, vol. 23, no. 1, pp. 1–8, 2008.

[104] S. Cafieri, L. Liberti, B. Nogarede *et al.*, 'Optimal design of electrical machines: Mathematical programming formulations', *COMPEL: The International Journal for Computation and Mathematics in Electrical and Electronic Engineering*, vol. 32, no. 3, pp. 977–996, 2013.

[105] T. Raminosoa, I. Rasoanarivo, F.-M. Sargos and R. Andriamalala, 'Constrained optimization of high power synchronous reluctance motor using non linear reluctance network modeling', in *41st IAS Annual Meeting (IEEE Industry ApplicationsSociety)*, 2006, pp. 1201–1208.

[106] S.-B. Yoon, I.-S. Jung, D.-S. Hyun, J.-P. Hong and Y.-J. Kim, 'Robust shape optimization of electromechanical devices', *Magnetics, IEEE Transactions on*, vol. 35, no. 3, pp. 1710–1713, 1999. DOI: 10.1109/20.767356.

[107] R. Carlson and F. Wurtz, 'The concepts of sizing and optimization model: Applied to the optimal design of a permanent magnet generator', in *Electrical Machines and Power Electronics and 2011 Electromotion Joint Conference (ACEMP), 2011 International Aegean Conference on*, IEEE, 2013, pp. 651–656.

[108] MathWorks, *Constrained nonlinear optimization algorithms*, Visited June 2013, MathWorks. [Online]. Available: http://www.mathworks.se/help/optim/ug/constrained-nonlinear-optimization-algorithms.html.

[109] F. Brunet, *Basics on continuous optimization*, Visited February 2016. [Online]. Available: http://www.brnt.eu/phd/node10.html.

[110] Y. Duan and D. M. Ionel, 'A review of recent developments in electrical machine design optimization methods with a permanent magnet synchronous motor benchmark study', in *Energy Conversion Congress and Exposition (ECCE)*, IEEE, 2011, pp. 3694–3701.

[111] F. Cupertino, G. Pellegrino, E. Armando and C. Gerada, 'A syr and ipm machine design methodology assisted by optimization algorithms', in *2012 IEEE Energy Conversion Congress and Exposition (ECCE)*, 2012, pp. 3686–3691.

[112] T. D. Strous, X. Wang, H. Polinder and J. Ferreira, 'Finite element based multi-objective optimization of a brushless doubly-fed induction machine', Electric Machines & Drives Conference (IEMDC), 2015.

[113] J.-S. Chun, H.-K. Jung and S.-Y. Hahn, 'A study on comparison of optimization performances between immune algorithm and other heuristic algorithms', *IEEE Transactions on Magnetics*, vol. 34, no. 5, pp. 2968–2971, 1998.

[114] M. Farina and J. Sykulski, 'Comparative study of evolution strategies combined with approximation techniques for practical electromagnetic optimization problems', *IEEE Transactions on Magnetics*, vol. 37, no. 5, pp. 3216–3220, 2001.

[115] M Van der Geest, H Polinder, J. Ferreira and D Zeilstra, 'Optimization and comparison of electrical machines using particle swarm optimization', in *Electrical Machines (ICEM), 2012 XXth International Conference on*, IEEE, 2012, pp. 1380–1386.

[116] E. L. Engevik, A. Røkke and R. Nilssen, 'Evaluating hybrid optimization algorithms for design of a permanent magnet generator', Electromotion Joint International Conference (ACEMP-OPTIM) 2015 , Side-Turkey, Sep. 2015, pp. 711–718.

[117] J. Vasconcelos, R. Saldanha, L. Krähenbühl and A. Nicolas, 'Genetic algorithm coupled with a deterministic method for optimization in electromagnetics', *IEEE Transactions on Magnetics*, vol. 33, pp. 1860–1863, 1997.

[118] Y. Ahn, J. Park, C.-G. Lee, J.-W. Kim and S.-Y. Jung, 'Novel memetic algorithm implemented with ga (genetic algorithm) and mads (mesh adaptive direct search) for optimal design of electromagnetic system', *IEEE Transactions on Magnetics*, vol. 46, no. 6, pp. 1982–1985, 2010.

[119] O. Mohammed and G. Üler, 'A hybrid technique for the optimal design of electromagnetic devices using direct search and genetic algorithms', *IEEE Transactions on Magnetics*, vol. 33, no. 2, pp. 1931–1934, 1997.

[120] T. Nordaunet, 'Reducing sub-harmonic spatial fields in concentrated winding machines using genetic algorithms', Master's thesis, Norwegian University of Science and Technology (NTNU), 2013.

[121] MathWorks, *Population diversity*, Visited February 2016. [Online]. Available: `http://se.mathworks.com/help/gads/population-diversity.html`.

[122] Mathworks, *Genetic algorithm options*, Visited February 2016. [Online]. Available: http://se.mathworks.com/help/gads/genetic-algorithm-options.html#f9147.

[123] M. Cistelecan, M. Popescu and M. Popescu, 'Study of the number of slots/pole combinations for low speed permanent magnet synchronous generators', in *Proc. of IEEE Int. Electric Machines and Drives Conf.,(IEMDC)*, vol. 2, 2007, pp. 1616–1620.

[124] Y. G. Xu, G. Li and Z. Wu, 'A novel hybrid genetic algorithm using local optimizer based on heuristic pattern move', *Applied Artificial Intelligence*, vol. 15, no. 7, pp. 601–631, 2001. DOI: 10.1080/088395101750363966. eprint: http://dx.doi.org/10.1080/088395101750363966. [Online]. Available: http://dx.doi.org/10.1080/088395101750363966.

[125] P. Puri and S. Ghosh, 'A hybrid optimization approach for {pi} controller tuning based on gain and phase margin specifications', *Swarm and Evolutionary Computation*, vol. 8, pp. 69 –78, 2013. DOI: http://dx.doi.org/10.1016/j.swevo.2012.09.001. [Online]. Available: http://www.sciencedirect.com/science/article/pii/S2210650212000636.

[126] A. Matveev and A. Røkke, 'Power take-off for tidal turbines providing lowest cost of energy matveev', *Proceedings of the 10th European Wave and Tidal Energy Conference*, Sep. 2013.

[127] P. Ward and P. Lawrenson, 'Magnetic permeance of doubly-salient air-gaps', in *Proceedings of the Institution of Electrical Engineers*, IET, vol. 124, 1977, pp. 542–544.